이학박사 학위논문

Excitation Spectra of Triangular Antiferromagnet Hexagonal $RMnO_3$: Spontaneous Decays of Magneto-Elastic Excitation

삼각격자 반강자성체 육방정계 $RMnO_3$의 들뜸스펙트럼 연구: 자기-탄성 들뜸의 자발적 붕괴

2017년 8월

서울대학교 대학원

물리천문학부 물리학전공

오 주 성

Excitation Spectra of Triangular Antiferromagnet Hexagonal $RMnO_3$: Spontaneous Decays of Magneto-Elastic Excitation

지도 교수 박 제 근

이 논문을 이학박사 학위논문으로 제출함

2017년 8월

서울대학교 대학원

물리천문학부 물리학전공

오 주 성

오주성의 이학박사 학위논문을 인준함

2017년 6월

위 원 장 _____ (인)

부위원장 _____ (인)

위 원 _____ (인)

위 원 _____ (인)

위 원 _____ (인)

Abstract

Frustrated magnets have been a fruitful playground for exploring new states of matter. Contrary to ordinary magnets which have collinear ground states, competing interactions in frustrated magnets cannot be satisfied simultaneously, and it leads to accidental ground state degeneracies of classical ground states. Such competing ground states result in sensitivity to additional perturbations, which might induce peculiar effects on the ground states and excitations.

Arguably, the simplest model magnetic system with geometrical frustration is a two dimensional triangular Heisenberg antiferromagnet (2D THA). In 2D THA, nonlinear spinwave theories predicted that the excitation spectra shows strong anomalies: significant energy shifts and linewidth broadening of magnon. Direct comparison of such theoretical predictions with experiments are rare, however, due to additional complications such as lattice distortions or spin phonon coupling present in real materials. One such candidate material for 2D THA having distorted triangular Mn spins with moderate spin phonon coupling is hexagonal rare-earth manganites (h-$RMnO_3$).

The magnon spectra have been measured by inelastic neutron scattering on single crystal, and reproduced by anharmonic spinwave calculation with an explicit magnon-phonon coupling. The magnetic excitation spectra of $Y_{1-x}Lu_xMnO_3$ has been measured using MAPS beamline at ISIS, UK and C5 spin polarized spectrometer at Chalk River laboratory, Canada. The overall spectra are quite well reproduced by linear spinwave theory with simple spin Hamiltonian, yet we observed weak additional peaks at high energy which cannot be explained by conventional magnon excitation. Such anomalies motivate us to consider a spin lattice coupling, which affects elastic properties of h-$RMnO_3$, revealed by many previous works. Indeed, a noncollinear spin structure of h-$RMnO_3$ allows a direct magnon-phonon coupling, which can produce additional modes in magnetic excitation spectra. In order to verify this, we measured phonon spectra of $YMnO_3$ above and below T_N, using an inelastic x-ray scattering technique. Below T_N, we observed an additional phonon mode having the same momentum and energy transfer as magnon, clearly indicating the presence of strong magnon-phonon coupling. Similarly, the additional magnon peaks in inelastic neutron scattering experiment have the same momentum and energy transfer as phonons. Such a strong coupling in the wide momentum space is distinct from previous studies of

magnon-phonon coupling confined in narrow regions in reciprocal space. Therefore we call these new hybrid modes magneto-elastic excitation.

In addition to the magnon-phonon coupling, the noncollinear spin structure is also expected to induce the magnon decay of 2D THA h-$RMnO_3$. By analyzing the inelastic neutron scattering data, we observed the evidence of such decays: linewidth broadening of magneto-elastic excitation. In order to reproduce the observed linewidth, we developed a theoretical method to calculate the decay rate of the magneto-elastic modes. The calculation result qualitatively explained the observed momentum dependence of linewidth.

Keywords: triangular antiferromagnet, $RMnO_3$, magnon-phonon coupling, anharmonicity, inelastic neutron scattering, inelastic x-ray scattering, thermal conductivity
Student Number: 2013-30920

Contents

List of Tables

List of Figures

1. Introduction

An interesting property of frustrated magnets is their sensitivity to additional perturbations. Previous works focused on the lifting of ground state degeneracies by quantum fluctuations or spin lattice coupling [1, 2]. Although such perturbations are mostly discussed in the context of ground state properties, quantum fluctuations and spin lattice coupling can also affect the excitation spectrum and properties [3, 4]. With a geometrical frustration on simple two dimensional triangular lattice and a moderate spin lattice coupling, hexagonal $RMnO_3$ is a promising candidate to experimentally investigate the above issues.

1.1 Spontaneous magnon decays in triangular Heisenberg antiferromagnet

Since the discovery of antiferromagnetism by Louis Neél, a fundamental problem in the field of magnetism has been the ground state and the excitation of antiferromagnets. The subject has been extensively studied on two dimensional square lattice antiferromangets after the discovery of high T_c superconductors [5]. Although the ground states of many antiferromagnets are closely described by classical Neél order, quantum fluctuations have nontrivial effects on the low temperature properties, particularly on excitations. Such nontrivial features have induced long debates on the specific nature of these elementary excitations [6, 7].

Frustrated magnetic systems have attracted considerable attention due to possible exotic ground states and excitations. In contrast to ordinary antiferromagnets order at Curie temperatures, some frustrated magnets do not exhibit any order down to the lowest measured temperatures. Such puzzling disordered ground states cannot be described by classical approaches such as Ginzberg-Landau theory and should be relied on extensive numerical methods [8]. Furthermore, excitation spectra in such systems often show anomalous continuum scattering [9, 10].

Triangular lattice antiferromagnets (TLA) are the simplest geometrically frustrated magnets. For Ising model where spins can point only along up or down direction, it is impossible to find a spin configuration that satisfy all the bonds, as shown by figure 1.1. Such competing states are shown to induce a disordered ground state [11]. In more realistic cases, many materials are closely represented

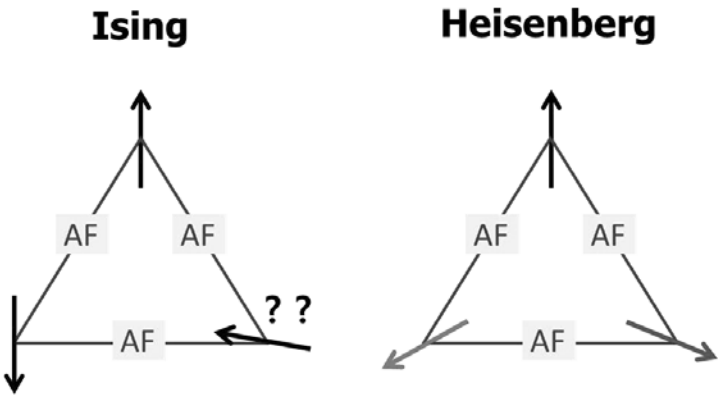

Figure 1.1: Ising(left) and Heisenberg(right) triangular antiferromagnet

by Heisenberg model where spins can point in any direction, as shown by the following Hamiltonian.

$$H = J \sum_{i,j} S_i \cdot S_j \tag{1.1}$$

There were long debates on the true ground state of this model in the quantum limit, due to numerical difficulties originating from frustration [12–15]. However, it was shown much later that unlike the earlier conjecture the ground state of two dimensional triangular Heisenberg antiferromagnet is shown to be a classical-like 120° long range ordered state [16, 17].

Afterwards, interest shifted to the excitation spectra of two dimensional triangular Heisenberg antiferromagnet (2D THA). The elementary excitation of the ordered magnetic system is a *magnon*, which corresponds to the propagation of spin flip excitation. The dispersion relations for these excitations are usually well described by linear spinwave theory. A numerical study on 2D THA, however, predicted after taking into account a nonlinear term that there should be a significant downward shift of magnon energy compared to the linear spinwave dispersion, which emphasizes the role of quantum fluctuations on the magnetic excitation spectra [18, 19]. This result is qualitatively different from square lattice antiferromagnet where excitation energy shifts upward compared to the linear spinwave dispersion [7]. Such a difference is proposed to come from different nature of ordered state in square and triangular antiferromagnet [3, 20]. That is, in the

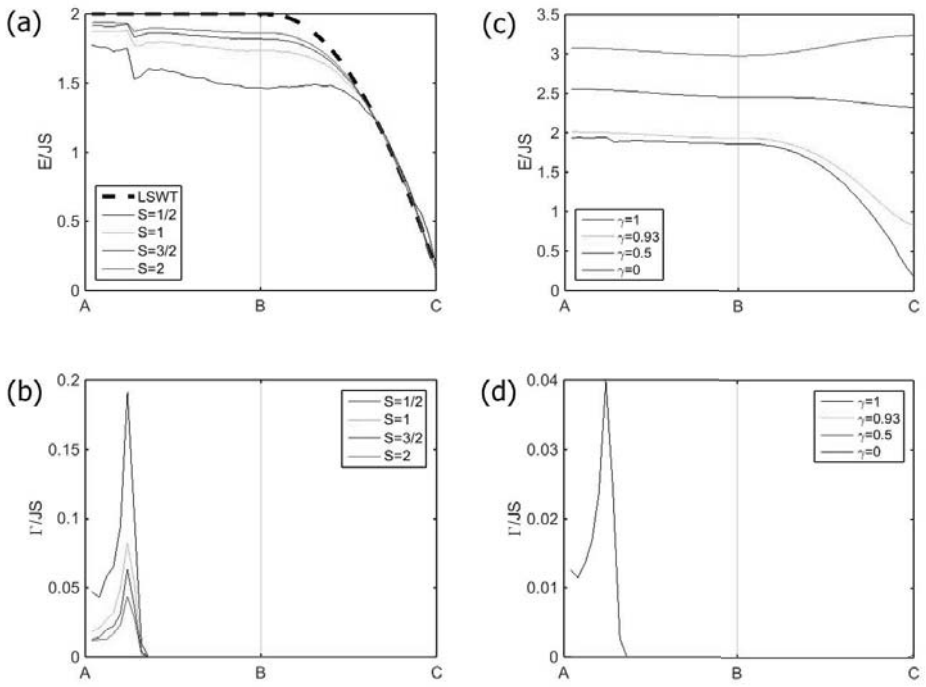

Figure 1.2: Nonlinear spinwave calculation results on the (a,c) magnon energies and (b,d) linewidths for various spins and anisotropy values. $\gamma = 1$ is used for (a,b) and S=2 is used for (c,d). The notation for the reciprocal space follows [18].

noncollinear 120° structure in 2D THA, the leading second order term is cubic which leads to interactions between one and two magnon states. Such interactions are forbidden in collinear magnets. They cause the decay of magnons into two magnon states which results in finite lifetime of magnon even at the zero temperature [3, 21]. This phenomena is called 'spontaneous magnon decays' and has been recently highlighted in the literature [22].

The Heisenberg Hamiltonian can be generalized to a XXZ model, which include easy plane spin anisotropy as often found in realistic cases.

$$H = J \sum_{i,j} \left(S_i^x S_j^x + S_i^y S_j^y + \gamma S_i^z S_j^z \right) \tag{1.2}$$

When γ is smaller than 1, the spins favor the xy direction. Then the calculated spinwave spectra considering cubic and quartic anharmonicities following [21] for

various spins and γ values are displayed by figure 1.2. When spin values are increased, a clear supression of the downward energy shift compared to linear spinwave dispersion is observed. The calculation also shows linewidth broadening present in all spin values, giving evidence of magnon decays. Such decays of a magnon into two magnon states should satisfy the momentum and energy conservation; the linewidth broadening is pronounced at certain reciprocal points where a magnon branch meets a large number of two magnon density of states. When γ is decreased, the spin gap is opened at C point, which increases the overall energy of the two magnon states. This suppresses the condition for the decays and no decays are allowed when γ is less than 0.93 [21].

However, experimental verification of the theoretical prediction has remained considerably challenging for the lack of ideal 2D THA being found in nature. For example, dimensional reduction in Cs_2CuCl_4 [23, 24] and next nearest neighbor interactions in $\alpha-CaCr_2O_4$ [25] made there spin excitation spectra quite different from those predicted for the ideal 2D THA. In this sense, the h-$RMnO_3$ compounds provide a rare opportunity, since their magnon spectra are proven to be similar to those of ideal case [26, 27].

1.2 Triangular antiferromanget hexagonal $RMnO_3$

1.2.1 Crystal and magnetic structure

Hexagonal $RMnO_3$ with R=(Y,Ho,Er,Tm,Yb,Lu) is a first identified geometrical ferroelectric, where the ferroelectric distortion is induced by an ionic size effect. It forms in a layered structure with the $P6_3cm$ space group and belongs to the famous multiferroic hexagonal manganites [28]. As an improper ferroelectric, it undergoes a ferroelectric transition at 1300-1700 K from the centrosymmetric $P6_3mmc$ to the noncentrosymmetric $P6_3cm$. The origin of this ferroelectric transition was shown to be due to the buckling of the MnO_5 bipyramid and the pd hybridization [29, 30], which also results in a trimerization of the 2D Mn triangular lattice.

Upon further cooling, hexagonal $RMnO_3$ compounds exhibit an antiferromagnetic transition near T_N=70-90 K due to super exchange interactions between 2D triangular lattice of Mn^{3+} moments. No structural change has been observed at T_N, so the crystallographic space group remains the same as the $P6_3cm$ space group, from which the magnetic space group can be determined. The magnetic

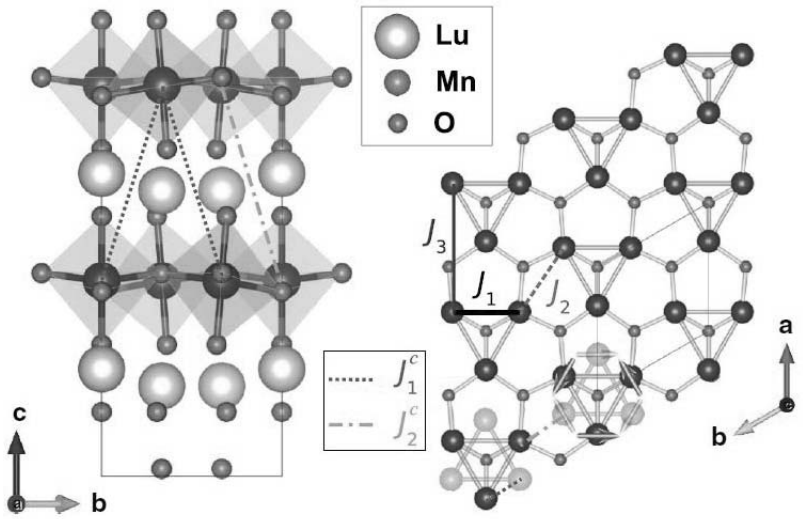

Figure 1.3: The crystal and 120° magnetic structure of hexagonal $LuMnO_3$ taken from [31]. $RMnO_3$ with other rare earth ions has a similar crystal structure.

structure was found to have a propagation vector $\mathbf{k} = (0, 0, 0)$, which gives rise to four possible one-dimensional representations, namely Γ_1 (A1), Γ_2 (A2), Γ_3 (B1), Γ_4 (B2), and two two-dimensional representations, Γ_5 (A) and Γ_6 (B), which are illustrated in figure 1.4. Rather than the Γ symbols, the international (Hermann–Mauguin) notation, where symmetry operators that retain time reversal symmetries are primed or underlined, is also often used in literature, with the following equivalence: $P6_3cm$ (Γ_1), $P6_3\underline{cm}$ (Γ_2), $P\underline{6}3c\underline{m}$ (Γ_3), $P\underline{6}_3\underline{c}m$ (Γ_4), $P6_3$ (Γ_5) and $P\underline{6}_3$ (Γ_6) [32]. The spin arrangements corresponding to these representations are illustrated in figure 1.4. The magnetic structures represented in figure 1.4 that preserve the sixfold rotational symmetry are essentially the 120° structure predicted for a classical Heisenberg antiferromagnet on the triangular lattice, which are either antiferromagnetically ($\Gamma_{1,2,5}$) or ferromagnetically ($\Gamma_{3,4,6}$) coupled along the c axis. For the Γ_2 and Γ_3 representations, the moments can have components along the c axis, which are (anti-)ferromagnetically coupled along the c axis for the (Γ_3) Γ_2 structures. For comparison, the moments are restricted to the hexagonal plane for the Γ_1 and Γ_4 structures. In the case of the one-dimensional representations, the in-plane moments are constrained to be perpendicular ($\Gamma_{1,4}$) or parallel ($\Gamma_{2,3}$) to the a axis, whilst for the two-dimensional representations they may take a constant angle ϕ with respect to the crystallographic axis. The two-dimensional representations may also have moment components along the c axis.

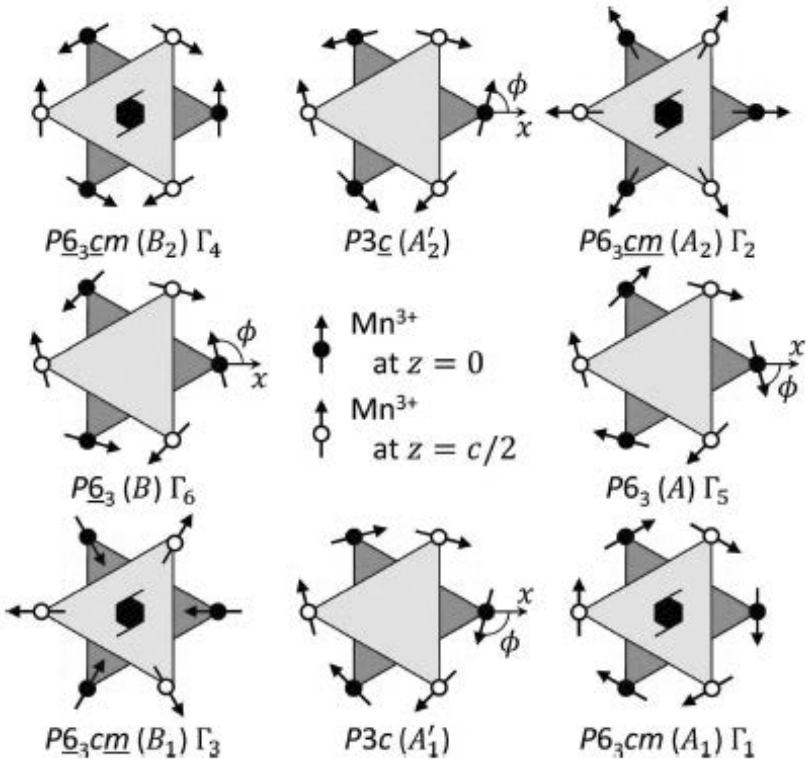

Figure 1.4: Magnetic structures allowed by cystal symmetry taken from [33]

Two main experimental techniques have been used to determine the magnetic structures of h-$RMnO_3$: neutron diffraction and second harmonic generation (SHG). Magnetometry may also be used to infer the presence of a Γ_2 order if a weak ferromagnetic signal is measured, although it is not the case for the h-$RMnO_3$ compounds. Whilst neutron powder diffraction is a common and powerful tool to determine a magnetic structure, it cannot distinguish between the Γ_1 and Γ_3 structures, or between the Γ_2 and Γ_4 structures. This may be resolved by single-crystal polarized neutron diffraction experiments, but the measurements are challenging and have only been reported for $HoMnO_3$ and $YMnO_3$ [34]. On the other hand, SHG can, in principle, distinguish between all the possible structures [35]. For light incident along the c axis, no second harmonic signal implies either one of the Γ_1 or Γ_2 structures, whilst a signal polarized parallel to the a axis indicates the Γ_4 structure and that polarized perpendicular to the a and c axes indicates the Γ_3 structure [32]. Although the Γ_1 and Γ_2 structures can be distinguished using light polarized parallel to the c axis, in this case a second harmonic signal from the ferroelectric polarization also exists [36]. Alternatively, the behavior of the second harmonic signals across a metamagnetic transition under applied magnetic field can serve to elucidate the zero-field magnetic structure [32].

1.2.2 Spin lattice coupling

Although quantum fluctuations are important in understanding the properties of 2D THA as discussed in the section 1.1, alternative mechanisms such as spin lattice coupling may present in real materials. Indeed, spin lattice coupling in hexagonal $RMnO_3$ is extensively studied in the context of magneto-electric coupling. There are two different mechanisms for magneto-electric coupling discussed in literature: coupling of ferroelectric and antiferromagnetic domain walls [37], and a change of bulk polarization due to atomic shifts accompanied by a magnetic order [38].

The first one, clamping of magnetic domains to the ferroelectric domains, is due to a single ion anisotropy coupled to the crystal structure [39]. There are three possible structural rotational directions of the MnO_5 polyhedra in the ab plane, denoted α, β and γ. The ferroelectric domains are then defined by the two possible directions of tilt of the apical oxygen ions, leading to the six possible structural-polarization domains α^{+-}, β^{+-} and γ^{+-}, which form the characteristic vortex structure observed in microscopy measurements [40, 41]. As each pair of antiphase domains α^{+-}, β^{+-} and γ^{+-} are related to a particular magnetic domain due to

the preference of the moments to align parallel or perpendicular to the direction of the Mn displacement as the result of the trimerization distortion, this explains why the magnetic domains are locked to the ferroelectric ones [42].

The second one, the abrupt change of the atom positions below T_N is less explored, yet it has stronger effects on the bulk properties. Anomalies have been observed in the physical properties at T_N: in the elastic constants [43] and dielectric permittivity [44]. The lattice constants and unit-cell volume determined from neutron diffraction experiments have also been observed to deviate from that expected from Debye–Gruneisen model [38, 45], as demonstrated in figure 1.5 (a). Such lattice constant changes accompany large atomic shifts, which reduces the electric polarization below T_N. Yet the origin of such large atomic shifts are elusive and following up x-ray diffraction experiments reported inconsistent results, which puzzles the interpretation of the original neutron diffraction results.

Complementary information can be obtained by measuring the changes in the phonon modes as the antiferromagnetic order develops or by observing the hybridization of magnon and phonon modes. Several IR and Raman measurements have shown that many phonon modes shift in energy below T_N [46–51]. For example, the in-plane phonon mode on R = Y, Er, Lu near 250 cm^{-1} observed by a Raman experiment shows a kink at T_N and hardens as the temperature is further lowered [47]. Further IR studies on the samples with R = Ho, Er, Tm, Yb and Lu as reproduced in figure 1.5 (b) gave similar behavior for the phonon energies, and reflect the change in vibrations of the manganese and oxygen ions within the triangular plane with the onset of the Neél order [51]. As such, vibrational motion should strongly affect a superexchange interaction between Mn-O-Mn bond, the origin of spin phonon coupling has been attributed to an exchange-striction.

Previous studies revealed that a spin lattice coupling of exchange-striction type can induce drastic effects on the ground states and excitations of frustrated magnets [2]. In triangular antiferromagnet, a theoretical study proposed a stabilization of collinear orders in presence of strong exchange-striction [52]. This, however, is not relevant to hexagonal $RMnO_3$, which is well inside the 120° ordered phase. On the other hand, the role of spin lattice coupling on the excitation spectra is largely unexplored.

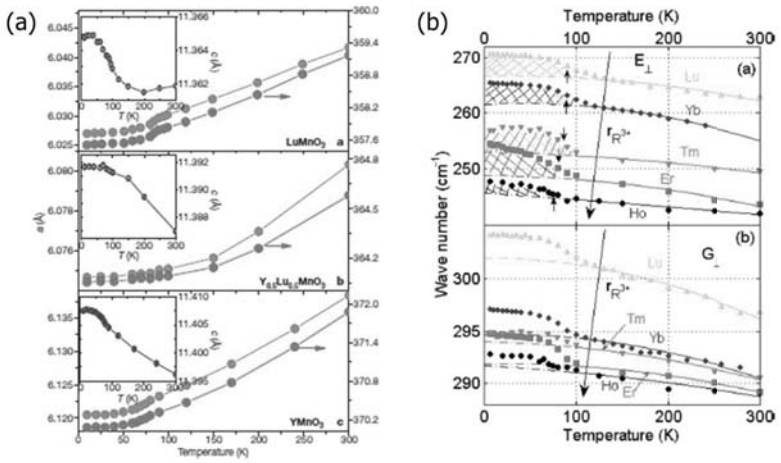

Figure 1.5: Abrubt changes in (a)lattice constants and (b)optical phonon frequencies taken from [38, 51]

1.3 Outline of thesis

In chapter 2, I will introduce experimental techniques to investigate the excitation spectra of hexagonal (Y,Lu)MnO_3. This includes inelastic neutron scattering for the magnetic excitations and inelastic x-ray scattering for the lattice dynamics. I then further describe the details of the time-of-flight inelastic neutron scattering experiments on the MAPS spectrometer at the ISIS facility and the AMATERAS spectrometer in the J-PARC facility, spin polarized triple axis neutron spectroscopy at the C5 spectrometer in the Chalk River facility, and inelastic x-ray scattering experiment on beamline BL43XU in the SPring8 facility.

Next, the calculation details for magnon, phonon and their cross coupling will be covered in chapter 3. The magnon is calculated using linear spin-wave theory from the simple spin Hamiltonian discussed in literature, and the phonon dispersion is calculated using density functional theory. The cross coupling of the magnon and phonon is calculated considering a spin lattice coupling of exchange striction type. Then using a simple one phonon model for the magnon-phonon coupling, the decay rate of the hybrid mode is derived.

Finally, I will compare the experiment and calculation, and discuss the results in chapter 4. The observed magnetic excitation spectra have additional weak signals at high energy, which cannot be reproduced by a simple spin model. The

presence of such peaks as well as the linewidth broadening have been reproduced by nonlinear spin-wave calculations using a Hamiltonian with an explicit magnon-phonon coupling. The validity of such a model has been further confirmed by additional peaks in the phonon spectra.

2. Experimental techniques

In order to measure the spin and lattice dynamics in hexagonal $RMnO_3$, several inelastic neutron and x-ray scattering experiments were conducted. Among $RMnO_3$ family, I focus on nonmagnetic R = (Y,Lu), in order to avoid further complications from rare-earth magnetism. The magnon spectra have been measured by using time-of-flight (ToF) neutron scattering technique and polarized and unpolarized neutron triple-axis spectrometer (TAS), while the phonon spectra have been measured by using a powder inelastic neutron scattering and a single crystal inelastic x-ray scattering experiment.

2.1 Inelastic neutron scattering technique

2.1.1 Basic principle

In order to measure atomic scale excitations, a probe whose wavelength is in the same order of atomic spacings (∼Å) is needed. Also, the excitations such as phonons and magnons, of interest in condensed matter physics, usually have energy scale of 1-100meV order, which determines the necessary resolution of the spectroscopic probe. Finally, to detect magnons and phonons, the probe should be sensitive to nuclei and magnetic moments. Since an inelastic neutron scattering technique satisfies above requirements, it has been a popular tool for studying excitations at the atomic scale. The possible inelastic scattering process with the excitations in solids is determined by the kinematic condition given by the following equations.

$$k_i - k_f = k \tag{2.1}$$

$$\frac{\hbar^2}{2m}(k_i^2 - k_f^2) = \hbar\omega(k) \tag{2.2}$$

The momentum and energy transfered from neutron into the lattice create phonon or magnon with the same momentum and energy. Therefore, the dispersion relation of these excitations can be obtained by measuring the difference between the initial and final neutrons.

Whilst the kinematic constraints described above provide a simple rule for

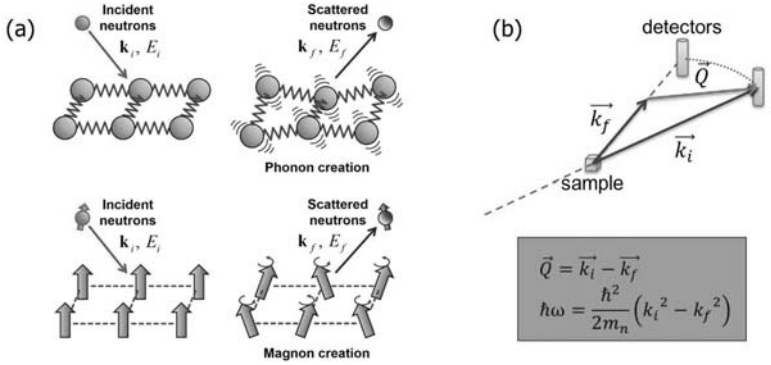

Figure 2.1: (a) A schematic diagram of inelastic neutron scattering process for the phonon and magnon creation [53]. (b) A schematic diagram of the experimental geometry.

the dispersion relation, complete scattering processes of magnons and phonons are described by the scattering cross section. For phonons, the relevant process is neutrons scattered by coherent oscillation of nuclei. When neutrons approach the nuclei of atoms in solid, the scattering process is governed by Fermi pseudopotential, which is theoretically well established. The differential scattering cross section for one phonon emission is given by the following equation [54].

$$\left(\frac{d^2\sigma}{d\Omega dE'}\right)_{1ph} = \frac{8\pi^3 k_f}{2v_0 k_i} \sum_s \sum_\tau \frac{1}{\omega_s} \left| \sum_d \frac{b_d}{\sqrt{M_d}} exp(-W_d) exp(ik \cdot d)(k \cdot e_{ds}) \right|^2 \times \langle n_s + 1 \rangle \, \delta(\omega - \omega_s) \delta(k - q - \tau) \tag{2.3}$$

Here, b_d is an atomic neutron scattering length, W_d is a Debye Waller factor which characterizes the thermal fluctuation, and e_{ds} is the polarization direction of the phonon mode involved. $\frac{k_i}{k_f}$ factor is due to the conversion from the energy dependence of the cross section to wave vector dependence. Since neutrons have spin $\frac{1}{2}$, they are also scattered by the electron spins in solids mediated by dipolar interaction. In this case, the scattering cross section is determined by spin correlation function as follows [54]:

$$\left(\frac{d^2\sigma}{d\Omega dE'}\right)_{mag} = (\gamma r_0)^2 \frac{k_f}{k_i} \left(\frac{1}{2} g F_m(k)\right)^2 exp(-2W) \sum\nolimits_{\alpha,\beta} (\delta_{\alpha\beta} - k_\alpha k_{beta}) S^{\alpha\beta}(k,\omega) \tag{2.4}$$

Here, F_m(k) is a magnetic form factor determined from the spatial distribution of the atomic magnetic moment, the first term inside the summation is polarization factor and the second term is the Fourier transform of a time dependent spin correlation function which is given by the following equation.

$$S^{\alpha\beta}(k,\omega) = \sum\nolimits_{i,j} exp(ik \cdot (d_i - d_j)) \int_{-\infty}^{\infty} exp(i\omega t) \left\langle S_i^\alpha(0) S_j^\beta(t) \right\rangle dt \tag{2.5}$$

Such scattering cross sections directly determine the intensity of the scattered neutrons I(Q,ω) when they scatter with magnons or phonons. The detailed calculation of phonon and magnon cross section using equations 2.3 and 2.5 will be covered in Chapter 3.

In order to determine the magnon and phonon dispersion of the crystal, it is important to have a way to distinguish the two types excitations in measurements. Fortunately, this naturally occurs in most magnetic solids due to the form factor difference of magnons and phonons. For the phonon scattering, the form factor is constant as a function of momentum transfer due to small size of the nuclei involved for the scattering process. Usually, the scattering cross section of phonon is proportional to square of the momentum transfer due to the $k \cdot e_{ds}$ term in the equation 2.3. On the other hand, the magnetic form factor F_m(k) is a rapidly decreasing function of the momentum transfer. Such difference makes the magnon and phonon signals dominant in the low and high momentum transfer regions, respectively. For example, the magnetic form factor of Mn^{3+} in hexagonal $RMnO_3$ shown by figure 2.2 shows that magnetic signals become less than 10% when the momentum transfer Q is higher than 5 $Å^{-1}$.

2.1.2 Time-of-flight(ToF) neutron scattering technique

There are two main methods for measuring inelastic neutron spectra: triple axis spectroscopy (TAS) and time-of-flight (TOF). The time of flight method will be described in this section. In this method, the energy of the neutrons is determined

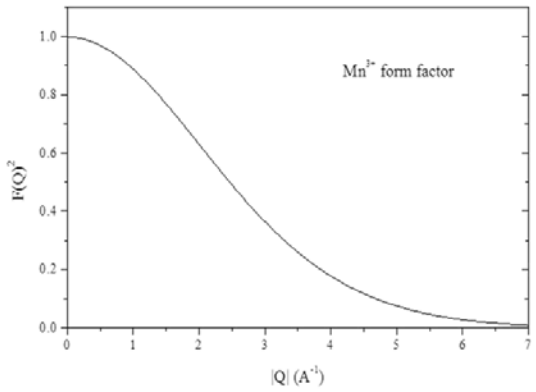

Figure 2.2: Magnetic form factor of Mn^{3+}

by the time they reach the detector. This requires a pulsed neutron source to set the starting time for a bunch of neutrons. This is most efficiently achieved with a neutron spallation source, where protons are accelerated in a linear accelerator and collide into a tungsten or mercury target at regular intervals. The high kinetic energy of the protons causes a series of fast reactions within the nuclei of the target atoms called an intranuclear cascade which results in the ejection of smaller nucleons such as neutrons of light nuclei. Furthermore, the nuclei are left in an excited state from which it decays by releasing more neutrons. These neutrons however have very high kinetic energy, in the MeV range whereas meV range is needed for studying excitations in condensed matters, so the produced neutrons are moderated with light atoms [55]. After that, neutrons with particular energies can be selected with the Fermi chopper. When the chopper rotates, only the neutrons with a particular velocity can pass a straight path through the chopper blades. Finally, the time of flight technique is schematically shown by the figure 2.3. The time spent by the neutron while it travels from the sample to the detector is determined by its scattered energy. Since the energy of the neutrons before interacting with the sample is fixed, this tells us the energy the neutrons gain or lose to the sample, and hence the energies of the excitations which scattered it. Also, the position-sensitive detectors provide the direction of the momentum of the neutron. Therefore, it is possible to accurately quantify the momentum and the energy transfered from the neutron to the sample. The standard repetition rate multiplication (RRM) method is an advanced form of TOF method. In this

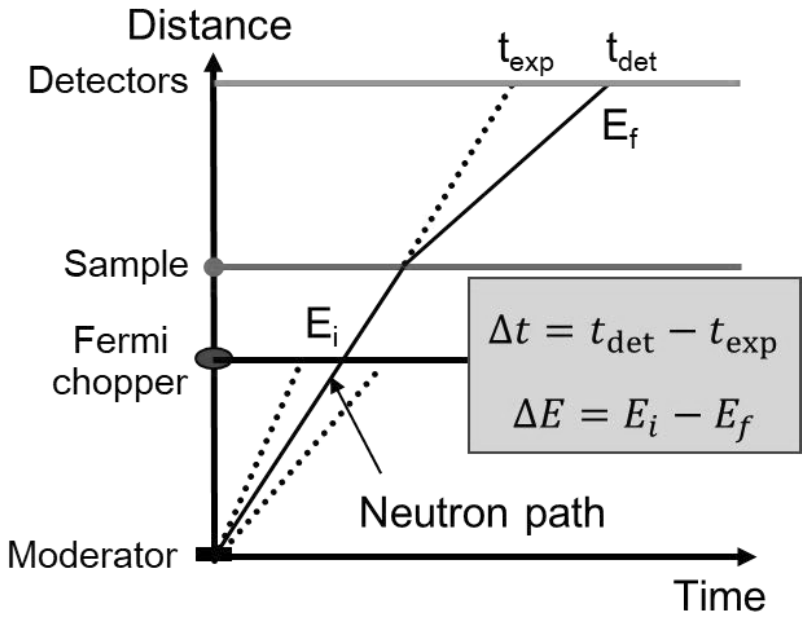

Figure 2.3: Neutron trajectory in ToF inelastic neutron scattering technique

method, several energies of neutrons are selected by the Fermi chopper. This is possible because slow neutrons arrive later than fast neutrons at the sample and allows the detector to separately detect the signals with different incident energies if the incident energies are well selected [55].

2.1.3 Measurement at ToF neutron spectometer MAPS

In order to map out the magnon spectra in hexagonal $RMnO_3$, inelastic neutron scattering experiments have been performed on single crystals of $YMnO_3$, $Y_{0.5}Lu_{0.5}MnO_3$ and $LuMnO_3$ using MAPS beamline at ISIS, UK. MAPS beamline is a first chopper spectrometer using the ToF method to measure the whole bandwidth of magnetic excitations in a single crystal. Most of its detectors are located near the direct beam as shown by figure 2.4 and therefore the momentum coverage is relatively small compared to other modern ToF spectrometers. This, however, is enough for measuring magnetic excitations that appear at low momentum ranges. For $LuMnO_3$ case, the incident energy was 40 meV for the ToF measurement, with the chopper speed set at 250 Hz resulting in the energy resolution of 0.43 meV to 1.36 meV depending on the energy transfer, and the sample

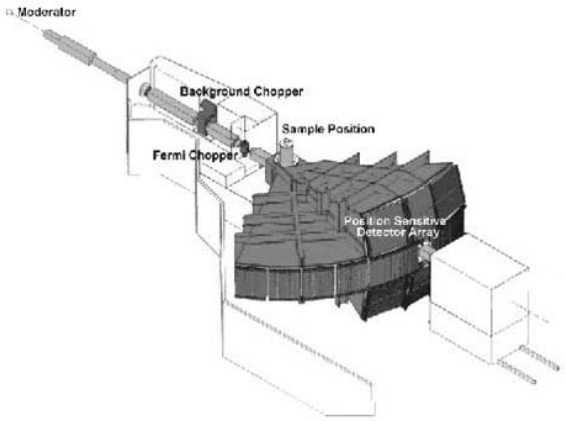

Figure 2.4: Structure of ToF neutron spectrometer MAPS

was mounted with the (HHL) scattering plane horizontal and k_i along (001), such that the (HK0) plane is imaged on the (vertical) detectors. Therefore, the data collected contains three dimensional information - two for the momentum space and one for the energy, as shown by figure 2.5. Such two dimensional momentum space information is enough for $LuMnO_3$, since it has a two dimensional layered structure. The Horace software was used for the data analysis and the result is shown by figure 2.5. The measured data show the clear signature of magnon dispersion up to 20 meV indicated by strong neutron intensities along particular lines in the q-E space. For the other two compounds $YMnO_3$ and $Y_{0.5}Lu_{0.5}MnO_3$, the incident neutron energies are 30 and 35 meV, the samples are rotated along (HHL) plane during the measurement, so that the three dimensional momentum information is obtained. However, the data are summed along the c*-axis for the analysis, which results in a similar data structure with the $LuMnO_3$ case.

2.1.4 Measurement at ToF neutron spectometer AMATERAS

Inelastic neutron scattering experiments were also carried out at the J-PARC facility using the AMATERAS beamline with powder samples of $YMnO_3$ and $LuMnO_3$. AMATERAS is a cold neutron disk choper spectrometer which is specialized for measuring low energy excitations. The standard repetition rate multiplication (RRM) method was used with incident beam energies of 42, 15, 8, and 5 meV. In order to check the temperature dependence of the excitation spectra, the temperature was varied from 10 to approximately 150 K in steps of 5 K. The result

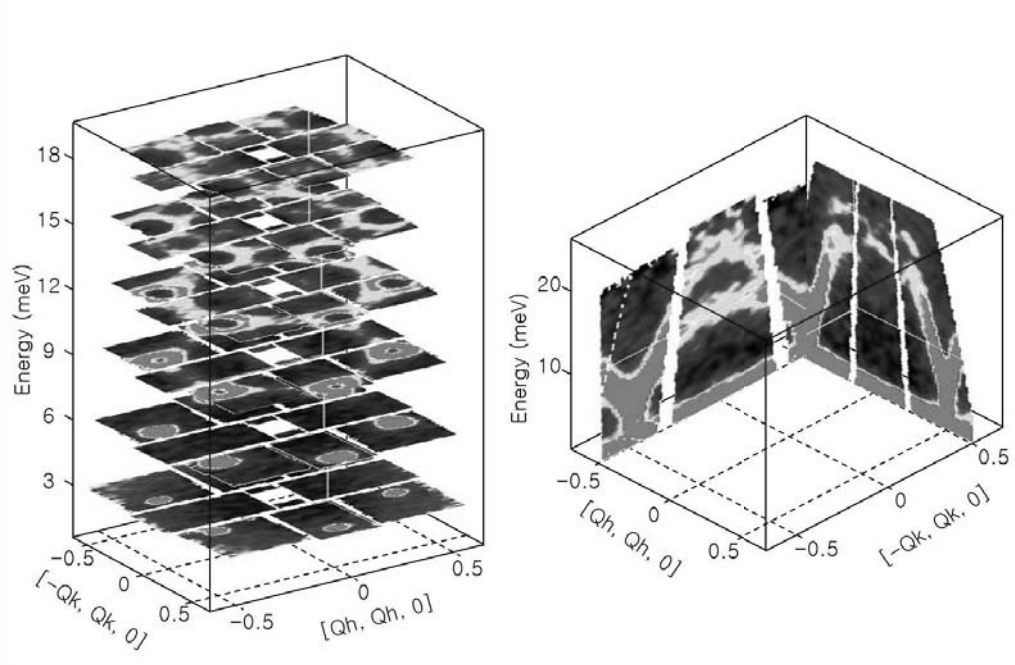

Figure 2.5: Three dimensional data on $LuMnO_3$ obtained by ToF inelastic neutron scattering, in (left)constant energy cuts and (right)constant q cuts.

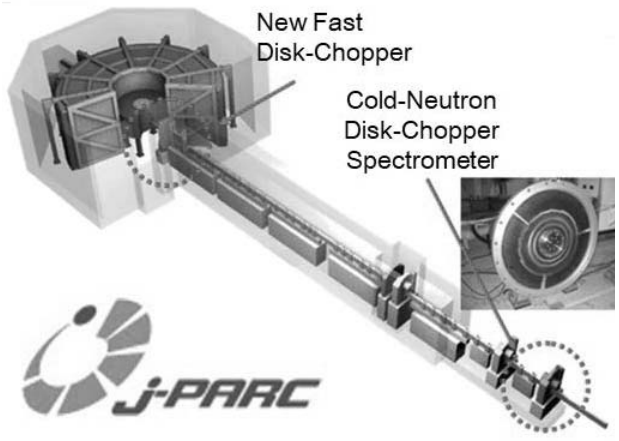

Figure 2.6: Structure of ToF neutron spectrometer AMATERAS

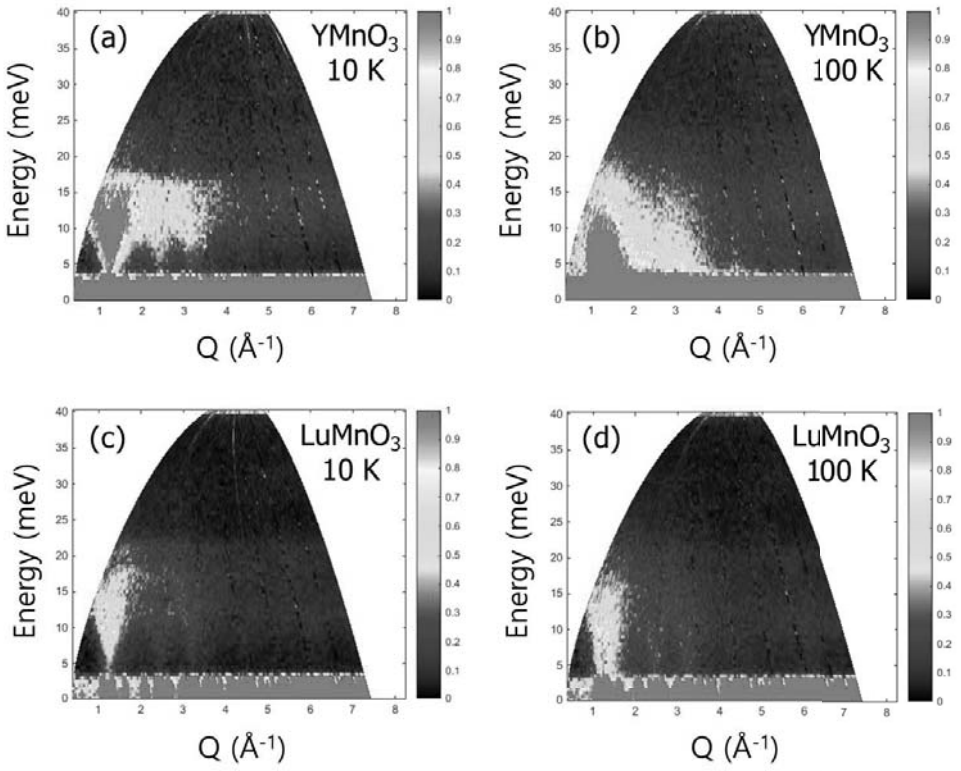

Figure 2.7: The powder inelastic neutron scattering result using AMATERAS for (a,b)$YMnO_3$ and (c,d)$LuMnO_3$ at (a,c)10 K and (b,d)100 K.

for the both compounds at 10 K and 100 K are shown by figure 2.7. The graphs indicate the number of neutrons at given energy and momentum transferred from the neutron to the sample. Since powder samples were used, no information on the direction of the momentum transferred can be obtained. This is the reason why only the magnitude of the momentum transfer vector is indicated in the graphs. The data indicate strong magnetic signal at Q$\sim$1 Å^{-1} which is slightly suppressed at 100 K. At the high momentum transfer above 5 Å^{-1}, the spectra is dominated by phonon signals due to small magnetic form factor shown by figure 2.2.

2.1.5 Polarized triple axis spectroscopy

In the previous sections, I introduced the neutron scattering processes for unpolarized neutrons. By using spin polarized neutrons, additional information can be

obtained, such as the ratio of magnetic and nuclear scattering cross section and each component of spin correlation function shown by equation 2.5. The basic elements of the polarized neutron triple-axis spectrometer(TAS) is shown by figure 4.7. Compared to ToF spectrometer, the advantage of TAS is that one can focus on certain momentum and energy transfer, and therefore can obtain better statistics with improved resolution. This is why TAS is favored for spin polarized experiments which significantly reduce the neutron flux and needs more elements for the spin polarization. A common technique for neutron spin polarization uses a Bragg diffraction from magnetized monochromators. This requires a certain ratio of nuclear and magnetic scattering cross section, which completely removes scattering from neutrons with up(+) or down(−) spins. Then the magnetic field is applied along the beam path from spin flipper in order to maintain the neutron spin polarization. This setup enables one to measure the magnetic scattering cross section in spin flip (+− or −+) and non spin flip (++ and −−) channels.

The differential cross section for polarized neutrons is given by [56]:

$$\left(\frac{d^2\sigma}{d\Omega_f dE_f}\right)_{s_i s_f} = \frac{k_f}{k_i}\sum\nolimits_{i,f} P(i)\left|\left\langle f\left|\sum e^{iQ\cdot r_l}U_l^{s_i s_f}\right|i\right\rangle\right|^2 \delta\left(\hbar\omega + E_i - E_f\right) \qquad (2.6)$$
$$U_l^{s_i s_f} = \left\langle s_f\left|b_l - p_l S_{\perp l}\cdot\sigma + B_l I_l\cdot\sigma\right|s_i\right\rangle$$

Here, $S_\perp$ denotes the spin component perpendicular to the momentum transfer, P is the neutron polarization direction and I is a nuclear spin. From equation 2.6, it is evident that nuclear scattering can be measured only for a non spin flip channel. For the elastic process, the possible matrix elements are as follows [56]:

$$\begin{aligned} U^{++} &= b - pS_{\perp\zeta} + BI_\zeta \\ U^{--} &= b + pS_{\perp\zeta} - BI_\zeta \\ U^{+-} &= -p\left(S_{\perp\xi} + iS_{\perp\zeta}\right) + B\left(I_\xi + iI_\zeta\right) \\ U^{-+} &= -p\left(S_{\perp\xi} - iS_{\perp\zeta}\right) + B\left(I_\xi - iI_\zeta\right) \end{aligned} \qquad (2.7)$$

Here, ζ is the direction parallel to the neutron polarization direction and ξ is the direction perpendicular to both momentum transfer Q and neutron polarization direction. There are two different experimental configurations for the

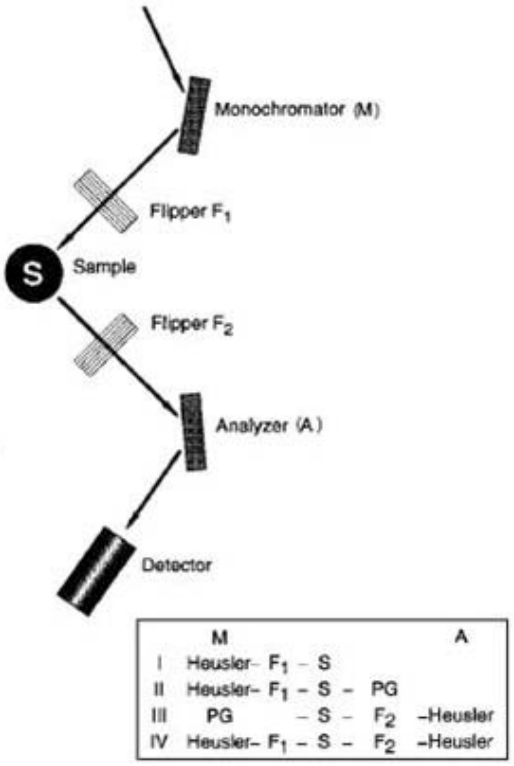

Figure 2.8: Basic layout of a triple-axis spectrometer with polarization analysis capabilities taken from [56].

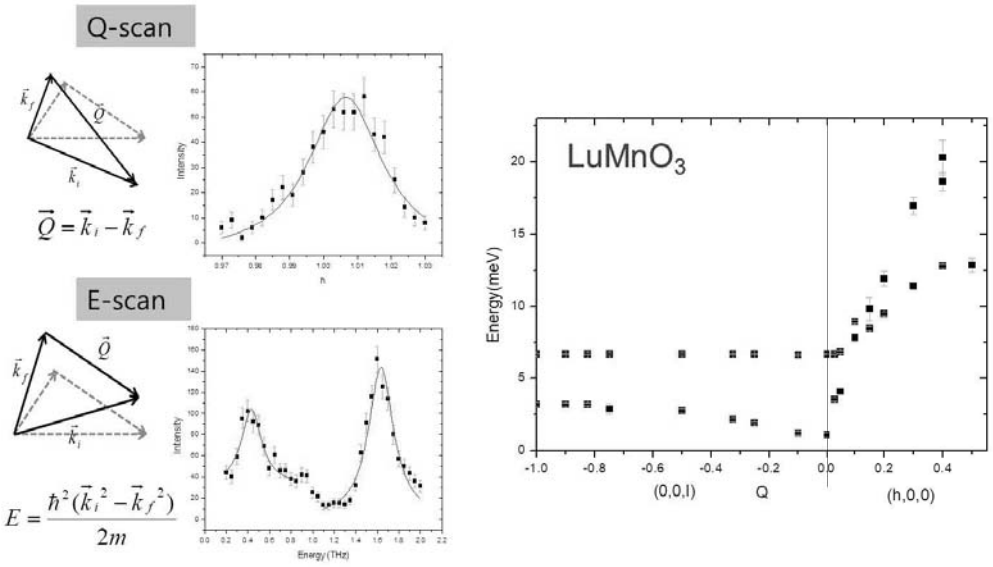

Figure 2.9: Spinwave dispersion of $LuMnO_3$ measured using C5 triple-axis spectrometer at Canadian Neutron Beam Center, Chalk River, Ontario.

polarization analysis: horizontal and vertical spin polarization. In the horizontal case, the neutron spin polarization direction ζ is parallel to Q. Therefore, $S_{\perp\zeta}$ is zero and nuclear cross section and magnetic cross section separately appear in the non spin flip and spin flip channels, respectively. For the vertical case, ζ is perpendicular to Q, and therefore $S_{\perp\zeta}$ appears in both channels. This is also applied to inelastic scattering case, where static spin directions in equation 2.7 is replaced by polarization direction of spin-wave modes.

First, the spin-wave dispersion of $LuMnO_3$ was measured using C5 triple-axis spectrometer with unpolarized neutrons at Canadian Neutron Beam Center, Chalk River, Ontario. A scattering plane (H0L) was used for the measurement, with the following spectrometer configuration: 0.55°-PG(002)-0.48°-sample-0.55°-PG(002)- 1.2°-detector, where the angles denote horizontal collimation and PG(002) is the Bragg reflection used for the monochromator and analyzer. The spinwave dispersion relation is obtained by fitting the E scan. In addition to the in-plane spin-wave dispersion up to 20 meV measured from ToF measurement described in section 2.1.3, small dispersion along (0 0 l) direction is observed. This indicates that magnetic ions in $LuMnO_3$ are not entirely two dimensional and small inter layer interactions present. A polarized inelastic neutron scattering ex-

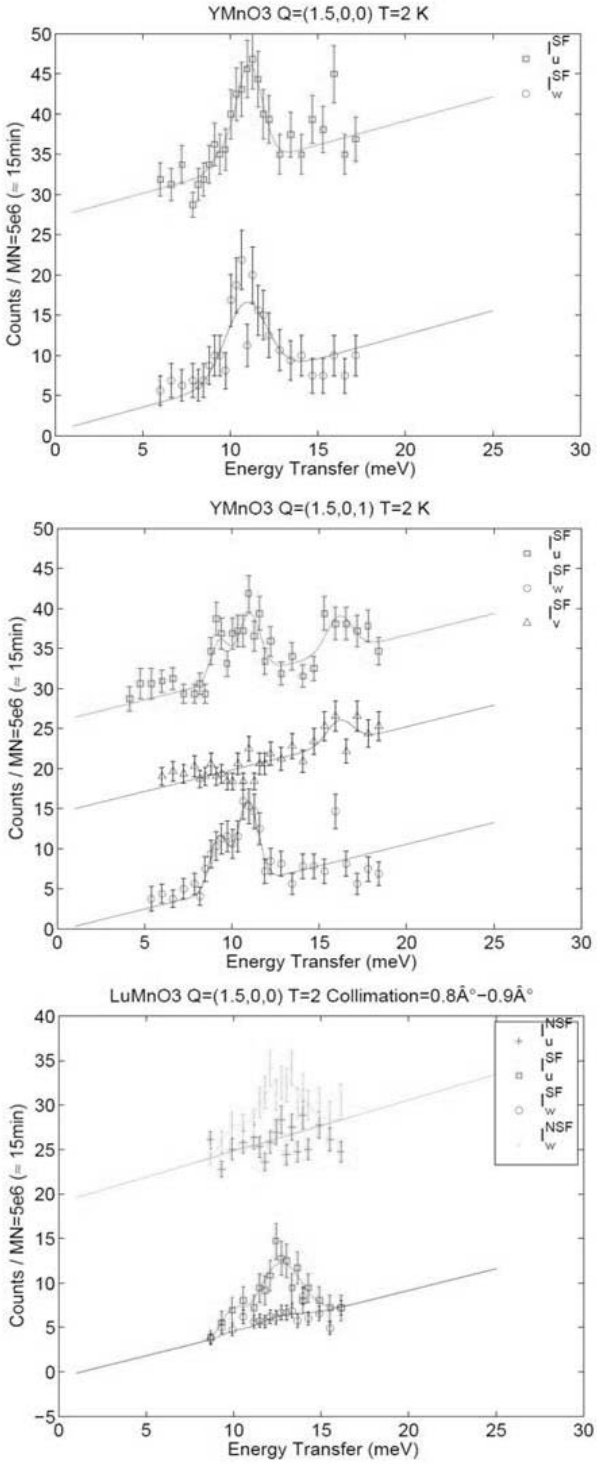

Figure 2.10: Polarized inelastic neutron scattering results for $YMnO_3$ and $LuMnO_3$ at B point with several different configurations for polarization analysis.

periment on $YMnO_3$ and $LuMnO_3$ has been performed using the same beamline. A vertically focusing Heusler and two pyrolytic graphite filters were used as an analyzer. A five coil assembly has been used to control the field direction, and the final energy has been fixed to 13.7 meV. We performed the polarization analysis of the bottom mode at the B point. In figure 2.10, u,v,w denotes different polarized neutron spin directions. u is a direction parallel to the momentum transfer Q, w is a direction in ab plane(c-axis) perpendicular to Q for $YMnO_3$($LuMnO_3$) and v is the direction perpendicular to both u and w. From the relations in equation 2.7, the polarization of the low energy spin-wave mode at about 10-12 meV is identified to be parallel to c-axis.

2.2 Inelastic x-ray scattering technique

2.2.1 Basic principle

The inelastic neutron scattering studies on the magnon and phonon spectra of $RMnO_3$ are covered in section 2.1. The phonon spectra was, however, measured using powder samples, and therefore the directional information was lacking. Inelastic x-ray scattering(IXS) is an alternative method to measure the phonon spectra with a good momentum resolution and nearly no intrinsic background. It also inherently enables excluding magnetic signals, which ensures that the measured dispersion is entirely from phonons. The phonon cross section for inelastic x-ray scattering process is given as follows [57]:

$$\left(\frac{d^2\sigma}{d\Omega dE'}\right)_{1ph} = \sum_q \sum_s \left| \sum_d \frac{f_d(k)}{\sqrt{2M_d}} e^{-W_d} k \cdot e_{ds} e^{ik\cdot d} \right|^2 \times \langle n_s + 1 \rangle \, \delta(\omega - \omega_s)\delta(k - Q) \tag{2.8}$$

Here, Q is q+τ and $f_d(k)$ is x-ray from factor of atom d. Therefore the main difference of the phonon scattering cross section of neutron and x-ray comes from atomic form factor. It is a constant for neutrons, but a decreasing function for x-rays. Furthermore, the x-ray form factor is proportional to the square of the atomic number, which makes it more sensitive to the vibration of heavy atoms.

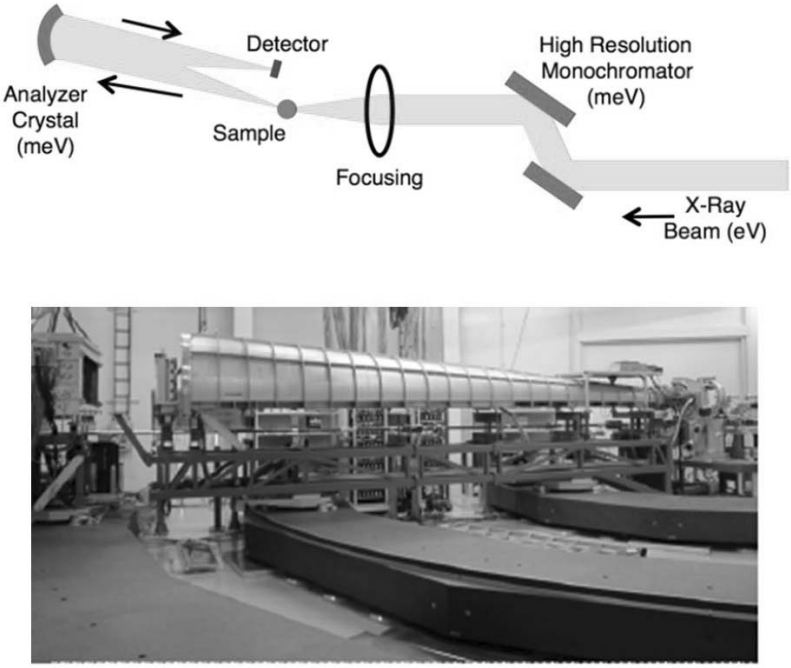

Figure 2.11: (top) Basic elements of inelastic x-ray scattering experiment. (bottom) IXS beamline BL43LXU at SPring8. Reprinted from [58]

2.2.2 IXS experiment on BL43LXU at SPring8

The inelastic x-ray scattering experiments on $YMnO_3$ and $LuMnO_3$ single crystals of $10\times10\times1$ mm^3 size have been carried out using BL43LXU at SPring8, Japan. A schematic of IXS and a photograph of BL43LXU spectrometer is shown by figure 2.11. A measurement usually proceeds by (1) moving the spectrometer two-theta arm (which holds the analyzer - or analyzer array) so the analyzer will intercept the scattered radiation at the momentum transfer of interest, and then (2) scanning the energy of the incident beam while holding the analyzer energy (and position) constant. In order to get high resolution at analyzer crystals, rather large (10m scale) spectrometers are required. The resulting momentum and energy resolution is 0.05 Å^{-1} and 1.5 meV respectively. Although energy resolution is worse than neutron which can be less than 1 meV, momentum resolution is about twice as much better. Moreover, BL43LXU uses 24 analyzer crystals, which enables simultaneous measurement at 24 different Q positions.

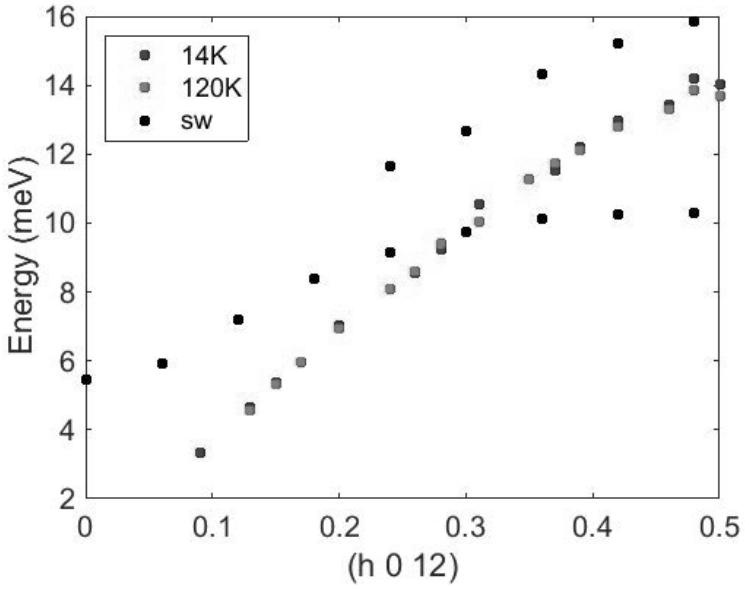

Figure 2.12: IXS result for $YMnO_3$ along (h 0 12) obtained above(red) and below(blue) T_N plotted together with the known spinwave dispersion(black) [59].

Two different plate-like single crystals of $YMnO_3$ have been measured, whose normal direction is (110) and (001) respectively. Since the momentum transfer of incident and scattered beam is nearly parallel to the normal direction, the two different configurations are for measuring at the in-plane and out-of-plane momentum transfer. The result of the latter case with a known spin-wave dispersion relation is summarized by figure 2.12. For the momentum transfer Q, the scattering cross section is maximized for phonon modes with polarization direction parallel to Q, according to equation 2.8. Therefore, the result shows an acoustic phonon mode polarized along the c-axis. Surprisingly, no signatures of magnon-phonon coupling previously reported [59, 60] are found. The phonon dispersion relation above and below $T_N = 75$ K is almost identical and no gap opening at Q=0.175 [59] is observed. This is unlikely to be due to the different cross-sections of neutrons and x-rays, since the mode splitting should equally affect both experiments. Therefore, the gap opening observed by inelastic neutron scattering may be caused by complicated momentum resolution effects or contributions from magnetic scattering. But these scenarios cannot explain the polarized inelastic neutron scattering experiment [60] and further investigation is required to resolve the discrepancy between the neutron and x-ray results.

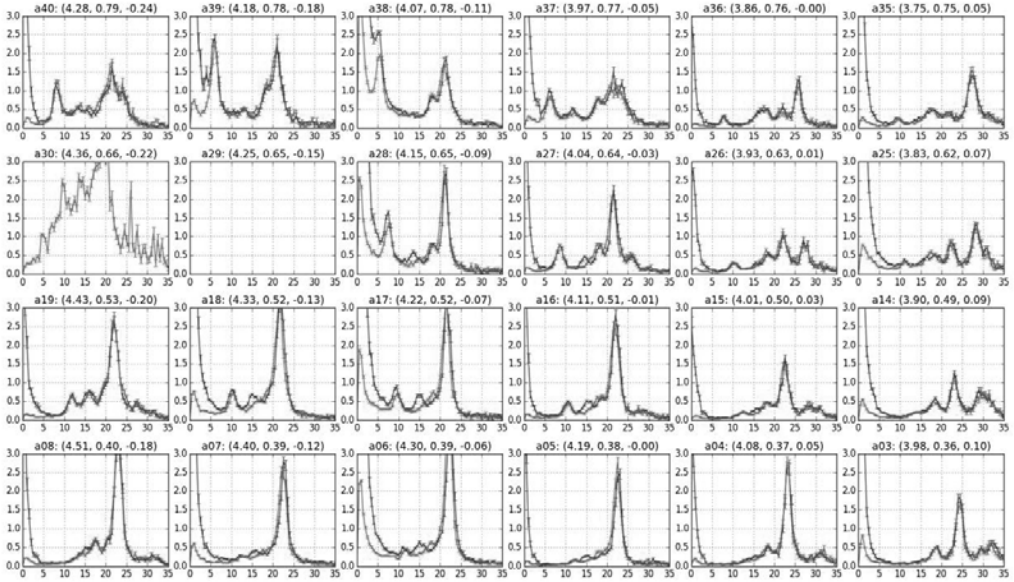

Figure 2.13: IXS result for $YMnO_3$ near Q=(4 0.5 0) at 120 K(red) and 14 K(blue).

The result for the former case, when the normal direction is (110), is shown by figure 2.13. The measured phonon modes should be polarized along the ab plane, contrary to the previous configuration. Compared to the phonon spectra above T_N, the spectra below T_N at several Q positions show clear new peaks around 15 meV. Interestingly, this new peaks have energies of the zone boundary magnon mode shown by figure 2.12. This result is analogous to the inter-locking of phonon mode to the magnon energy, observed from previous inelastic neutron scattering [59], and therefore it is a strong evidence of magnon-phonon coupling. Note however that the polarization direction of the involved phonon mode is different. Similar features are also observed for $LuMnO_3$ as shown by figure 2.14, at slightly different Q positions.

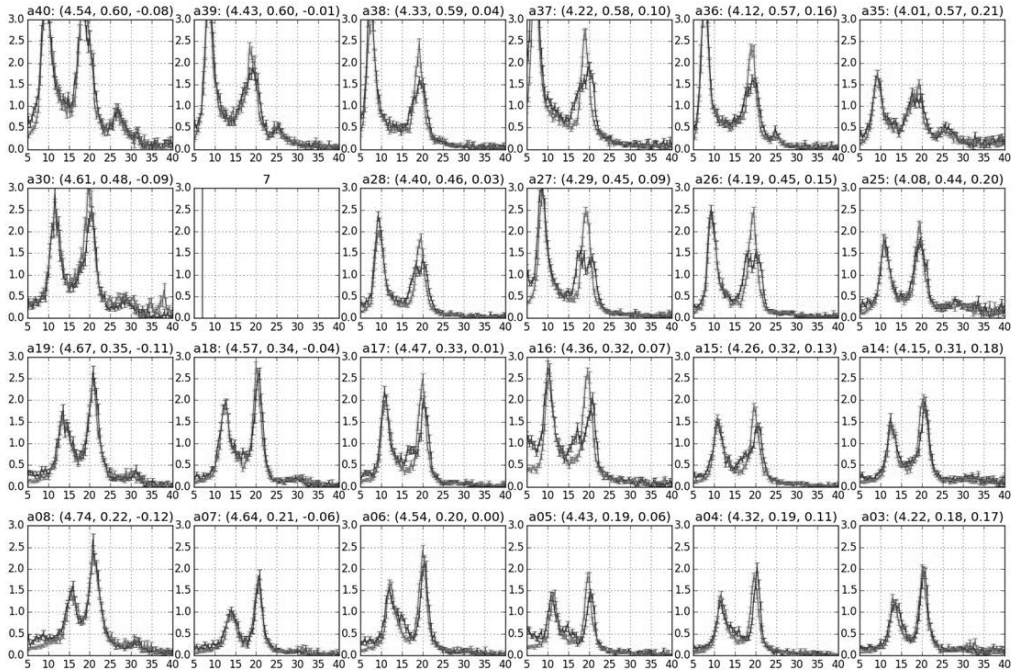

Figure 2.14: IXS result for $LuMnO_3$ near Q=(4.33 0.33 0) at 120 K(red) and 14 K(blue).

3. Calculation of magnon-phonon coupling and decay rate

3.1 Calculation of magnon and phonon

In order to describe magnon and phonon spectra measured for $YMnO_3$ and $LuMnO_3$, a linear spinwave calculation and a density functional theory(DFT) phonon calculation are performed. Then magnon-phonon coupling observed from the experiment, which is discussed in chpter 2, is calculated considering particular spin lattice coupling mechanisms. Finally, the decay rate of the coupled mode is calculated.

3.1.1 Density functional theory phonon calculation

Phonons are quantized portions of energy in lattice vibration waves. The properties of these waves are described in the reciprocal spaces. The general form of phonon Hamiltonian and the displacement vector of the j-th atom in the l-th unit cell are given by:

$$\begin{aligned} H_{ph} &= \sum\nolimits_k X_{ph}^{\dagger}(k) \begin{pmatrix} \Omega & 0 \\ 0 & \Omega \end{pmatrix} X_{ph}(k) \\ X_{ph}(k)^T &= \begin{pmatrix} b_{k1} & \dots & b_{k\lambda} & \dots & b_{-k1}^{\dagger} & \dots & b_{-k\lambda}^{\dagger} & \dots \end{pmatrix} \\ \Omega &= \begin{pmatrix} D_k & 0 \\ 0 & D_k \end{pmatrix}, \qquad D_k = \begin{pmatrix} \frac{\hbar\omega_{k1}}{2} & 0 \\ 0 & \ddots \end{pmatrix} \\ U_{j,l} &= \sqrt{\frac{\hbar}{2m_j\omega_{k\lambda}}} \sum_{k,\lambda} V_{j,k\lambda} e^{ik\cdot(R_l+r_j)} \left(b_{k\lambda} + b_{-k\lambda}^{\dagger}\right) \end{aligned} \tag{3.1}$$

where R and r indicate the unit cell and atom positions, while λ is a band index. The phonon frequencies $\omega_{k\lambda}$ and eigenvectors V_j,k_λ of $Y_{1-x}Lu_xMnO_3$ have been calculated using the PHONOPY code [61] based on the force constant method [62]. The force constants were constructed by means of a supercell approach based on the density functional perturbation theory (DFPT) [63], implemented in the VASP code. It is well-known that the highly-localized levels

such as Mn-3d orbitals are not well described by normal DFT calculations, and thus we applied the Perdew Burke-Ernzerhof (PBE) method [64] including U in order to restore the strong electron-electron exchange-correlation effect [65]. This method was employed for the better description of the Mn-3d orbital in $RMnO_3$. Specifically, we used the value of U for the 3d orbital of Mn as 4 eV, which is slightly larger than 2.6 eV estimated from previous calculations [66]. Then, we constructed a rhombohedral-shape supercell, corresponding to 3 unit cells containing 90 atoms. Although manganese spins couple antiferromagnetically, we used a ferromagnetic spin structure to preserve the crystal symmetry. Another way to preserve the crystal symmetry is neglecting the spin character of Mn^{3+} spin, but the associated energy error is much larger for the latter [67]. All the atomic positions were fully relaxed until the Hellmann-Feynman force on each atom was reduced to 0.01 eV/Å.

The phonon dynamical structure factor can be calculated using the equation 2.3, the eigen values and eigen vectors from PHONOPY. We checked that our calculated phonon dispersion along the [H 0 12] direction for $YMnO_3$ is in a good agreement with the result reported in Ref. [59] as shown by figure 3.1. The details of the dynamical structure factor calculations will be revisited in the following sections.

3.1.2 Magnon calculation

Like phonons, magnons are quantized spin waves in magnetically ordered crystals. They are completely described by their dispersion relation $\omega(q)$, where q is the wavevector. Measurements of this dispersion are sufficient to determine the underlying interactions that govern the spin dynamics, such as exchange interactions and single ion anisotropies. The dominant magnetic interaction which determines 120° spin structure is the nearest neighbor super-exchange interaction in the triangular Mn-O layer. Although the Hamiltonian above describes the high energy magnon spectra quite well, the inter layer super-super exchange and single ion anisotropies are necessary to explain the various possible magnetic structures, as shown by figure 1.4. The interlayer interactions determine the angle between the spins in nearest layers and the single ion anisotropies fixes the direction of each spins. The full spin Hamiltonian includes four different exchange parameters (J_1 J_2-J_1'-J_2'), easy plane anisotropy (D_1) and easy axis anisotropy (D_2). Several inelastic neutron scattering experiments reports the magnon dispersion relations

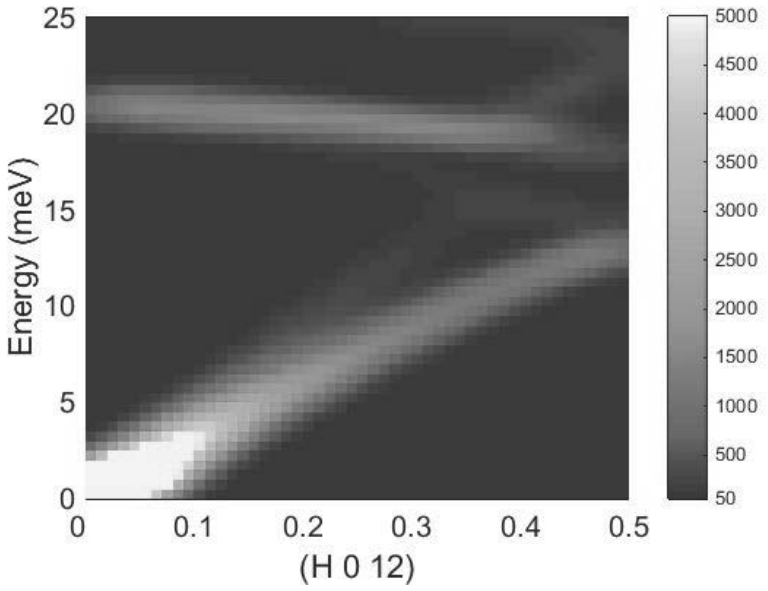

Figure 3.1: Calculated phonon spectra of $YMnO_3$ along (H 0 12) direction

in various h-$RMnO_3$ compounds [26, 27, 68–72]. The interlayer interactions and easy axis anisotropy are more than 100 times smaller than dominant in-plane exchange interactions, evidenced by a small dispersion along the c* direction and a small spin gap [68, 69]. The spin Hamiltonian including the above ingredients is given by:

$$\begin{aligned}\mathcal{H} =& J_1 \sum_{\textbf{intra}} \mathbf{S}_i \cdot \mathbf{S}_j + J_2 \sum_{\textbf{inter}} \mathbf{S}_i \cdot \mathbf{S}_j \\ &+ J_1^c \sum_{\textbf{out intra}} \mathbf{S}_i \cdot \mathbf{S}_j + J_2^c \sum_{\textbf{out inter}} \mathbf{S}_i \cdot \mathbf{S}_j \\ &+ D_1 \sum_i (\mathbf{S}_i^z)^2 + D_2 \sum_i (\mathbf{S}_i \cdot \mathbf{n}_i)^2.\end{aligned} \tag{3.2}$$

where $\mathbf{n}_i$ is a unit vector parallel to the spin direction at i-th site in the Γ_4 configuration (see figure 1.4). The two different exchange parameters J_1 and J_2 are due to the Mn trimerization as shown in figure 3.2. A standard way of calculating magnon spectra for the Γ_4 spin structure will be covered in this section. The other spin configurations can be handled in a similar manner.

The spin operators at six sublattices can be expressed using Holstein-Primakoff

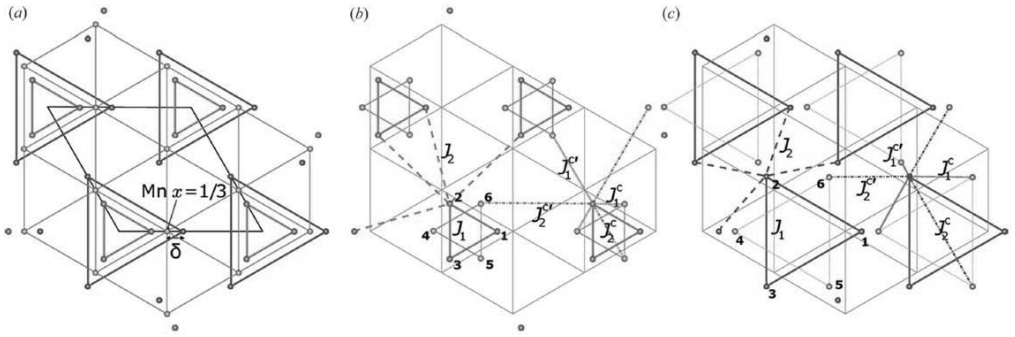

Figure 3.2: (a) Pattern of Mn trimerization with two different values of the Mn x position with Mn ions forming smaller trimers (red) or larger trimers (blue) on the ab plane. The different magnetic exchange interactions are shown for the case of (b) x<1/3 and (c) x>1/3.

operators as shown by the following equations:

$$\begin{aligned} S_i^x &= \frac{\sqrt{2S}}{2i}(a_i - a_i^\dagger) \\ S_i^y &= S - a_i a_i^\dagger \\ S_i^z &= \frac{\sqrt{2S}}{2}(a_i + a_i^\dagger) \end{aligned} \tag{3.3}$$

$$\begin{aligned} S_j^x &= -\frac{\sqrt{3}}{2}(S - a_j a_j^\dagger) - \frac{1}{2}\frac{\sqrt{2S}}{2i}(a_j - a_j^\dagger) \\ S_j^y &= -\frac{1}{2}(S - a_j a_j^\dagger) + \frac{\sqrt{3}}{2}\frac{\sqrt{2S}}{2i}(a_j - a_j^\dagger) \\ S_j^z &= \frac{\sqrt{2S}}{2}(a_j + a_j^\dagger) \end{aligned} \tag{3.4}$$

$$\begin{aligned} S_k^x &= \frac{\sqrt{3}}{2}(S - a_k a_k^\dagger) - \frac{1}{2}\frac{\sqrt{2S}}{2i}(a_k - a_k^\dagger) \\ S_k^y &= -\frac{1}{2}(S - a_k a_k^\dagger) - \frac{\sqrt{3}}{2}\frac{\sqrt{2S}}{2i}(a_k - a_k^\dagger) \\ S_k^z &= \frac{\sqrt{2S}}{2}(a_k + a_k^\dagger) \end{aligned} \tag{3.5}$$

where $i = 1, 4$, $j = 2, 5$ and $k = 3, 6$. After substituting equation (3.3)–(3.5) into equation (3.2) leaving out terms, no higher than quadratic of $a^\dagger$ (creation operator) and a (annihilation operator), and performing Fourier transformation,

the Hamiltonian can be rewritten in the following matrix form:

$$\mathcal{H} = -6\Delta S(S+1)N + \sum_k \mathbf{X}^\dagger \begin{pmatrix} \mathbf{U} & \mathbf{V} \\ \mathbf{V} & \mathbf{U} \end{pmatrix} \mathbf{X} \tag{3.6}$$

where

$$\begin{aligned} \mathbf{U} &= \begin{pmatrix} \mathbf{P} + \Delta \mathbf{I}_3 & \mathbf{Q} + \mathbf{R} \\ \mathbf{Q}^* + \mathbf{R}^* & \mathbf{P}^* + \Delta \mathbf{I}_3 \end{pmatrix}, \\ \mathbf{V} &= \begin{pmatrix} 3\mathbf{P} + D_1 \mathbf{I}_3 & 3\mathbf{Q} \\ 3\mathbf{Q}^* & 3\mathbf{P}^* + D_1 \mathbf{I}_3 \end{pmatrix}, \end{aligned} \tag{3.7}$$

$$\mathbf{X} = \begin{pmatrix} a_{1,k} \\ \vdots \\ a_{6,k} \\ a_{1,-k} \\ \vdots \\ a_{6,-k} \end{pmatrix}, \quad \begin{aligned} \mathbf{P} &= \begin{pmatrix} 0 & A^* & C \\ A & 0 & B^* \\ C^* & B & 0 \end{pmatrix}, \\ \mathbf{Q} &= \begin{pmatrix} 0 & A' & A' \\ A' & 0 & A' \\ A' & A' & 0 \end{pmatrix}, \\ \mathbf{R} &= \begin{pmatrix} B' & 0 & 0 \\ 0 & B' & 0 \\ 0 & 0 & B' \end{pmatrix}, \end{aligned} \tag{3.8}$$

and

$$\begin{aligned} A &= \frac{1}{8}\left[J_1 + J_2\left(e^{-ik\cdot b} + e^{-ik\cdot(a+b)}\right)\right], \\ B &= \frac{1}{8}\left[J_1 + J_2\left(e^{-ik\cdot a} + e^{ik\cdot b}\right)\right], \\ C &= \frac{1}{8}\left[J_1 + J_2\left(e^{ik\cdot a} + e^{ik\cdot(a+b)}\right)\right], \\ \Delta &= \frac{1}{2}\left(J_1 + 2J_2 + 2J_1^c - 2J_2^c + D_1 - 2D_2\right), \\ A' &= \frac{J_1^c}{8}\left(1 + e^{-ik\cdot c}\right), \\ B' &= \frac{J_2^c}{2}\left(1 + e^{-ik\cdot c}\right). \end{aligned} \tag{3.9}$$

Here, a and b denote the lattice unit vectors and $\mathbf{I}_3$ is a 3×3 identity matrix. The numerical diagonalization of the matrix form above results in six magnon modes. The obtained eigenvalues and eigenvectors are used to get the magnon

dispersion and dynamical structure factor as described by [73, 74]. More details on the dynamical structure calculations will be revisited in the following sections.

3.2 Magnon-phonon coupling

3.2.1 Magnon-phonon Hamiltonian

The possible evidence of magnon-phonon coupling observed from inelastic x-ray scattering data, discussed in section 2.2.2 requires calculations which include magnon-phonon coupling. Such coupling should involve a phonon mode polarized in the ab plane, because the anomalies have been observed for such phonon modes and not for phonons polarized along the c-axis. This is consistent with optical studies, which show abrupt change of phonon modes involving the in-plane Mn and O vibrational motion [50]. Here, we consider a spin lattice coupling mechanism of exchange-striction type where exchange energies are modulated as a function of Mn-O bond lengths. Such a proposal may be natural, since the extensive studies on the orthorhombic variant of $RMnO_3$ pointed out exchange-striction as the main spin-lattice coupling mechanism [75, 76]. Whilst the form of the exchange-striction does not give a linear coupling between magnons and phonons in collinear magnets, leaving the single ion magneto-striction as the main mechanism for the magnon-phonon hybridization [77], the linear coupling is allowed in non-collinear spin structures: since the first order variation of the exchange energy with respect to transverse spin fluctuations is nonzero for non-collinear spins [75]. The coupling term for an exchange-striction model is given as follows:

$$H_{mp} = \tilde{\alpha} \sum\nolimits_{ij} \left(e_{O_{ij}i} \cdot U_i + e_{O_{ij}j} \cdot U_j \right) S_i \cdot S_j \tag{3.10}$$

Here, U_i is the displacement vector of i-th manganese atom, $e_{O_{ij}i}$ denotes the unit vector connecting the i-th manganese atom and the neighboring oxygen atoms between the i-th and j-th manganese atoms as shown in figure 3.3, $\tilde{\alpha}$ is the exchange-striction, $\tilde{\alpha} = \frac{\partial J}{\partial r}$, which is naturally made into a dimensionless exchange-striction constant $\alpha = \frac{2d}{J}\tilde{\alpha}$, and d is Mn-O bond length at the equilibrium. We ignore the oxygen vibrations due to a small oxygen DOS below 20 meV, which will be discussed in the following sections. In order to make the Hamiltonian quadratic, since the displacement vectors give linear terms in phonon operators according to equation (3), only linear terms in $S_i \cdot S_j$ should be considered. Af-

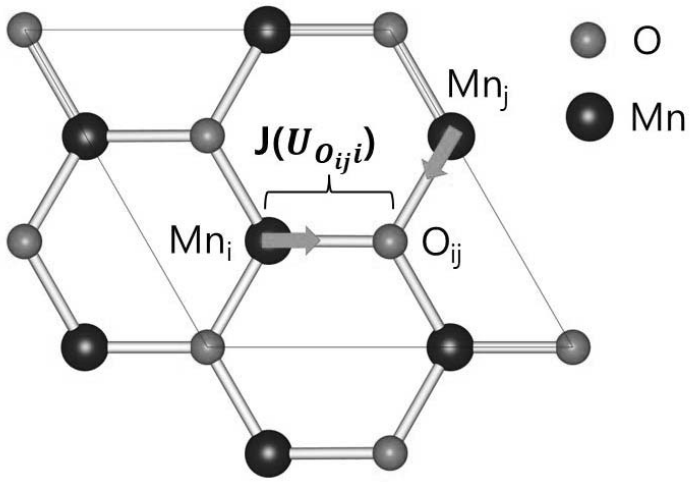

Figure 3.3: The Manganese displacements that most significantly modulate the exchange interactions.

ter substituting the displacement vectors and spin operators into phonon and Holstein Primakoff operators as described above, the magnon-phonon coupling Hamiltonian between i-th and j-th sublattices are given by:

$$\begin{aligned} H_{mp}^{ij} = \frac{i\tilde{\alpha}S}{4} \sum\nolimits_{R_{ij}} \sum\nolimits_{k,\lambda} \sqrt{\frac{3\hbar S}{m\omega_{k\lambda}}} [e_{O_{ij}i} \cdot V_{i,k,}^{*} e^{ik\cdot r_i} (b_\lambda(-k) + b_\lambda^\dagger(k)) \\ \times (a_j(k) - a_j^\dagger(-k)) e^{ik\cdot R_{ij}} - e_{O_{ij}j} \cdot V_{j,k,\lambda}^{*} e^{ik\cdot r_j} (b_\lambda(-k) + b_\lambda^\dagger(k)) \\ \times (a_i(k) - a_i^\dagger(-k)) e^{-ik\cdot R_{ij}}] \end{aligned} \tag{3.11}$$

Then, the total Hamiltonian becomes:

$$
\begin{aligned}
H_{tot} &= S\sum\nolimits_k X_{tot}^{\dagger}\begin{pmatrix} L & -iN^{\dagger} & M & -iN^{\dagger} \\ iN & \Omega & -iN & 0 \\ M & iN^{\dagger} & L & -iN^{\dagger} \\ iN & 0 & iN & \Omega \end{pmatrix} X_{tot} \\
X_{tot}^{T} &= \left(a_{k1}\dots a_{k6} b_{k1}\dots b_{k\lambda}\dots a_{-k1}^{\dagger}\dots a_{-k6}^{\dagger} b_{-k1}^{\dagger}\dots b_{-k\lambda}^{\dagger}\dots\right) \\
N(\lambda,1) &= \frac{1}{8}\sqrt{\frac{3\hbar S}{m_{Mn}\omega_{k\lambda}}}\left(B_{31}\cdot W_{3,k}^{*} - B_{21}ßW_{2,k}^{*}\right) \\
N(\lambda,2) &= \frac{1}{8}\sqrt{\frac{3\hbar S}{m_{Mn}\omega_{k\lambda}}}\left(B_{12}\cdot W_{1,k}^{*} - B_{32}\cdot W_{3,k}^{*}\right) \\
N(\lambda,3) &= \frac{1}{8}\sqrt{\frac{3\hbar S}{m_{Mn}\omega_{k\lambda}}}\left(B_{23}\cdot W_{2,k}^{*} - B_{13}\cdot W_{1,k}^{*}\right) \\
N(\lambda,4) &= \frac{1}{8}\sqrt{\frac{3\hbar S}{m_{Mn}\omega_{k\lambda}}}\left(B_{64}\cdot W_{6,k}^{*} - B_{54}\cdot W_{4,k}^{*}\right) \\
N(\lambda,5) &= \frac{1}{8}\sqrt{\frac{3\hbar S}{m_{Mn}\omega_{k\lambda}}}\left(B_{45}\cdot W_{4,k}^{*} - B_{65}\cdot W_{6,k}^{*}\right) \\
N(\lambda,6) &= \frac{1}{8}\sqrt{\frac{3\hbar S}{m_{Mn}\omega_{k\lambda}}}\left(B_{56}\cdot W_{5,k}^{*} - B_{46}\cdot W_{4,k}^{*}\right)
\end{aligned}
\tag{3.12}
$$

and

$$
B_{lm} = e_{O_{ij}i} e^{ik\cdot(R(j)-R(i))} \tag{3.13}
$$

Here, $W_{i,k,\lambda} = V_{i,k\lambda} e^{ik\cdot r_i}$ and R_{ij} are summarized in the following table, where e_1 = (-1 0 0), e_2 = (1/2 $\sqrt{3}$/2 0), e_3 = (1/2 $-\sqrt{3}$/2 0).

3.2.2 Dynamical spin structure factor

Dynamical spin structure factor is another name for the time-dependent spin correlation function given by equation 2.5 and is directly related to the neutron scattering cross section. From Holstein-Primakoff transformation 3.3, each spin operators can be written by:

$$
S_i^{\alpha} = \frac{\sqrt{2S}}{2}\left(\bar{z}_i^{\alpha} a_i + z_i^{\alpha} a_i^{\dagger}\right) \tag{3.14}
$$

i,j	$e_{O_{ij}i}$	R_{ij}
1,2	e_1, e_2, e_3	0,a,-b
2,3	e_3, e_1, e_2	-a-b,-a,0
3,1	e_2, e_3, e_1	a+b,0,b
2,1	e_3, e_1, e_2	0,-a,b
3,2	e_2, e_3, e_1	a+b,a,0
1,3	e_1, e_2, e_3	-a-b,0,-b
4,5	$-e_1, -e_2, -e_3$	a-b,-b,a
5,6	$-e_3, -e_1, -e_2$	b,0,-a
6,4	$-e_2, -e_3, -e_1$	-a,b,0
5,4	$-e_3, -e_1, -e_2$	b-a,b,-a
6,5	$-e_2, -e_3, -e_1$	-b,0,a
4,6	$-e_1, -e_2, -e_3$	a,-b,0

Table 3.1: $e_{O_{ij}i}$ and Rij between different neighboring spins.

The terms proportional to $S_z = S - a_i a_i^\dagger$ only contribute to the time independent part or elastic part of equation 2.5, therefore neglected here. Then,

$$\left\langle S_{mi}^{\alpha} S_{nj}^{\beta}(t) \right\rangle = \frac{S}{2} \left\langle \left[a_i^\dagger(R_m) a_j(R_m) \right] \begin{bmatrix} z_i^\alpha \bar{z}_j^\beta & z_i^\alpha z_j^\beta \\ \bar{z}_i^\alpha \bar{z}_j^\beta & \bar{z}_i^\alpha z_j^\beta \end{bmatrix} \begin{bmatrix} a_j(R_n,t) \\ a_j^\dagger(R_m,t) \end{bmatrix} \right\rangle \tag{3.15}$$

By numerical diagonalization of the Hamiltonian, Holstein-Primakoff operators can be expressed with magnon operators as shown by the following equation.

$$X_i = \sum\nolimits_\eta T_{i\eta} Y_\eta \tag{3.16}$$

X is given by equation 3.12 and Y is a column vector whose components are quasiparticle creation and annihilation operators. Then,

$$\int_{m,n} e^{ik\cdot(R_n - R_m)} \int dt e^{-i\omega t} \int_{\alpha,\beta=x,y,z} \left\langle S_{mi}^{\alpha} S_{nj}^{\beta}(t) \right\rangle$$

$$= \int dt e^{-i\omega t} \int_{\alpha,\beta=x,y,z} \frac{S}{2} \left\langle \left[a_i^\dagger(-k) \;\; a_j(k) \right] \begin{bmatrix} z_i^\alpha \bar{z}_j^\beta & z_i^\alpha z_j^\beta \\ \bar{z}_i^\alpha \bar{z}_j^\beta & \bar{z}_i^\alpha z_j^\beta \end{bmatrix} \begin{bmatrix} a_j(-k,t) \\ a_j^\dagger(k,t) \end{bmatrix} \right\rangle$$

$$= \int dt e^{-i\omega t} \int_{\alpha,\beta,\mu,\nu,\sigma,\varsigma} \frac{S}{2} \left\langle \left[T_{i+\frac{n}{2},\sigma} \; T_{i,\zeta} Y_\zeta \right] \begin{bmatrix} z_i^\alpha \bar{z}_j^\beta & z_i^\alpha z_j^\beta \\ \bar{z}_i^\alpha \bar{z}_j^\beta & \bar{z}_i^\alpha z_j^\beta \end{bmatrix} \begin{bmatrix} Y_\mu^\dagger T_{\mu,j+\frac{n}{2}}^\dagger e^{i\omega_\mu t} \\ Y_\nu^\dagger T_{\nu,j}^\dagger e^{i\omega_\nu t} \end{bmatrix} \right\rangle$$

$$
\begin{aligned}
=\frac{S}{2}\int_{\alpha,\beta,\mu\leq \mathrm{n}/2,\nu\leq \mathrm{n}/2,\sigma,\varsigma} & z_i^{\alpha}\overline{z}_j^{\beta}T_{i+n/2,\sigma}T^{\dagger}_{\mu,j+n/2}\delta\left(\sigma-\mu\right)\delta\left(\omega-\omega_{\mu}\right) \\
& +z_i^{\alpha}z_j^{\beta}T_{i+\frac{n}{2},\sigma}T^{\dagger}_{\nu,j}\delta\left(\varsigma-\nu\right)\delta(\omega-\omega_{\nu})
\end{aligned}
\tag{3.17}
$$

Here, n=6 is the number of magnetic sublattices, and the following relation have been used:

$$
\left\langle F_iF_j^{\dagger}\right\rangle=\delta_{ij}\left(1+n_j\right),\quad \langle F_iF_j\rangle=0,\quad \left\langle F_i^{\dagger}F_j^{\dagger}\right\rangle=0,\quad \left\langle F_i^{\dagger}F_j=\delta_{ij}n_j\right\rangle \tag{3.18}
$$

F_i is a quasiparticle annihilation operator and n_i is a number density of bosons. Since our interest is the zero temperature structure factor, n_i is set to zero here. Inserting (3.17) to (2.5), the final expression is given by:

$$
\begin{aligned}
& S^{\alpha\beta}\left(k,\omega\right)=\frac{S}{2}\int_{i,j}e^{ik\cdot\left(r_j-r_i\right)}\int_{\alpha,\beta,\mu\leq \mathrm{n}/2,\nu\leq \mathrm{n}/2,\sigma,\varsigma}\left(\delta_{\alpha\beta}-\frac{k^{\alpha}k^{\beta}}{k^2}\right) \\
& \times\left[z_i^{\alpha}\overline{z}_j^{\beta}T_{i+n/2,\mu}T^{\dagger}_{\mu,j+n/2}\delta\left(\omega-\omega_{\mu}\right)+z_i^{\alpha}z_j^{\beta}T_{i+n/2,\nu}T^{\dagger}_{\nu,j}\right. \\
& \left.\times\delta\left(\omega-\omega_{\nu}\right)+\overline{z}_i^{\alpha}\overline{z}_j^{\beta}T_{i,\mu}T^{\dagger}_{\mu,j+n/2}\delta\left(\omega-\omega_{\mu}\right)+\overline{z}_i^{\alpha}z_j^{\beta}T_{i,\nu}T^{\dagger}_{\nu,j}\delta\left(\omega-\omega_{\nu}\right)\right]
\end{aligned}
\tag{3.19}
$$

3.2.3 Phonon dynamical structure factor

The phonon dynamical structure factor is given by:

$$
S_{ph}\left(k,\omega\right)=\int_{m,n,i,j}f_i\left(k\right)f_j\left(k\right)e^{ik\cdot\left(R_m+r_i-R_n-r_j\right)}\int dte^{-i\omega t}\left\langle k\boldsymbol{U}_{i,m}\boldsymbol{U}^T_{j,n}\left(t\right)k^T\right\rangle \tag{3.20}
$$

Here, $f_i\left(k\right)$ is form factor, which is proportional to atomic number z.
Using equation (2.3),

$$
S_{ph}\left(k,\omega\right)=\int dte^{-i\omega t}\left\langle \boldsymbol{k}\widetilde{\boldsymbol{V}}^{*}_{k}\widetilde{\boldsymbol{V}}^{T}_{k}(t)\boldsymbol{k}^T\right\rangle \tag{3.21}
$$

Where $\widetilde{\boldsymbol{V}}_{ik,\lambda}\left(t\right)=\frac{\sqrt{\hbar}f_i}{\sqrt{2m_i\omega_{k\lambda}}}\boldsymbol{V}_{ik,\lambda}\left(b_{k\lambda}\left(t\right)+b^{\dagger}_{-k\lambda}\left(t\right)\right)$ and $\mathbf{k}$ is 1x3N vector which repeats the momentum transfer vector k 3N times.
Using equation (3.16) and (3.18), (3.21) can be rewritten by the following equa-

tion.

$$S_{ph}\left(k,\omega\right)=\left|\left(\boldsymbol{kV}\widetilde{\boldsymbol{T}}\right)_i\right|^2\delta\left(\omega-\omega_i\right) \tag{3.22}$$

Here, $\widetilde{\boldsymbol{T}}$ is composed of 7^{th} to 3N+6^{th} row and first to 3N+6^{th} column of .

3.3 Anharmonic spinwave calculation

3.3.1 One phonon model

In the following Hamiltonian, we assumed one dispersionless optical phonon mode to form the magnon-phonon hybrid mode:

$$\begin{aligned} H &= J\sum_{ij}\left(S_i^xS_j^x+S_i^yS_j^y+\widetilde{\gamma}S_i^zS_j^z\right)+\hbar\omega_0\sum_k b_{kx(y)}^\dagger b_{kx(y)} \\ &+\widetilde{\alpha}\sum_{ij}\left(\boldsymbol{e}_{O_{ij}i}\cdot\boldsymbol{U}_i+\boldsymbol{e}_{O_{ij}j}\cdot\boldsymbol{U}_j\right)\boldsymbol{S}_i\cdot\boldsymbol{S}_j \end{aligned} \tag{3.23}$$

Here, $e_{O_{ij}i}$ denotes a unit vector parallel or perpendicular to the line connecting i-th Mn atoms and O_{ij} depending on the magnon-phonon coupling mechanism. After the successive application of Holstein-Primakoff transformation and Bogoliubov transformation, the first term in the above equation can be summarized by the following equations:

$$\begin{aligned} &\mathrm{J}\sum_{ij}\left(S_i^xS_j^x+S_i^yS_j^y+\widetilde{\gamma}S_i^zS_j^z\right)=S\sum_k A_ka_k^\dagger a_k-\frac{1}{2}B_k\left(a_k^\dagger a_{-k}^\dagger+a_{-k}a_k\right)= \\ &\sum_k\varepsilon_k\alpha_k^\dagger\alpha_k \end{aligned} \tag{3.24}$$

$$\varepsilon_k=S\sqrt{A_k^2-B_k^2}\,,\quad a_k=u_k\alpha_k+v_k\alpha_{-k}^\dagger\,,\quad u_k^2+v_k^2=\frac{SA_k}{\varepsilon_k},\quad 2u_kv_k=\frac{SB_k}{\varepsilon_k} \tag{3.25}$$

$$A_k=3J\left(\left(\widetilde{\gamma}-\frac{1}{2}\right)f_k+1\right),\qquad B_k=\frac{3J}{2}\left(1+2\widetilde{\gamma}\right)f_k \tag{3.26}$$

$$f_k=\frac{1}{3}\int_i cos\left(\boldsymbol{k}\cdot\boldsymbol{\delta_i}\right) \tag{3.27}$$

$$\boldsymbol{\delta}_1 = (1,0)\,, \quad \boldsymbol{\delta}_2 = \left(-\frac{1}{2}, \frac{\sqrt{3}}{2}\right), \quad \boldsymbol{\delta}_3 = \left(-\frac{1}{2}, -\frac{\sqrt{3}}{2}\right) \tag{3.28}$$

The quadratic part of the Hamiltonian can be written in the following matrix form:

$$H_2^k = Y^\dagger h Y \tag{3.29}$$

$$\mathrm{Y} = \left(\alpha_k \ \beta_k \ \alpha_{-k}^\dagger \ \beta_{-k}^\dagger\right)^T, \qquad h = \frac{1}{2}\begin{pmatrix} F & G \\ G & F \end{pmatrix} \tag{3.30}$$

$$\beta_k = (\chi_{kx} b_{kx} + \chi_{ky} b_{ky})/|\boldsymbol{\chi}_k| \tag{3.31}$$

$$\mathrm{F} = \begin{pmatrix} \varepsilon_k & c_k \\ c_k & \hbar\omega_0 \end{pmatrix}, \quad G = \begin{pmatrix} 0 & c_k \\ c_k & 0 \end{pmatrix} \tag{3.32}$$

Here, the operator β_k represents a linear combination of the two degenerate phonon modes that are coupled to the magnon branch. When the bond length change is important, the coupling factor $\boldsymbol{\chi}_k$ in (3.31) is given by:

$$\boldsymbol{\chi}_k = \boldsymbol{e}_1\left(e^{i\boldsymbol{k}\cdot\boldsymbol{\delta_2}} - e^{-i\boldsymbol{k}\cdot\boldsymbol{\delta_3}}\right) + \boldsymbol{e}_2\left(e^{i\boldsymbol{k}\cdot\boldsymbol{\delta_3}} - e^{-i\boldsymbol{k}\cdot\boldsymbol{\delta_1}}\right) + \boldsymbol{e}_3\left(e^{i\boldsymbol{k}\cdot\boldsymbol{\delta_1}} - e^{-i\boldsymbol{k}\cdot\boldsymbol{\delta_2}}\right) \tag{3.33}$$

$$\boldsymbol{e}_1 = (0,1)\,, \quad \boldsymbol{e}_2 = \left(-\frac{\sqrt{3}}{2}, -\frac{1}{2}\right), \quad \boldsymbol{e}_3 = \left(\frac{\sqrt{3}}{2}, -\frac{1}{2}\right) \tag{3.34}$$

Alternatively, when the bond angles are relevant, the coupling term is also given by eq. (3.29) with $\boldsymbol{\chi}_k = \boldsymbol{\delta}_2\left(e^{i\boldsymbol{k}\cdot\boldsymbol{\delta_1}} + e^{-i\boldsymbol{k}\cdot\boldsymbol{\delta_3}}\right) + \boldsymbol{\delta}_3\left(e^{i\boldsymbol{k}\cdot\boldsymbol{\delta_2}} + e^{-i\boldsymbol{k}\cdot\boldsymbol{\delta_1}}\right) + \boldsymbol{\delta}_1\left(e^{i\boldsymbol{k}\cdot\boldsymbol{\delta_3}} + e^{i\boldsymbol{k}\cdot\boldsymbol{\delta_2}}\right)$.

The magnon-phonon coupling parameter c_k in (3.32) can be written as

$$c_k = \mathrm{g}\cdot\mathrm{JS}\sqrt{\frac{3S}{8}}\,(u_k + v_k)\,|\boldsymbol{\chi}_k| \tag{3.35}$$

where

$$\mathrm{g} = \alpha \cdot \frac{1}{2d}\sqrt{\frac{\hbar}{2m_{Mn}\omega_0}} \tag{3.36}$$

Here, g is the product of the dimensionless exchange-striction strength α and the average zero-point atomic displacement in units of 2d associated with the phonon mode $_0$: $\frac{1}{2d}\sqrt{\frac{\hbar}{2m_{Mn}\omega_0}}$. Now, the Hamiltonian can be transformed to the diagonalized form [**?**] with the energies given by the following equations:

$$E_{0k} = \sqrt{\frac{\varepsilon_k^2 + \hbar^2\omega_0^2 - \sqrt{\left(\varepsilon_k^2 + \hbar^2\omega_0^2\right)^2 - 4\left(\hbar^2\varepsilon_k^2\omega_0^2 - 4\hbar {c_k}^2\varepsilon_k\omega_0\right)}}{2}}$$

$$E_{1k} = \sqrt{\frac{\varepsilon_k^2 + \hbar^2\omega_0^2 + \sqrt{\left(\varepsilon_k^2 + \hbar^2\omega_0^2\right)^2 - 4\left(\hbar^2\varepsilon_k^2\omega_0^2 - 4\hbar {c_k}^2\varepsilon_k\omega_0\right)}}{2}} \tag{3.37}$$

We note that away from the level-crossing region, $\varepsilon_k \approx \hbar\omega_0$, Eq. (3.37) closely describes the original magnon and phonon modes, but near that region they are strongly intermixed.

The additional Bogoliubov transformation that diagonalizes the Hamiltonian by mixing magnons and phonons is

$$a_k = u_{0k}\gamma_{0,k} + u_{1k}\gamma_{1,k} + v_{0k}\gamma_{0,-k}^\dagger + v_{1k}\gamma_{1,-k}^\dagger \tag{3.38}$$

where $\gamma_{0,k}$ are the operators of the new quasiparticles: magneto-phonon modes. Using the smallness of the magnon-phonon coupling parameter c_k in equation (3.35), associated with the smallness of the magnon-phonon coupling g, one can write the parameters of this transformation as:

$$u_{0k} \simeq u_k \Big/ \sqrt{1 + \left(\frac{c_k}{E_{0k} - \hbar\omega_0}\right)^2}$$

$$u_{1k} \simeq \left[\frac{c_k}{(E_{1k} - \varepsilon_k)}u_k - \frac{c_k}{(E_{1k} + \varepsilon_k)}v_k\right] \Big/ \sqrt{1 + \left(\frac{c_k}{E_{1k} - \varepsilon_k}\right)^2}$$

$$v_{0k} \simeq v_k \Big/ \sqrt{1 + \left(\frac{c_k}{E_{0k} - \hbar\omega_0}\right)^2}$$

$$v_{1k} \simeq \left[\frac{c_k}{(E_{1k} - \varepsilon_k)}v_k - \frac{c_k}{(E_{1k} + \varepsilon_k)}u_k\right] \Big/ \sqrt{1 + \left(\frac{c_k}{E_{1k} - \varepsilon_k}\right)^2} \tag{3.39}$$

When the original, unperturbed magnon band is near the phonon branch, $\varepsilon_k \approx \hbar\omega_0$, the energies of the magneto-phonon modes can be written as

$$E_{0k} \simeq \varepsilon_k - \Delta_k$$

$$E_{1k} \simeq \hbar\omega_0 + \Delta_k$$

where the splitting

$$\Delta_k = c_k \tag{3.40}$$

is *linear* in the magnon(spin)-phonon coupling. The physics here is that of the mode mixing and level repulsion. One can, therefore, be able to determine the dimensionless exchange-striction strength α directly from the value of the gap between the modes 0 and 1.

3.3.2 Cubic anharmonicity

The cubic term from the spin Hamiltonian is given by

$$H_3^0 \cong J\sqrt{\frac{S}{2}} \int_{ij} sin\theta_{ij} \left[a_i^\dagger a_i \left(a_j^\dagger + a_j \right) - a_j^\dagger a_j \left(a_i^\dagger + a_i \right) \right]$$

$$= \mathrm{iJ}\sqrt{2S} \int_{ij} \int_{k_{1,2,3}} sin\left(\boldsymbol{Q}\cdot\boldsymbol{\delta_{ij}}\right)\ sin\left(k_3\cdot\delta_{ij}\right) \left(a_{-k_1}^\dagger a_{k_2} a_{k_3} + a_{-k_1}^\dagger a_{k_2} a_{-k_3}^\dagger \right)$$

Here, $\boldsymbol{Q} = (4\pi/3a, 0)$ is the ordering vector associated with the 120° ordering structure.

Note that the cubic term from the magnon phonon coupling is negligible due to small mean fluctuations of atoms as discussed in Section 2.5. Using Eq. (3.38), the symmetrized Hamiltonian becomes

$$H_3 = \int_{kq,\mu\nu\eta} \left[\frac{1}{2!}\Gamma_1^{\mu\nu\eta}\left(q, k-q; k\right)\gamma_{\mu,q}^\dagger \gamma_{\nu,k-q}^\dagger \gamma_{\eta,k} + \frac{1}{3!}\Gamma_2^{\mu\nu\eta}\left(q, -k-q, k\right)\gamma_{\mu,q}^\dagger \gamma_{\nu,-k-q}^\dagger \gamma_{\eta,k}^\dagger \right] \tag{3.41}$$

$$\Gamma_{1,2}^{\mu\nu\eta} = 3iJ\sqrt{\frac{3S}{2}}\widetilde{\Gamma}_{1,2}^{\mu\nu\eta} \tag{3.42}$$

$$\widetilde{\Gamma}_1^{\mu\nu\eta} = \overline{f}_1\left(u_{\mu1}+v_{\mu1}\right)\left(u_{\nu2}u_{\eta3}+v_{\nu2}v_{\eta3}\right) + \overline{f}_2\left(u_{\nu2}+v_{\nu2}\right)\left(u_{\mu1}u_{\eta3}+v_{\mu1}v_{\eta3}\right)$$

$$-\overline{f}_3\left(u_{\eta3}+v_{\eta3}\right)\left(u_{\mu1}v_{\nu2}+v_{\mu1}u_{\nu2}\right)$$

$$\widetilde{\Gamma}_2^{\mu\nu\eta} = \overline{f}_1\left(u_{\mu1}+v_{\mu1}\right)\left(u_{\nu2}v_{\eta3}+v_{\nu2}u_{\eta3}\right) + \overline{f}_2\left(u_{\nu2}+v_{\nu2}\right)\left(u_{\mu1}v_{\eta3}+v_{\mu1}u_{\eta3}\right)$$

$$+\overline{f}_3\left(u_{\eta3}+v_{\eta3}\right)\left(u_{\mu1}v_{\nu2}+v_{\mu1}u_{\nu2}\right)$$

$\overline{f}_i = \frac{1}{3}\int_j sin\left(\boldsymbol{k_i}\cdot\boldsymbol{d_j}\right)$

Here $\mu,\ \nu,\ \eta$ are 0 or 1 indices of the magneto-phonon modes in Eq. (3.38).

The relevant decay channel for the quasiparticle with energy E_{1k} (magneto-phonon mode) should be

$$\Gamma_1^{001}\left(q, k-q; k\right)\gamma_{0,q}^{\dagger}\gamma_{0,k-q}^{\dagger}\gamma_{1,k} \tag{3.43}$$

due to the kinematic condition. To investigate the decay rate of each mode, the decay channels should be specified. Following the same notation for the modes we used for Eq. (3.38), we can neglect the 0→{0,0} decay channel due to a large easy-plane anisotropy close to the critical value of 0.92, below which the decays are completely eliminated [21]. Similarly, 1→{1,1} and 1→{1,0} decays are also forbidden since two quasi-particles states of the decay products should lie at much higher energies. Therefore, 1→{0,0} decay is the only relevant channel and the calculated minimum of two quasi-particles continuum from mode 0 is clearly below mode 1. Then, the decay rate of mode 1 is given by the following equation.

$$\Gamma_{1,k} = \frac{1}{2} Im\left(\int_q \frac{\left|\Gamma_1^{001}\left(q, k-q; k\right)\right|^2}{E_{1,k} - E_{0,q} - E_{0,k-q} + i0}\right) \tag{3.44}$$

3.3.3 Dynamical structure factor

The general spectral properties of branch μ can be obtained from the spectral function

$$A_\mu\left(q,\omega\right) = -\frac{1}{\pi} ImG_\mu\left(q,\omega\right) \tag{3.45}$$

The Green function for branch μ is given by

$$G_\mu^{-1}\left(q,\omega\right) = \omega - E_{\mu q} - \Sigma_\mu\left(q,\omega\right) \tag{3.46}$$

Since we are interested in linewidth broadening due to decays, only the imaginary part of the decay rate is considered. Then, the on-shell self-energy is given by

$$\Sigma_\mu\left(q, \omega = E_{\eta,q}\right) = -i\int_{p,\mu\nu} \frac{\pi}{2} \left|\Gamma_1^{\mu\nu\eta}\left(p, q-p; q\right)\right|^2 \delta\left(E_{\eta,q} - E_{\mu,p} - E_{\nu,q-p}\right) \tag{3.47}$$

The dynamical structure factor can be calculated using the spectral function Eq. (3.45).

$$\mathrm{S}\left(q,\omega\right)=\left(\delta_{\alpha\beta}-\frac{k_{\alpha}k_{\beta}}{k^{2}}\right)S_{\alpha\beta}\left(q,\omega\right) \tag{3.48}$$

Up to the $\mathrm{O}(1/S)$ order, each component of the dynamical structure factor is given by the following equations [78].

$$\begin{aligned}S_{x_0x_0}\left(q,\omega\right)=S_{z_0z_0}\left(q,\omega\right)&=\frac{1}{4}\left(S_{xx}\left(q_{-},\omega\right)+S_{xx}\left(q_{+},\omega\right)+S_{zz}\left(q_{+},\omega\right)\right)\\ S_{y_0y_0}\left(q,\omega\right)&=S_{yy}\left(q,\omega\right)\end{aligned} \tag{3.49}$$

Then, Eq. (3.49) can be rewritten by

$$\mathrm{S}\left(q,\omega\right)=\left(1-\frac{k_{y}^{2}}{k^{2}}\right)S_{y_0y_0}\left(q,\omega\right)+\left(2-\frac{k_{x}^{2}+k_{z}^{2}}{k^{2}}\right)S_{x_0x_0}\left(q,\omega\right) \tag{3.50}$$

$$\begin{aligned}S_{xx}\left(q,\omega\right)&\approx\int_{\mu}\frac{S}{2}(u_{\mu,q}+v_{\nu,q})^{2}A_{11}^{\mu}\left(q,\omega\right)\\ S_{yy}\left(q,\omega\right)&\approx\int_{\mu}\frac{S}{2}(u_{\mu,q}-v_{\nu,q})^{2}A_{11}^{\mu}\left(q,\omega\right)\\ S_{zz}\left(q,\omega\right)&=\frac{1}{2}\int_{p,\mu\nu}\left(u_{\mu,p}v_{\nu,p-q}+v_{\mu,p}u_{\nu,p-q}\right)^{2}\delta\left(\omega-E_{\mu,p}-E_{\nu,p-q}\right)\end{aligned} \tag{3.51}$$

3.3.4 Magnon-phonon coupling in $YMnO_3$ due to DM and single ion anisotropy

The magnon-phonon coupling from exchange-striction has been covered in the previous sections. But it is also possible that other terms in spin Hamiltonian such as DM and single ion anisotropies (SIA) can give rise to magnon-phonon coupling. Indeed, such terms have been pointed to induce the gap opening of c-axis polarized phonon mode [59, 60], yet no calculation results has been reported so far. In this section, I explicitly calculate the Hamiltonian matrix for such case.

1. DM Hamiltonian

$$\mathrm{H}=\sum_{ij}J_{ij}S_{i}\cdot S_{j}+\sum_{ij}D_{ij}\cdot S_{i}\times S_{j}+\sum_{i}S_{i}K_{i}S_{j} \tag{3.52}$$

Previously, I have discussed the symmetric exchange J and easy plane & easy axis type anisotropy K. Here, I will discuss DM vectors lying in the ab plane and off diagonal components of the single ion anisotropy.

DM interactions and single ion anisotropies (SIA) lead to a spin canting along the c-axis whose angle α is given by the following relation.

$$\alpha \simeq \frac{\sqrt{3}D_{xy} + K_{xz}}{18J} \tag{3.53}$$

Since this canting angle is too small to affect the spin dynamics, we will neglect it from now on. Then, the spin operators can be represented by Holstein-Primakoff operators.

$$\begin{aligned}
S^x_{1,4} &= S - a^\dagger_{1,4}a_{1,4} \\
S^y_{1,4} &= \frac{\sqrt{2S}}{2i}\left(a_{1,4} - a^\dagger_{1,4}\right) \\
S^z_{1,4} &= \frac{\sqrt{2S}}{2}\left(a_{1,4} + a^\dagger_{1,4}\right) \\
S^x_{2,5} &= -\frac{1}{2}\left(S - a^\dagger_{2,5}a_{2,5}\right) - \frac{\sqrt{6S}}{4i}\left(a_{2,5} - a^\dagger_{2,5}\right) \\
S^y_{2,5} &= -\frac{\sqrt{2S}}{4i}\left(a_{2,5} - a^\dagger_{2,5}\right) + \frac{\sqrt{3}}{2}\left(S - a^\dagger_{2,5}a_{2,5}\right) \\
S^z_{2,5} &= \frac{\sqrt{2S}}{2}\left(a_{2,5} + a^\dagger_{2,5}\right) \\
S^x_{3,6} &= -\frac{1}{2}\left(S - a^\dagger_{3,6}a_{3,6}\right) + \frac{\sqrt{6S}}{4i}\left(a_{3,6} - a^\dagger_{3,6}\right) \\
S^y_{3,6} &= -\frac{\sqrt{2S}}{4i}\left(a_{3,6} - a^\dagger_{3,6}\right) - \frac{\sqrt{3}}{2}\left(S - a^\dagger_{3,6}a_{3,6}\right) \\
S^z_{3,6} &= \frac{\sqrt{2S}}{2}\left(a_{3,6} + a^\dagger_{3,6}\right)
\end{aligned} \tag{3.54}$$

Then the ab plane component of the cross products are given by:

$$S_{1,4}\times S_{2,5} = \hat{x}\left[-i\frac{S}{4}\left(3a_{1,4}a_{2,5} + a_{1,4}a^\dagger_{2,5} - a^\dagger_{1,4}a_{2,5} - 3a^\dagger_{1,4}a^\dagger_{2,5}\right) - \frac{\sqrt{6S}}{4}S\left(a_{1,4} + a^\dagger_{1,4}\right)\right]$$

$$+\hat{y}\left[i\frac{\sqrt{3}S}{4}\left(a_{1,4}a_{2,5} - a_{1,4}a^\dagger_{2,5} + a^\dagger_{1,4}a_{2,5} - a^\dagger_{1,4}a^\dagger_{2,5}\right) - \frac{\sqrt{2S}}{4}S\left(a_{1,4} + a^\dagger_{1,4} + 2a_{2,5} + 2a^\dagger_{2,5}\right)\right]$$

$$S_{2,5} \times S_{3,6} = \hat{x}\left[-i\frac{S}{2}\left(-a_{2,5}a_{3,6}^{\dagger} + a_{2,5}^{\dagger}a_{3,6}\right) + \frac{\sqrt{6S}}{4}S\left(a_{2,5} + a_{2,5}^{\dagger} + a_{3,6} + a_{3,6}^{\dagger}\right)\right]$$

$$+\hat{y}\left[-i\frac{\sqrt{3}S}{2}\left(a_{2,5}a_{3,6} - a_{2,5}^{\dagger}a_{3,6}^{\dagger}\right) + \frac{\sqrt{2S}}{4}S\left(a_{3,6} + a_{3,6}^{\dagger} - a_{2,5} - a_{2,5}^{\dagger}\right)\right]$$

$$S_{3,6}\times S_{1,4} = \hat{x}\left[-i\frac{S}{4}\left(-3a_{3,6}a_{1,4} + a_{3,6}a_{1,4}^{\dagger} - a_{3,6}^{\dagger}a_{1,4} + 3a_{3,6}^{\dagger}a_{1,4}^{\dagger}\right) - \frac{\sqrt{6S}}{4}S\left(a_{1,4} + a_{1,4}^{\dagger}\right)\right]$$

$$+\hat{y}\left[-i\frac{\sqrt{3}S}{4}\left(-a_{3,6}a_{1,4} - a_{3,6}a_{1,4}^{\dagger} + a_{3,6}^{\dagger}a_{1,4} + a_{3,6}^{\dagger}a_{1,4}^{\dagger}\right) + \frac{\sqrt{2S}}{4}S\left(2a_{3,6} + 2a_{3,6}^{\dagger} + a_{1,4} + a_{1,4}^{\dagger}\right)\right]$$

Here, the quadratic terms contribute to the spinwave dispersion, while the linear terms are responsible for the magnon-phonon coupling. Constants and cubic terms are dropped for convenience. After the Fourier transformation, the DM interaction Hamiltonian is given by the following matrix form.

$$H_{DM} = \sum_{k} X_k^{\dagger} h_k X_k$$

$$h_k = \begin{bmatrix} F_1 & 0 & G_1 & 0 \\ 0 & F_2 & 0 & G_2 \\ -G_1 & 0 & -F_1 & 0 \\ 0 & -G_2 & 0 & -F_2 \end{bmatrix}$$

$$F_1 = \begin{bmatrix} 0 & iA_{12} & iA_{31}^{*} \\ iA_{12}^{*} & 0 & iA_{23} \\ iA_{31} & iA_{23}^{*} & 0 \end{bmatrix} F_2 = \begin{bmatrix} 0 & iA_{45} & iA_{64}^{*} \\ iA_{45}^{*} & 0 & iA_{56} \\ iA_{64} & iA_{56}^{*} & 0 \end{bmatrix}$$

$$G_1 = \begin{bmatrix} 0 & iB_{12} & iB_{31}^{*} \\ iB_{12}^{*} & 0 & iB_{23} \\ iB_{31} & iB_{23}^{*} & 0 \end{bmatrix} G_2 = \begin{bmatrix} 0 & iB_{45} & iB_{64}^{*} \\ iB_{45}^{*} & 0 & iB_{56} \\ iB_{64} & iB_{56}^{*} & 0 \end{bmatrix}$$

$$A_{12} = \frac{S}{8}\left[2D_1 + D_2\left(e^{ik\cdot a} + e^{-ik\cdot b}\right)\right]$$

$$A_{23} = \frac{S}{8}\left[2D_1 e^{-ik\cdot(a+b)} + D_2\left(e^{-ik\cdot a} + 1\right)\right]$$

$$A_{31} = \frac{S}{8}\left[2D_1 e^{ik\cdot(a+b)} + D_2\left(1 + e^{ik\cdot b}\right)\right]$$

i,j	$\hat{z}_{ij}$	$\hat{r}_{ij}$	$\hat{D}_{ij}$	R_{ij}
1,2	-1, +1, +1	e_3, e_2, e_1	-d_3, d_2, d_1	0, a, -b
2,3	-1, +1, +1	e_1, e_3, e_2	-d_1, d_3, d_2	-a-b, -a, 0
3,1	-1, +1, +1	e_2, e_1, e_3	-d_2, d_1, d_3	a+b, 0, b
4,5	-1, +1, +1	-e_3, -e_2, -e_1	d_3, -d_2, -d_1	a-b, -b, a
5,6	-1, +1, +1	-e_1, -e_3, -e_2	d_1, -d_3, -d_2	b, 0, -a
6,4	-1, +1, +1	-e_2, -e_1, -e_3	d_2, -d_1, -d_3	-a, b, 0

Table 3.2: DM vectors and Rij between different neighboring spins.

$$A_{45} = -\frac{S}{8}\left[2D_1 e^{ik\cdot(a-b)} + D_2\left(e^{-ik\cdot b} + e^{ik\cdot a}\right)\right]$$

$$A_{56} = -\frac{S}{8}\left[2D_1 e^{ik\cdot b} + D_2\left(1 + e^{-ik\cdot a}\right)\right]$$

$$A_{64} = -\frac{S}{8}\left[2D_1 e^{-ik\cdot a} + D_2\left(e^{ik\cdot b} + 1\right)\right]$$

$$B_{12} = \frac{S}{8}\left[D_2\left(-3e^{ik\cdot a} + 3e^{-ik\cdot b}\right)\right]$$

$$B_{23} = \frac{S}{8}\left[D_2\left(-3e^{-ik\cdot a} + 3\right)\right]$$

$$B_{31} = \frac{S}{8}\left[D_2\left(-3 + 3e^{ik\cdot b}\right)\right]$$

$$B_{45} = \frac{S}{8}\left[D_2\left(3e^{-ik\cdot b} - 3e^{ik\cdot a}\right)\right]$$

$$B_{56} = \frac{S}{8}\left[D_2\left(3 - 3e^{-ik\cdot a}\right)\right]$$

$$B_{64} = \frac{S}{8}\left[D_2\left(3e^{ik\cdot b} - 3\right)\right]$$

$$X_k = \begin{pmatrix} a_{1k} & \cdots & a_{6k} & a^{\dagger}_{-1k} & \cdots & a^{\dagger}_{-6k} \end{pmatrix}^T \tag{3.55}$$

$$e_1 = (0, -1,\ 0)\,, e_{2=}\left(\frac{\sqrt{3}}{2}, \frac{1}{2}, 0\right), e_3 = \left(-\frac{\sqrt{3}}{2}, \frac{1}{2}, 0\right)$$

$$d_1 = (1, 0, 0)\,, d_2 = \left(-\frac{1}{2}, \frac{\sqrt{3}}{2}, 0\right), d_3 = (-\frac{1}{2}, -\frac{\sqrt{3}}{2}, 0)$$

1. Magnon-phonon coupling Hamiltonian

Oxygen trimerization distortion below the FE transition leads to the DM interaction and off diagonal component of SIA. Therefore, the coupling Hamiltonian is given by

$$H_{coup} = \int_{ij} \alpha_{ij} \hat{z}_{O_{ij}} \cdot u_{O_{ij}} \left(\hat{z}_{O_{ij}} \times \hat{r}_{ij} \right) \cdot S_i \times S_j + \beta_{ij} \hat{z}_{O_{ij}} \cdot u_{O_{ij}} \left(S_i^n S_i^z + S_i^z S_i^n \right) \tag{3.56}$$

Here, u_{ij} is the displacement vector of oxygen atom connecting i-th and j-th Manganese atom, and the linear term in SIA and Oxygen z displacements are given by

$$S_i^n S_i^z = \left(S - a_i^\dagger a_i \right) \frac{\sqrt{2S}}{2} \left(a_i + a_i^\dagger \right) \simeq \frac{S\sqrt{2S}}{2} \left(a_i + a_i^\dagger \right) \tag{3.57}$$

$$u_{O_{ij}}^z = \sqrt{\frac{\hbar}{2m\omega_k}} \int_k W_{O_{ij},k}^z e^{ik \cdot R_{O_{ij}}} \left(b_k + b_{-k}^\dagger \right) \tag{3.58}$$

Then, the coupling Hamiltonian can be written by the following matrix form.

$$H_{coup} = \int_k Y_k^\dagger h_k Y_k$$

$$Y_k = \begin{pmatrix} a_{1k} & \cdots & a_{6k} & b_k & a_{-1k}^\dagger & \cdots & a_{-6k}^\dagger & b_{-k}^\dagger \end{pmatrix}^T$$

$$h_k = \begin{bmatrix} 0 & N^\dagger & 0 & N^\dagger \\ N & 0 & N & 0 \\ 0 & N^\dagger & 0 & N^\dagger \\ N & 0 & N & 0 \end{bmatrix}$$

$$\mathrm{N} = \begin{pmatrix} N_1 & \cdots & N_6 \end{pmatrix}$$

W??conj(W)

$$N_1 = S\sqrt{\frac{S\hbar}{m\omega_k}} \left[\left(-\frac{\sqrt{3}}{2}\alpha_1 - \frac{\beta_1}{2} \right) W_{O_1,k}^z + \left(-\frac{\sqrt{3}}{4}\alpha_2 + \frac{\beta_2}{2} \right) \left(W_{O_3,k}^z + W_{O_2,k}^z e^{ik \cdot b} \right) \right]$$

$$N_2 = S\sqrt{\frac{S\hbar}{m\omega_k}} \left[\left(-\frac{\sqrt{3}}{2}\alpha_1 - \frac{\beta_1}{2} \right) W_{O_1,k}^z + \left(-\frac{\sqrt{3}}{4}\alpha_2 + \frac{\beta_2}{2} \right) \left(W_{O_3,k}^z e^{ik \cdot a} + W_{O_2,k}^z \right) \right]$$

$$N_3 = S\sqrt{\frac{S\hbar}{m\omega_k}} \left[\left(-\frac{\sqrt{3}}{2}\alpha_1 - \frac{\beta_1}{2} \right) W_{O_1,k}^z e^{-ik \cdot (a+b)} + \left(-\frac{\sqrt{3}}{4}\alpha_2 + \frac{\beta_2}{2} \right) \left(W_{O_3,k}^z + W_{O_2,k}^z \right) \right]$$

O_{ij},i	$\hat{z}_{ij}$	$\hat{r}_{ij}$	$\hat{D}_{ij}$	$R_{ij,i}$	O_{ij}
12,1	-1, +1, +1	e_3, e_2, e_1	-d_3, d_2, d_1	0, 0, b	1, 3, 2
12,2	-1, +1, +1	e_3, e_2, e_1	-d_3, d_2, d_1	0, a, 0	1, 3, 2
23,2	-1, +1, +1	e_1, e_3, e_2	-d_1, d_2, d_3	0, a, 0	1, 3, 2
23,3	-1, +1, +1	e_1, e_3, e_2	-d_1, d_2, d_3	-a-b, 0, 0	1, 3, 2
31,3	-1, +1, +1	e_2, e_1, e_3	-d_2, d_1, d_3	-a-b, 0, 0	1 ,3, 2
31,1	-1, +1, +1	e_2, e_1, e_3	-d_2, d_1, d_3	0, 0, b	1, 3, 2
45,4	-1, +1, +1	-e_3, -e_2, -e_1	d_3, -d_2, -d_1	-a, b, 0	4, 5, 6
45,5	-1, +1, +1	-e_3, -e_2, -e_1	d_3, -d_2, -d_1	-b, 0, a	4, 5, 6
56,5	-1, +1, +1	-e_1, -e_3, -e_2	d_1, -d_2, -d_3	-b, 0, a	4, 5, 6
56,6	-1, +1, +1	-e_1, -e_3, -e_2	d_1, -d_2, -d_3	0, 0, 0	4, 5, 6
64,6	-1, +1, +1	-e_2, -e_1, -e_3	d_2, -d_1, -d_3	0, 0, 0	4, 5, 6
64,4	-1, +1, +1	-e_2, -e_1, -e_3	d_2, -d_1, -d_3	-a, b, 0	4, 5, 6

Table 3.3: DM vector, Rij and corresponding oxygen atoms between different neighboring spins.

$$N_4 = S\sqrt{\frac{S\hbar}{m\omega_k}}\left[\left(\frac{\sqrt{3}}{2}\alpha_1 + \frac{\beta_1}{2}\right)W^z_{O_4,k}e^{-ik\cdot a} + \left(\frac{\sqrt{3}}{4}\alpha_2 - \frac{\beta_2}{2}\right)\left(W^z_{O_5,k}e^{ik\cdot b} + W^z_{O_6,k}\right)\right]$$

$$N_5 = S\sqrt{\frac{S\hbar}{m\omega_k}}\left[\left(\frac{\sqrt{3}}{2}\alpha_1 + \frac{\beta_1}{2}\right)W^z_{O_4,k}e^{-ik\cdot b} + \left(\frac{\sqrt{3}}{4}\alpha_2 - \frac{\beta_2}{2}\right)\left(W^z_{O_5,k} + W^z_{O_6,k}e^{ik\cdot a}\right)\right]$$

$$N_6 = S\sqrt{\frac{S\hbar}{m\omega_k}}\left[\left(\frac{\sqrt{3}}{2}\alpha_1 + \frac{\beta_1}{2}\right)W^z_{O_4,k} + \left(\frac{\sqrt{3}}{4}\alpha_2 - \frac{\beta_2}{2}\right)\left(W^z_{O_5,k} + W^z_{O_6,k}\right)\right] \tag{3.59}$$

Here, $\sqrt{\frac{S\hbar}{m\omega_k}} = \frac{0.7202}{\sqrt{E_k}}$ Å

4. Magnon and phonon spectra of $RMnO_3$

4.1 Magnetic excitation spectra

4.1.1 Determination of spin Hamiltonian

The magnetic excitation spectra of $RMnO_3$ measured from inelastic neutron scattering experiments described in the chapter 2 can be compared with the theoretical spectra discussed in the chapter 3. The dominant magnetic interaction which determines the 120° spin structure is the nearest neighbor super exchange interaction in the triangular Mn-O layer. The spin Hamiltonian including only such interactions is given by:

$$\mathcal{H} = J_1 \sum_{\mathbf{intra}} \mathbf{S}_i \cdot \mathbf{S}_j + J_2 \sum_{\mathbf{inter}} \mathbf{S}_i \cdot \mathbf{S}_j \tag{4.1}$$

$$\tag{4.2}$$

The two different exchange parameters J_1 and J_2 are due to the Mn trimerization as shown in figure 1.4. The two different values of exchange interaction are most apparent in the high energy part of magnon dispersion along the (H,1-2H,0) direction, as shown in the figure 4.1. If J_1 unequals to J_2, a triply degenerate mode at K point is lifted, resulting in one doubly degenerate mode at high energy and the other at lower energy. When $J_2 > J_1$, the high energy mode along the M-K direction is almost degenerate, while the three different modes are evident for $J_1 > J_2$. The measured spinwave of $LuMnO_3$ shows clear three peaks at the Λ point as shown in figure 4.1 (c), which matches the $J_1 > J_2$ case. It is consistent with powder neutron diffraction results reporting Mn x position is smaller than 1/3 at low temperatures [38, 45].

Although the dominant in-plane super exchange interactions describe the high energy magnon spectra quite well, the inter-layer super exchange interaction and the single ion anisotropy are necessary to explain the various possible magnetic structures. The inter-layer interaction determines the angle between the spins in alternating triangular layers, while the single ion anisotropies fix the directions of the spins [70]. The full spin Hamiltonian includes four different exchange parameters (J_1-J_2-J_1^c-J_2^c), easy plane anisotropy (D_1) and easy axis anisotropy (D_2) as

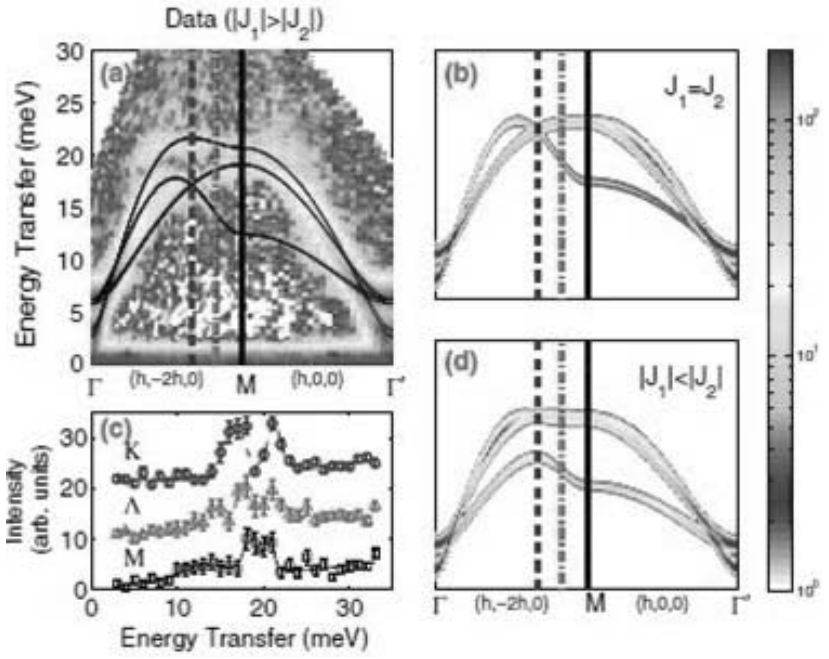

Figure 4.1: Data (a) and linear spin wave theory calculated neutron structure factors convoluted with a 0.8 meV Gaussian (b),(d). (c) Cuts along the vertical lines in the dispersion curves at the M, ($\frac{1}{2}$ 0 0), (square and solid line) and K, ($\frac{1}{3}$ $\frac{1}{3}$ 0), (circle and dashed line) wave vectors and in between, Λ.

shown by equation 3.2. The inter layer interactions and the easy axis anisotropy are more than 100 times smaller than the dominant in-plane exchange interactions [68, 69], as evidenced by a small dispersion along the c* direction and a small spin gap shown by the right most part of figure 4.2. The dispersion was calculated using standard methods with the best fit to the measured inelastic neutron spectra obtained by a minimal set of parameters: $J_1 = 9$ meV, $J_2 = 1.4$ meV, $J_1^c - J_2^c = 0.018$ meV, $D_1 = 0.28$ meV and $D_2 = 0.006$ meV. Except for some discrepancies indicated by red box to be discussed later, the key features of the measured spin waves are well captured by this model. Note that $J_1 > J_2$ contrasts with the previously reported TAS spin wave measurements which suggested the opposite case [69]. In particular, the authors reported only two peaks at the M point (1/2 0 0), which is only consistent with the case of $J_1 < J_2$. Our data show three modes at M and a mode crossing at K which can only be explained by $J_1 > J_2$. The large ratio $J_1/J_2 \sim 6.4$, albeit within the stability limit of the long-range 120° structure, unlike in $LiVO_2$, is unexpected. Indeed, a first-principle calcuation using the coordinates reported by Lee [38] yielded $\frac{J_1}{J_2} \sim 1.1$ for $LuMnO_3$, which is quite different from $\frac{J_1}{J_2}$ value determined from our inelastic neutron scattering experiments. In terms of the spinwave dispersion, it is required by the large gap between two upper spin wave modes, which is degenerate when $J_1 = J_2$ and $J_1 < J_2$.

4.1.2 Discrepancies between the calculated and measured spectra

Although the key features of the magnon spectra are captured by the Hamiltonian presented in the previous section, a closer inspection of the experimental spin wave dispersion curve reveals some interesting discrepancies, which cannot be explained by the linear spinwave calculations. The most notable discrepancy is seen near (1/2 1/2 0)(labelled B in the single sublattice triangular Brillouin zone), where the experimental dispersion curve not only deviates from the theoretical results but also shows a minimum. This minimum occurs exactly at the same point where nonlinear spin wave theory predicts a roton-like minimum [18, 19]. Another feature that is predicted by nonlinear spin wave theory is the magnon linewidth broadening. In fact, the experimental results show such linewidth broadenings near B and D point, as shown in the top panel of figure 4.2 by the larger full width at half maximum (FWHM) of the fitted peaks from energy cuts to the

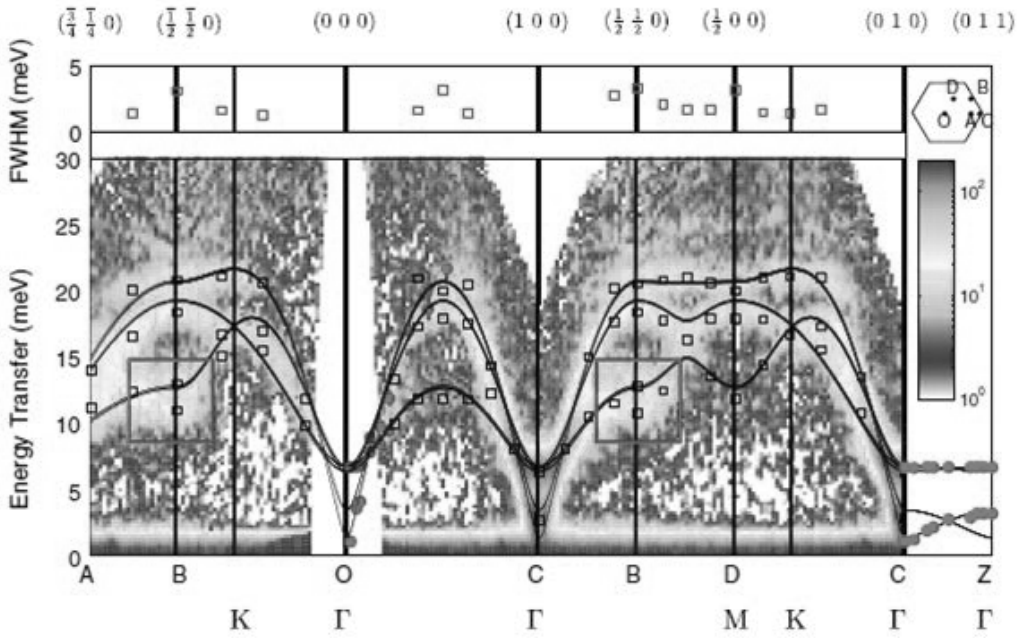

Figure 4.2: Inelastic neutron scattering data along high symmetric directions: fitted peak positions from TAS data (filled circle), ToF data (open square and the contour map), and the fitted dispersion (solid curves) calculated by linear spin wave theory. The first Brillouin zone labels for the hexagonal unit cell (bottom text line) and triangular unit cell (line above) are also shown, together with a sketch of the triangular Brillouin zone (top right corner). The top panel shows the fitted FWHM of the 20 meV peaks from the ToF data, indicating broad peaks, possibly due to magnon decay, only near $(\frac{1}{2}\ \frac{1}{2}\ 0)$ and $(\frac{1}{2}\ 0\ 0)$.

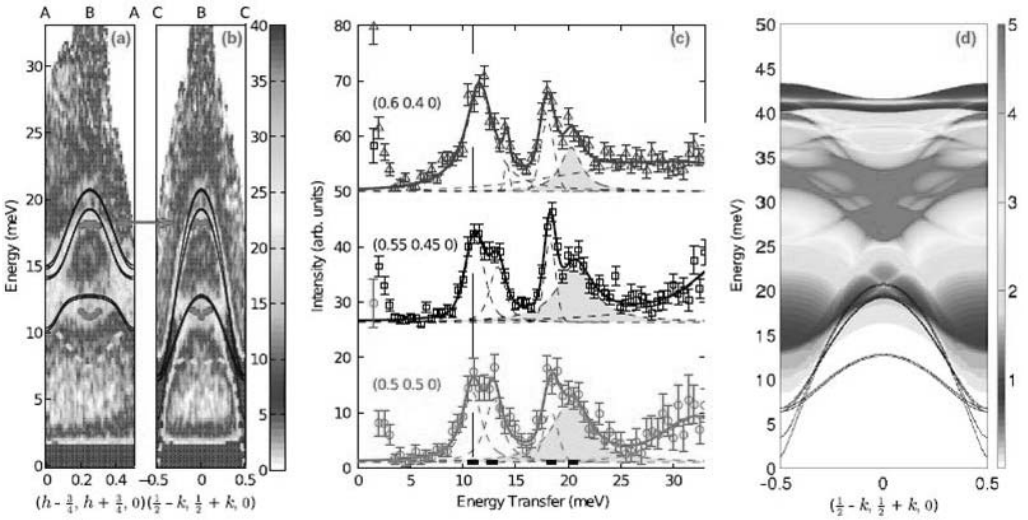

Figure 4.3: Cuts near the roton-like minimum showing the three signatures of magnon decay. (a),(b) The minimum in the dispersion of the lowest energy mode at $(\frac{1}{2}\ \frac{1}{2}\ 0)$, the flat dispersion of the higher energy mode at the same point, indicated by the arrows in (a) and (b), and the anomalously broad width of the $\approx$ 20 meV mode in the cuts in (c). In (a) and (b), points (filled circle) indicate the fitted peak positions from energy cuts through the data. In (c), solid lines at the bottom directly below the peak centers indicate the instrumental resolution width. Thin dashed lines indicate individual fitted Voigt peaks, while the solid line is their sum, and points are measured data. The very broad peak at $\approx$ 32 meV in (c) is attributed to two-magnon scattering. (d) The two-magnon density of states calculated using linear spin wave theory from the single-magnon dispersion (solid lines).

data. Figure 4.3 (c) shows such cuts around B point where the highest energy mode is several times broader than the instrumental resolution while the other points have FWHM similar to the instrument resolution. The signal at higher energy transfer is likely to be caused by two-magnon scattering. Furthermore, this observation of magnon decay is consistent with the calculated two-magnon density of states in figure 4.3 (d), which show that the top of the single-magnon dispersion coincides with a line of strong two-magnon densities of states permitting many decay channels. The calculation of such linewidth, however, is difficult due to the large spatial anisotropy of exchange interaction, which reduces the symmetry of ideal triangular lattice.

Although I have interpreted the result with J_1-J_2 model with magnon decay,

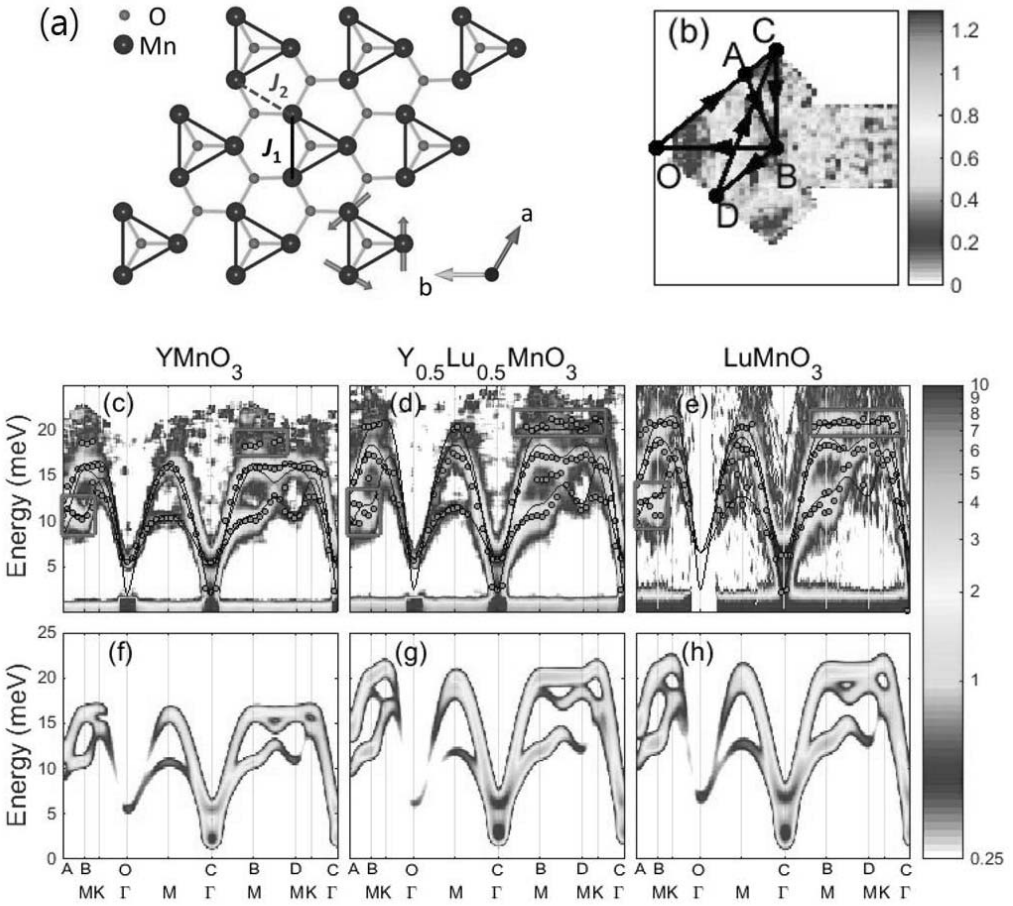

Figure 4.4: (a) A Mn-O layer in $RMnO_3$ forming a distorted 2D triangular antiferromagnet. (b) Inelastic neutron scattering data on $LuMnO_3$ summed over an energy window of [19.5, 20.5]meV. The arrows in b indicate the reciprocal points where the data shown in c–e are cut. (c–e) The inelastic neutron-scattering data along the high symmetric directions (red circle and contour map) and fitted dispersion (black solid curve) for (c) $YMnO_3$, (d) $Y_{0.5}Lu_{0.5}MnO_3$ and (e) $LuMnO_3$ calculated by linear spin wave theory. (f–h) Calculated dynamical spin structure factors using the minimal spin Hamiltonian, equation 3.2 for (f) $YMnO_3$, (g) $Y_{0.5}Lu_{0.5}MnO_3$ and (h) $LuMnO_3$. For the simulations, I used the momentum and energy resolution of the instrument at the elastic line.

the difficulties in nonlinear spinwave calculation and large J_1/J_2 ratio inconsistent with DFT calculation are the two problems to be resolved. One possible approach is to observe the tendency of $\frac{J_1}{J_2}$ ratio and the linewidth in $RMnO_3$ with different rare-earth ions and check if our interpretation is still valid. Therefore I performed similar ToF inelastic neutron scattering experiments on $YMnO_3$ and $Y_{0.5}Lu_{0.5}MnO_3$ single crystals at MAPS, ISIS. Fig. 4.4 shows the spin waves measured at the MAPS beamline of the ISIS facility together with the theoretical dispersion relation calculated from the spin Hamiltonian by a linear spin wave theory using the following parameters: for $YMnO_3$, J_1=4, J_2=1.8, D_1=0.28, D_2=-0.02 meV: for $Y_{0.5}Lu_{0.5}MnO_3$, J_1=12.5, J_2=0.97, D_1=0.18, D_2=-0.018 meV: for $LuMnO_3$, J_1=9, J_2=1.4, D_1=0.28, D_2=-0.02 meV. Despite the apparent success of the linear spin wave calculations, there lies a critical failure too: first, the downward curvature along the AB direction and second, the additional peaks at about 19 meV indicated by a red box in figure 4.4c. But most importantly, here I have to use an unphysically large J_1/J_2 ratio in order to explain the additional high-energy peaks. Apart from the large J_1/J_2 ratio, this analysis of the linear spin waves has another drawback: which is that the calculated dynamical structure factor using the linear spin wave theory as shown in Figs. 4.4g & h always produces stronger intensity at the top mode of the spin waves than at the middle one, in marked contrast with the experimental data.

This discrepancy requires us to consider additional effects and go beyond the standard linear spin wave theory. An additional perturbation next to simple Heisenberg interaction is a spin-lattice coupling, a modulation of exchange due to atomic displacement. Such exchange striction type coupling have been proposed by previous IR and Raman measurements [50, 79], which reported the abrupt energy changes of manganese d-d trnasion and a phonon mode corresponding to in-plane Mn-O vibration motion at T_N. Many other experiments including ultrasound measurements [43], neutron diffraction [38] and dielectric constant measurements [80] also show the importance of magnon and inplane phonon coupling. This conclusion is also backed up by theoretical calculations [81].

4.1.3 Magneto-elastic excitation

Following this idea of a spin-lattice coupling in $RMnO_3$, I construct the following full model Hamiltonian, which couples the in-plane manganese vibrations directly

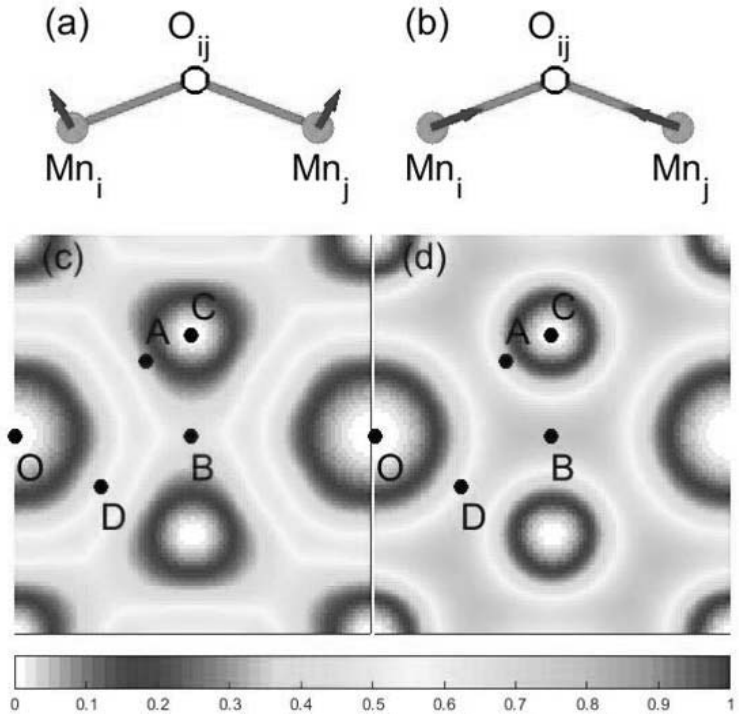

Figure 4.5: It depicts the manganese displacement for the two cases, where there are variations in (a) a bond angle and (b) a bond length, respectively. The q-dependent dynamical structure factor of the high energy magnetoelastic mode calculated using Eq. 3.23 is given for the case of the structural modulation in (c) a bond angle change and (d) a bond length change. Note that our calculated dynamical structure factor for a scenario of bond-angle modulation (a & c) fails to reproduce the experimental momentum dependence shown in Fig. 1(b) as compared with those for a scenario of bond-length modulation (b & d).

to the spin system:

$$H{=}H_{\text{spin}} + \hbar \int_{i=1}^{90} \omega_i b_k^\dagger b_k + \ \widetilde{\alpha} \int_{ij} \left(\mathbf{e}_{\mathrm{O}_{ij}i} \cdot \mathbf{u}_{\mathrm{i}} + \mathbf{e}_{\mathrm{O}_{ij}j} \cdot \mathbf{u}_j \right) \mathbf{S}_i \cdot \mathbf{S}_j(1),$$

where $\mathbf{e}_{\mathrm{O}_{ij}i}$ denotes the unit vector connecting the i-th manganese atom and the neighbouring oxygen atoms between the i-th and j-th manganese atoms as shown in figure 4.5, $\widetilde{\alpha}$ is the exchange striction, $\widetilde{\alpha} = \partial J/\partial r$, which is naturally made into a dimensionless exchange-striction constant $\alpha = \widetilde{\alpha} \cdot 2d/J$ [82], and d is the Mn-O bond length at the equilibrium. Therefore, our Hamiltonian takes into account the modulations of the Mn-O bond length as a function of Mn displacements.

Before going into detailed discussion, I would like to make a general remark on the related issue. In cases when the spin rotational symmetry is broken completely in the ground state, i.e., when the spin structure is non-collinear, the Heisenberg term of the Hamiltonian provides a coupling of the transverse and longitudinal modes on neighboring sites. That is, in terms of the local site-dependent preferred spin direction of the ordered state, the coupling terms take the form of the type $S_i^z S_j^x$, etc. In the magnon language, they are quantized into the "odd" terms, producing linear $(a + a^\dagger)$ and cubic ($a^\dagger aa$, etc.) contributions. In equilibrium, the linear magnon term must vanish, leaving the anharmonic cubic magnon coupling to be the sole outcome, which is important for magnon decays. However, in the presence of coupling to phonons, the linear $(a + a^\dagger)$ terms is "activated", as the local atomic displacements (u_i) violate the equilibrium conditions locally, hence the "direct" coupling of magnons and phonons.

To calculate the full dispersions of all 90 phonon modes for the unit cell with six formula units, we used a first-principles density functional theory (DFT). We show the full phonon dispersion curves for the three compounds as dashed lines in Fig. 4.6. We then calculated the dynamical spin structure factor within the linear approximation by using the full Hamiltonian above with the explicit magnon-phonon coupling: I used the dimensionless exchange-striction coefficients of $\alpha{\sim}$16-20.

The exchange-striction constant can also be estimated by using the pressure-dependence of the crystal structure and the antiferromagnetic transition reported for $YMnO_3$ [83, 84]. From the experimental results, I came to an estimate of the dimensionless exchange striction α of 14 with the following formula: $\alpha{=}\frac{d(P_0)\partial T_{\mathrm{N}}(P)/\partial P}{T_{\mathrm{N}}(P_0)(\partial d(P)/\partial P)}$. Here, d is average Mn-O bond length, which is approximately

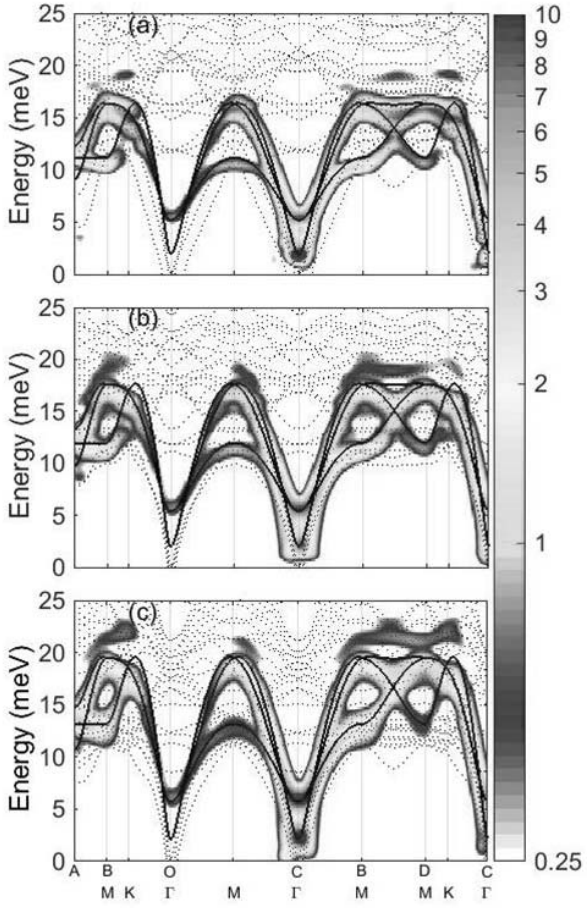

Figure 4.6: The dynamical spin structure factor calculated from the full Hamiltonian, equation 3.10 (contour map) by taking into account the magnon–phonon coupling: the phonon dispersion curves (dashed lines) and the magnon dispersion without the coupling (solid lines) for (a) $YMnO_3$, (b) $Y_{0.5}Lu_{0.5}MnO_3$ and (c) $LuMnO_3$.

one third of lattice constant a. The experimental parameters used in our estimate are $\frac{\partial T_N(P)}{\partial P} = 3$ K GPa^{-1} [83] and $\frac{\partial d(P)}{\partial P} = 0.0057$ Å GPa^{-1} [84]. Below I point out that our own data for the magnon excitation spectrum imply the value of the magneto-striction of the same order. This should be contrasted with the cuprates family, where estimates for an equivalent quantity are substantially smaller, α∼2-7 [85, 86].

By comparing with the experimental data, we obtained the best fitting results with the following sets of the parameters: J_1=J_2=2.5 meV, D_1=0.28 meV, D_2=-0.02 meV and α=16 for $YMnO_3$; J_1=J_2=2.7 meV, D_1=0.28 meV, D_2=-0.02 meV and α=20 for $Y_{0.5}Lu_{0.5}MnO_3$; J_1=J_2=3 meV, D_1=0.28 meV, D_2=-0.02 meV and α=16 for $LuMnO_3$. We note that according to the DFT calculations [86] the relative difference between J_1 and J_2 is theoretically about 10 – 20% at maximum. Therefore, we judge that this choice of J_1=J_2 in our analysis is good enough to capture the essential underlying physics of (Y,Lu)MnO_3, which is the magnon-phonon coupling.

The results shown as colur contour plot in Fig. 4.6 reproduce the overall features of the observed spectra of the experimental data in Fig. 4.4. It clearly shows that the high-energy signals located at $18 \sim 20$ meV come from a direct coupling between the magnon and the optical phonons, i.e. a magneto-elastic mode. This conclusion on the relevance of the magnon-phonon coupling for $RMnO_3$ is also supported by the fact that our calculated spinwaves successfully explains the downward curvature of the bottom magnon branch along the AB direction. In fact, an estimate of the exchange striction from the splitting of the high-energy hybrid modes in Fig. 4.6 yields the values in the same range, α∼10-20, according to equation 3.40. Note that our polarized neutron scattering data are also in good agreement with our calculation. The spin phonon model explains the peak splitting of the bottom mode at B point as well as the polarization of the mode as shown by figure 4.7.

4.1.4 Decay of the hybrid mode

In addition to the magnon-phonon hybridization, noncollinear spin structures allow three magnon interactions as discussed above, which can lead to spontaneous magnon decay into two magnon states when the kinematic conditions are satisfied. The magneto-elastic excitations have, by definition, both magnon and phonon characters. Therefore, the above mechanism can also lead to the decay of magneto-

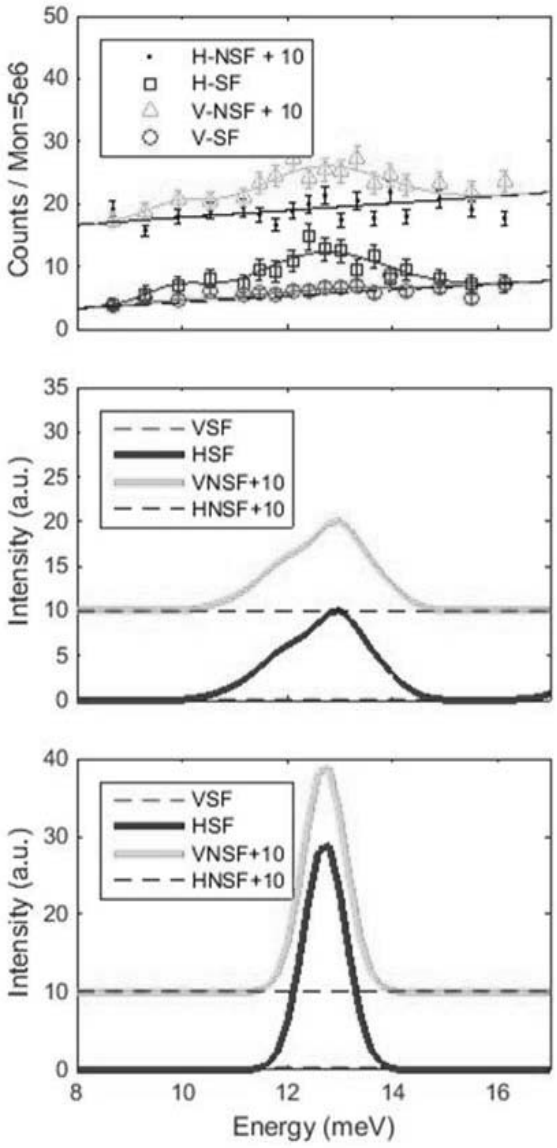

Figure 4.7: (a) The measured spectra are shown for the following four cases: for the vertical field non-spin flip channel (green), the horizontal field non-spin flip channel (black), the horizontal field spin flip channel (blue) and the vertical field spin flip channel (red). The error bars are the standard deviation of each data points experimentally measured. (b) The calculated spectra with the magnon phonon coupling using the first principle phonon result. (c) The calculated spectra without the magnon phonon coupling.

elastic excitations inside the two quasi-particles continuum of magnon. Indeed, I observe significant broadening of the top mode in $LuMnO_3$ near the B and D points as shown in Fig. 4.8 and Fig. 4.9: less strong broadening has been seen for other two compounds.

In order to calculate the decay rate directly and compare it with the experimental data, I simplify the problem by assuming a dispersionless optical phonon mode located at about 20 meV, where the strongest coupling has been observed in our data. Then our model Hamiltonian reads as follows:

$$H{=}J\int_{ij}\left(S_i^xS_j^x+S_i^yS_j^y+\gamma S_i^zS_j^z\right)+\hbar\omega_0\int_k b_k^\dagger b_k+\widetilde{\alpha}\int_{ij}\left(\mathbf{e}_{\mathrm{O}_{ij}i}\cdot\mathbf{u}_i+\boldsymbol{e}_{\mathrm{O}_{ij}j}\cdot\mathbf{u}_j\right)\mathbf{S}_i\cdot\mathbf{S}_j$$

(3.53).

First, I calculate the dynamical spin structure factor by using a standard method. As shown in Fig. 4.8(a) and Fig. 4.5, despite the simplification, the calculation results reproduce well the experimental intensity along the C-B-D direction. For the calculations, I used the following set of the parameters: for $YMnO_3$ J=2.7 meV, γ=0.93, $\hbar\omega_0$=17.5 meV, $\tilde{\alpha}$=7.2; for $LuMnO_3$ J=3.2 meV, γ=0.93, $\hbar\omega_0$=19.5 meV, $\tilde{\alpha}$=8. Then the decay rate of the high-energy mode was calculated using an anharmonic spin wave theory within the 1/S approximation. The calculated results summarized in Fig. 4.8 also show the significant linewidth broadening for the top mode near the B and D points only for $LuMnO_3$, consistent with the experimental results.

The reason for this is that in $LuMnO_3$, the combination of the higher energies of the magnon and magnetoelastic modes means that more decay channels, including two quasiparticle emission, are kinematically allowed. The different decay channels have different boundaries in the reciprocal space which also corresponds to logarithmic singularities in the decay rate [21], and the largest broadening is observed at momentum transfers where the single-quasiparticle dispersion crosses these boundaries, such as at the B point. In the case of $YMnO_3$, no such crossing occurs, so there are fewer decay channels available explaining why the observed linewidths remain narrow. Here I should stress that the single-magnon branches do not cross the line of singularities, whereas the magnetoelastic mode does, so a pure magnon decay is forbidden in this case. Similarly, the intrinsic decay rate of phonons is usually small due to a weak cubic anharmonicity. Thus the strong hybridization of magnons and phonons provides a new mechanism to enhancing

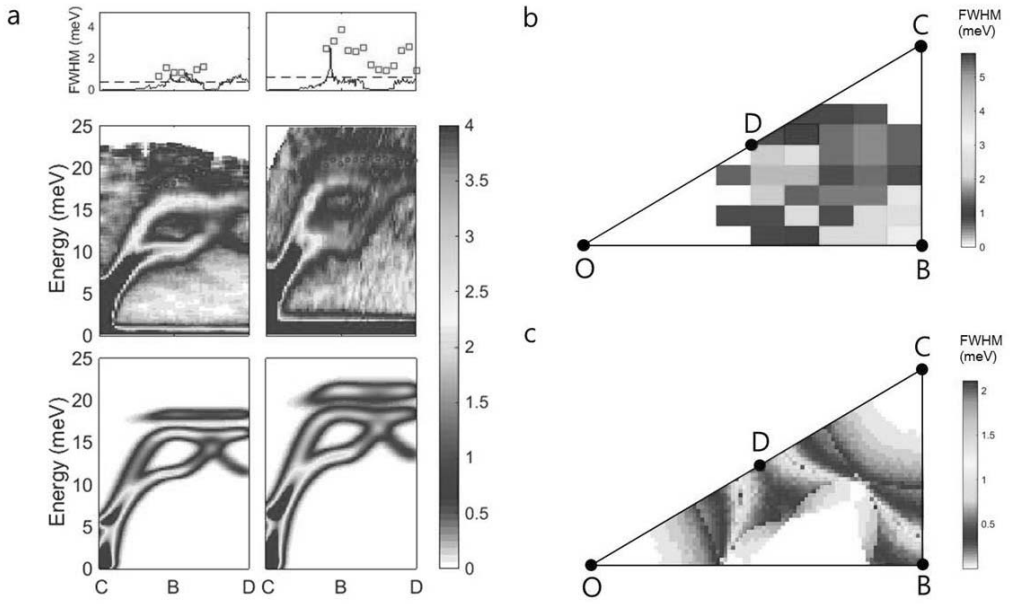

Figure 4.8: (a) The neutron-scattering data along the CBD direction (middle) and the calculated dynamical structure factor within the linear spin wave theory (bottom). Observed linewidth broadening of the top mode (square) together with the calculated result from the 1/S approximation (line) and the experimental resolution (dashed line) (top) for $YMnO_3$ (left) and $LuMnO_3$ (right). (b) Observed linewidth of the top mode for $LuMnO_3$ (contour map) and (c) calculated intrinsic broadening of the top mode using the model Hamiltonian, equation 3.53. The experimental linewidth of the top mode was estimated by using multi-Gaussian functions and the typical results are shown in figure 4.9

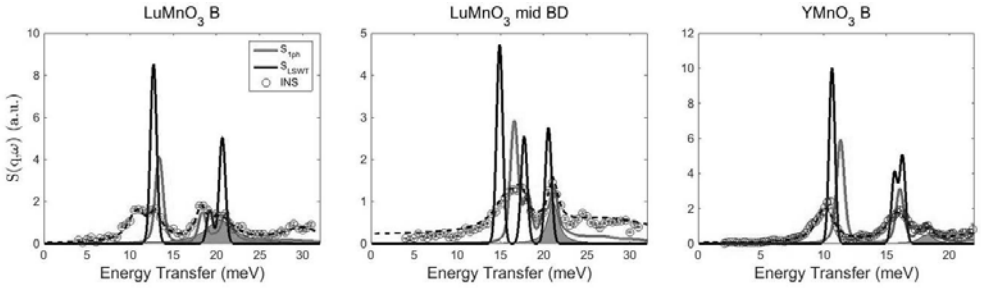

Figure 4.9: Constant q-cuts (circle) along the BD direction compared to the two theoretical cases: one is the 1/S expansion results for one phonon model using Eq. 3.53 (red line) and the other is LSWT without magnon phonon coupling calculated using Eq. 3.2 (black line) for (a,b) $LuMnO_3$ and (c) $YMnO_3$. The dashed line shows the fitting results using multi Gaussian functions, and the shaded area indicates the linewidth broadening of the magneto-elastic mode. Broad signals at high energy are attributed to two magnon continuum.

the magnon decays.

4.2 Phonon spectra

The signature of magnon phonon coupling on the magnetic excitation is covered in section 4.1. But this can only be confirmed by observing the same effect on the phonon spectra.

4.2.1 Magnon phonon coupling due to exchange strction

The phonon density of states obtained by powder inelastic neutron scattering experiments on $YMnO_3$ and $LuMnO_3$ performed on AMATERAS at J-PARC are shown by figure 4.10. Since the magnetic form factor decreses rapidly as a function of momentum transfer, the phonon signal has been taken at relatively large momentum transfers of Q=5-6 $^{-1}$ and summed over Q. Then the phonon density of states are obtained by DFT phonon calculation described in chapter 3. The calculated phonon DOS well captures the peak position of the measured spectra, justifying the analysis in section 4.1 based on the DFT phonon results. Note that the stronger intensity of magneto-elastic excitation for the lutetium richer compounds can also be understood as larger manganese phonon PDOS at the energies of the hybrid mode.

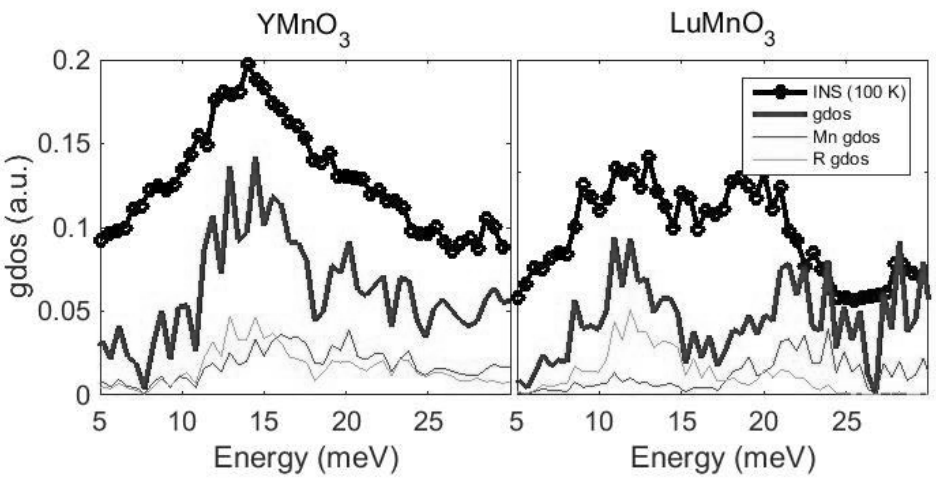

Figure 4.10: It compares the measured experimental phonon DOS with the theoretical results: the inelastic neutron scattering data taken at 100 K (black), the calculated gDOS (blue), manganese gDOS (red) and rare-earth elements gDOS (green).

The IXS experiment was performed on BL43XU at Spring8 with energy resolution of 1.5 meV at FWHM. In order to investigate the in-plane phonon modes coupled to magnon modes, I measured phonon spectra near q = (4 0.5 0). The result shown by Fig. 4.11 demonstrates the spectral weight transfer from the 18 meV optical phonon to a magnon mode at 15 meV below T_N. This directly evidences the coupling of 15 meV magnon mode and 18 meV phonon mode, and support our explanation that the the additional peak at 18 meV measured by inelastic neutron scattering is caused by the magnetic character of such phonon mode. Furthermore, the phonon spectra above and below T_N qualitatively agree with the calculation with and without spin lattice coupling, supporting our exchangestriction model 3.10.

4.2.2 Spin lattice coupling due to DM and SIA

Previous studies also reported an out of plane phonon mode couples to a magnon mode, which is claimed to be caused by DM and single ion anisotropy(SIA) [59, 60]. In order to reexamine such coupling with better q resolution, I performed IXS measurements along the same direction as explored by previous INS mea-

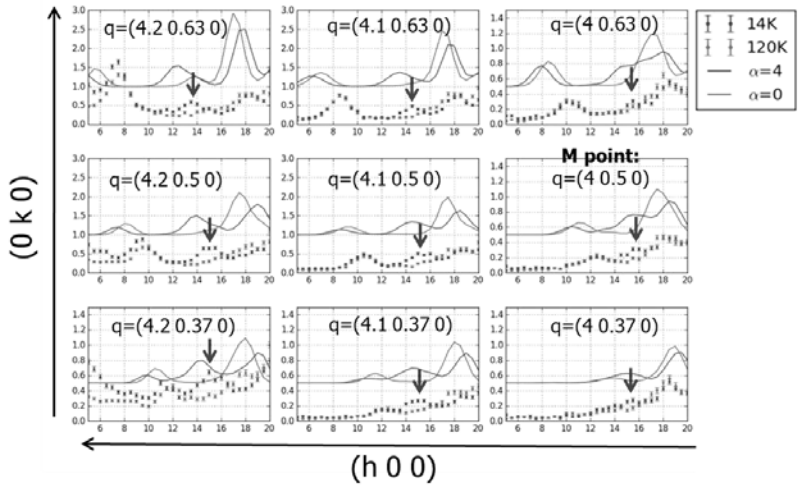

Figure 4.11: Longitudinal phonon modes of $YMnO_3$ near M point at different temperatures and the theoretical calculation (solid lines) considering spin lattice coupling 3.10 revealing coupling of spin and inplane lattice modulation.

surements. Surprisingly, I couldn't found any gap opening near q = (0.175 0 12) as previously reported. The symmetry allowed components which can induce linear magnon phonon coupling is in-plane DM interaction and off-diagonal SIA, which is about two orderes of magnitude smaller than exchange energy. Therefore, such small terms are not likely to induce the large coupling observed. Indeed, the calculation based on SIA driven magnon-phonon coupling shows the gap opening at the completely different q point [59].

Instead, only a slight change in phonon energies near the crossing point is observed as shown by Fig. 4.12. Although the observed effect is much smaller than previously reported, the q point of gap opening is same as the previous calculation [59]. It is also qualitatively reproduced by the SIA based model 3.56 considering the out-of-plane oxygen displacements. The magnetostriction coefficient β used here is 1 meV/. From previous DFT results, the value of the off-diagonal element in SIA tensor is estimated to be order of 0.1 meV. This, together with the oxygen c-axis displacement of 0.2 Åin the ferroelectric phase, β is estimated to be about 0.5 mev/Å. Considering that there can also be contributions from DM interaction, the estimated value of 0.5 is not far from the experimental value of 1. Such DM interaction and the off diagonal component of SIA in h-$RMnO_3$ compounds causes canted moment along c-axis, as discusse in section 4.1. When weak

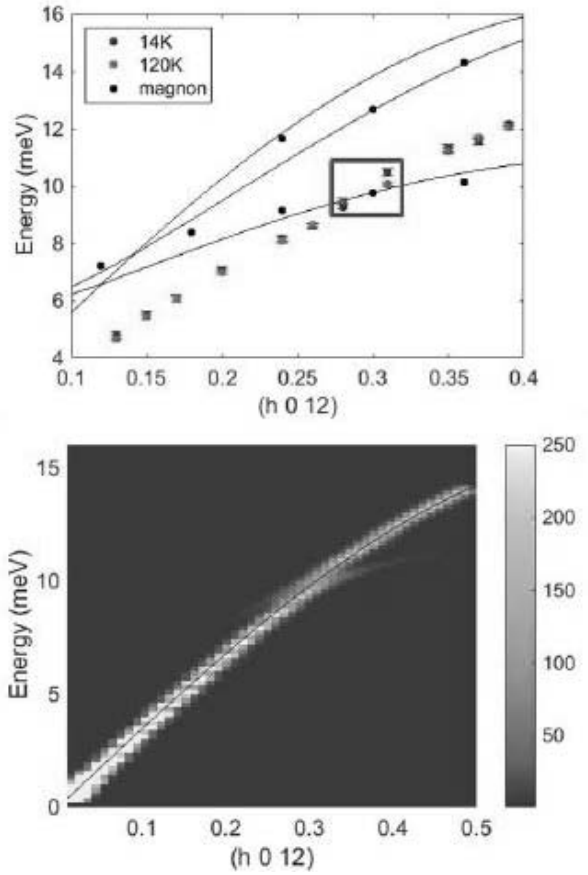

Figure 4.12: (Top) Energy change of transverse acoustic phonon near the crossing with magnon. (Bottom) Calculated phonon spectra considering coupling of spin and out-of-plane lattice modulation by SIA 3.56.

ferromagnetic moment is allowed by symmetry, like for $LuFeO_3$ and $ScMnO_3$, these terms are central for multiferroic property i.e. the electric control of the net magnetic moment. Thus, the spin lattice Hamiltonian of $YMnO_3$ determined by the present study may shed light on the coupling of spin, charge and lattice degrees of freedom in this fascinating multiferroic compound.

5. Conclusion

5.1 Outlook

I have showed that magnon-phonon coupling is important for the excitation spectra of 2D THA $RMnO_3$. A natural question arising out of this work is that how general such magnon phonon coupling occurs in other materials. To answer this question, it is important to estimate the exchange striction constant $\tilde{\alpha} = \frac{\alpha d}{J}$ in equation 3.2.1 for other systems. Compared to $\tilde{\alpha} = 16$ for the (Y,Lu)MnO_3 case, $\tilde{\alpha}$ is about twice larger and smaller for $CuCrO_2$ and La_2CuO_4, according to pressure experiments [87–89]. A more convenient estimation of such spin-lattice coupling can be made by measuring the change of lattice constants as a function of temperature. The change of the distance d between the magnetic ions below T_N can be expressed as $\Delta d = \frac{\alpha S^2}{K}$. For $YMnO_3$, this value is estimated to be 0.002 Å [38, 90], which is not much larger than many other magnetic systems. It is similar to orthorombic $RMnO_3$ case ($\alpha \approx 0.001$ Å) [91] and α-$SrCr_2O_4$ [92] and (Mn,Fe,Ni)F_2 ($\alpha \approx 0.003$ Å) [93]. Furthermore, the spin phonon coupling observed from optical experiments are also similar to those of other transition metal oxides. IR and Raman experiments reported about 0.6% phonon energy change in $RMnO_3$ while similar changes are observed in $RCrO_3$ [94], orthorombic $RMnO_3$ [95] and $Ca_3Co_4O_9$ [96]. Therefore, we observe that $\tilde{\alpha}$ in $RMnO_3$ is similar to many other magnetic materials and so magnon-phonon coupling can be a common feature for other triangular antiferromagnets with a non-collinear magnetic order. Indeed, recent inelastic neutron and x-ray scattering experiments reported the clear evidence of magnon phonon coupling in 2D THA $LiCrO_2$ [25] and $CuCrO_2$ [97].

Looking beyond the 2D triangular antiferromagnets, we believe that the idea of magnon–phonon coupling can also be important in the studies of other interesting magnetic systems. First, the analysis similar to $RMnO_3$ might shed a light on the investigation of spin-lattice coupling mechanism with unusual thermal expansion behavior materials. One candidate is antiperovskite Mn_3XN (X=Sn,Ge,Cu) which exhibits large negative thermal expansion when the spins order with 120° noncollinear structure [98]. Second, a large magnon phonon coupling can be used to investigate the magnetic ground states and excitations in 5d transition metal oxides. Currently, such studies have been carried out only on few limited samples

mainly due to poor resolutions of resonant inelastic x-ray scattering [99] and too small single crystal sizes available for inelastic neutron scattering. Note that investigation of phonon spectra using inelastic x-ray scattering can be an alternative method [100], because large magnon-phonon coupling is expected for 5d transition metal oxides with noncollinear spin structure such as pyrochlore iridates [101] and osmate [102], which exhibit large spin-lattice coupling [103].

Another fruitful direction worth exploring is to realize an ideal 2D THA and identify the magnon energy renormalization. A weak point of the current nonlinear spinwave calculations for $RMnO_3$ is that I did not consider the real part of magnon self energy in the analysis presented in this thesis, due to the difficulty of the calculation including magnon phonon coupling. One way to avoid such complication is to seperate magnon and phonon energies by studying materials with small exchange interactions, such as $RbFe(MoO_4)_2$ [104]. Another way is to find materials with small α value such as cuprate; 2D THA with a small spin-lattice coupling is rare.

5.2 Summary

To summarize, I mapped out the full spin waves and phonon excitations of $(Y,Lu)MnO_3$ over the Brillouin zone. By carrying out the calculations using the completel Hamiltonian with both magnons and phonons on an equal footing and their coupling, I have demonstrated the magnon-phonon hybridization in our inelastic neutron and x-ray scattering data, which is originating from the noncollinear spin structure.

Furthermore, I have identified the linewidth broadening of the resulting hybrid mode, which is well reproduced by the calculation including cubic nonlinear terms. These nonlinear effects also arise from the noncollinear spin structure, which in the case of $RMnO_3$ is the 120° structure, suggesting that the nonlinear quantum effect may still be observed in systems closer to the classical limit. As there are many other antiferromagnets with a noncollinear ordered structure, we expect to see many more spin systems exhibit such interesting effects.

Appendix A. Codes for the calculation of magnon phonon coupling

To calculate and diagonalize the magnon phonon coupling Hamiltonian, I made a MATLAB code *RMO_ mp2.m*.

```
function [E,V]=RMO_mp2(kx,ky,kz,vpk,w1k)
num=96;%matrix size
S=2;
J1=2.5;%2.5 YMnO3/ 3 LuMnO3/ 2.7 YLMO
J2=2.5;
d1=0.28;
d2=-0.02;
ap1=0;ap2=0;
g1=ap1*J1;g2=ap2*J1;
w2k=w1k/8.065;
% vpk=abs(vpk);
a=[6.0760778956701698    0.0000000000000000    0.0000000000000000];
b=[-3.0380389478350849    5.2612218396265655   -0.0008125388379104];
c=[0.0000000000000000   -0.0017386792259000   11.4306544195067499];
at=2*pi*cross(b,c)/dot(a,cross(b,c));
bt=2*pi*cross(c,a)/dot(a,cross(b,c));
ct=2*pi*cross(a,b)/dot(a,cross(b,c));
k=kx*at+ky*bt+kz*ct;
e1=[-1 0 0]; e2=[1/2,sqrt(3)/2,0]; e3=[1/2,-sqrt(3)/2,0];
A1=(J1+J2*(exp(1i*dot(k,a))+exp(-1i*dot(k,b))))/8;
B1=(J1*exp(1i*dot(k,-a-b))+J2*(1+exp(1i*dot(k,-a))))/8;
C1=(J1*exp(1i*dot(k,a+b))+J2*(1+exp(1i*dot(k,b))))/8;
A2=(J2*exp(1i*dot(k,a))+J1*exp(1i*dot(k,a-b))+J2*exp(1i*dot(k,-b)))/8;
B2=(J2+J2*exp(1i*dot(k,-a))+J1*exp(1i*dot(k,b)))/8;
C2=(J1*exp(1i*dot(k,-a))+J2+J2*exp(1i*dot(k,b)))/8;
del=J1/2+J2+d1/2-d2;
A12=g1*(e2*exp(1i*dot(k,a))+e3*exp(1i*dot(k,-b))+e1)/2;
A23=g1*(e3*exp(1i*dot(k,-a-b))+e2+e1*exp(1i*dot(k,-a)))/2;
A31=g1*(e1*exp(1i*dot(k,b))+e2*exp(1i*dot(k,a+b))+e3)/2;
```

```
A21=g1*(e1*exp(-1i*dot(k,a))+e2*exp(-1i*dot(k,-b))+e3)/2;
A32=g1*(e1*exp(-1i*dot(k,-a-b))+e1+e3*exp(1i*dot(k,a)))/2;
A13=g1*(e3*exp(-1i*dot(k,b))+e1*exp(-1i*dot(k,a+b))+e2)/2;
A45=-g1*(e3*exp(1i*dot(k,a))+e1*exp(1i*dot(k,a-b))+e2*exp(1i*dot(k,-b)))
A56=-g1*(e3*exp(1i*dot(k,b))+(e1+e2*exp(1i*dot(k,-a))))/2;%-
A64=-g1*(e2*exp(1i*dot(k,-a))+(e3*exp(1i*dot(k,b))+e1))/2;%-
A54=-g1*(e2*exp(-1i*dot(k,a))+e3*exp(-1i*dot(k,a-b))+e1*exp(-1i*dot(k,-b
A65=-g1*(e2*exp(-1i*dot(k,b))+(e3+e1*exp(-1i*dot(k,-a))))/2;%-
A46=-g1*(e1*exp(-1i*dot(k,-a))+(e2*exp(-1i*dot(k,b))+e3))/2;%-

zz=[0 0 1];
AA1=g2*zz*(exp(1i*dot(k,a))+exp(1i*dot(k,-b))-1)/2;
BB1=g2*zz*((-exp(1i*dot(k,-a-b))+1+exp(1i*dot(k,-a))))/2;
CC1=g2*zz*(exp(1i*dot(k,b))-exp(1i*dot(k,a+b))+1)/2;
AA2=g2*zz*(exp(1i*dot(k,a))-exp(1i*dot(k,a-b))+exp(1i*dot(k,-b)))/2;%-
BB2=g2*zz*(-exp(1i*dot(k,b))+1+exp(1i*dot(k,-a)))/2;%-
CC2=g2*zz*(-exp(1i*dot(k,-a))+exp(1i*dot(k,b))+1)/2;%-
del1=g2*zz/2;

X1=S*[del A1 conj(C1);conj(A1) del B1;C1 conj(B1) del];
X2=S*[del A2 conj(C2);conj(A2) del B2;C2 conj(B2) del];
L=[X1 1e-3*eye(3);1e-3*eye(3) X2];
Y1=S*[d1/2 3*A1 3*conj(C1);3*conj(A1) d1/2 3*B1;3*C1 3*conj(B1) d1/2];
Y2=S*[d1/2 3*A2 3*conj(C2);3*conj(A2) d1/2 3*B2;3*C2 3*conj(B2) d1/2];
M=[Y1 1e-3*eye(3);1e-3*eye(3) Y2];
G=diag(w2k(1:90)/2);
N=zeros(90,6);

vpk=conj(vpk);
for j=1:90 %Mn
    N(j,1)=A31*vpk(25:27,j)-A21*vpk(22:24,j)+conj(AA1)*vpk(22:24,j)+CC1*
    N(j,2)=A12*vpk(19:21,j)-A32*vpk(25:27,j)+AA1*vpk(19:21,j)+conj(BB1)*
    N(j,3)=A23*vpk(22:24,j)-A13*vpk(19:21,j)+conj(CC1)*vpk(19:21,j)+BB1*
    N(j,4)=A64*vpk(34:36,j)-A54*vpk(31:33,j)+conj(AA2)*vpk(31:33,j)+CC2*
    N(j,5)=A45*vpk(28:30,j)-A65*vpk(34:36,j)+AA2*vpk(28:30,j)+conj(BB2)*
```

```
    N(j,6)=A56*vpk(31:33,j)-A46*vpk(28:30,j)+conj(CC2)*vpk(28:30,j)+BI
    N(j,:)=N(j,:)/sqrt(w2k(j));
end

H=[L,-1i*0.1683*S*N',M,-1i*0.1683*S*N';1i*0.1683*S*N,G,-1i*0.1683*S*N,

% H=[L,M;M,L];
g=[eye(num),zeros(num);zeros(num),-eye(num)];
[v,e]=eig(2*g*H);
% E=e;V=v;
% {
[E1,n]=sort(real(diag(e)),'descend');
% [~,m]=sort(real(diag(e)));
vp=zeros(2*num,2*num);
for j=1:num%length(n/2)
    vp(:,j)=v(:,n(j));
    vp(:,j+num)=[zeros(num) eye(num);eye(num) zeros(num)]*v(:,n(j));
end
d=diag(g*vp'*g*vp);
V=zeros(2*num);
for j=1:2*num
    V(:,j)=vp(:,j)/sqrt(d(j));
end
E=diag(E1(1:num));
```

To calculate the dynamical spin structure factor, I made a MATLAB code *RMO_mp_Sqw.m.*

```
function [s,E]=RMO_mp_Sqw(kx,ky,kz,vpk,w1k)
num=96;%matrix size
[E,V]=RMO_mp2(kx,ky,kz,vpk,w1k);%out of plane
%[E,V]=LMO_mp1(kx,ky,kz,vpk,w1k);%super exchangestriction
a=[6.0760778956701698    0.0000000000000000    0.0000000000000000];
b=[-3.0380389478350849    5.2612218396265655   -0.0008125388379104];
c=[0.0000000000000000   -0.0017386792259000   11.4306544195067499];
at=2*pi*cross(b,c)/dot(a,cross(b,c));
```

```
bt=2*pi*cross(c,a)/dot(a,cross(b,c));
ct=2*pi*cross(a,b)/dot(a,cross(b,c));
k=kx*at+ky*bt+kz*ct;
%% atom positions
r=zeros(6,3);
r(1,:)=a/3+c;
r(2,:)=b/3+c;
r(3,:)=2*a/3+2*b/3+c;
r(4,:)=2*a/3+c/2;
r(5,:)=2*b/3+c/2;
r(6,:)=a/3+b/3+c/2;
%% Expressing spin operators with magnon operators
X=zeros(6,2*num,3);
% {
X(:,:,3)=[V(1,:)+V(num+1,:);V(2,:)+V(num+2,:);V(3,:)+V(num+3,:);V(4,:)+\
X(:,:,1)=[zeros(1,2*num);-(1i*sqrt(3)/2)*(V(2,:)-V(num+2,:));(1i*sqrt(3)
X(:,:,2)=[-1i*(V(1,:)-V(1+num,:));(1i/2)*(V(2,:)-V(2+num,:));(1i/2)*(V(3
%}
%{
X(:,:,3)=[V(1,:)+V(num+1,:);V(2,:)+V(num+2,:);V(3,:)+V(num+3,:);V(4,:)+\
X(:,:,2)=[zeros(1,2*num);-(1i*sqrt(3)/2)*(V(2,:)-V(num+2,:));(1i*sqrt(3)
X(:,:,1)=-[-1i*(V(1,:)-V(1+num,:));(1i/2)*(V(2,:)-V(2+num,:));(1i/2)*(V
%}
%{
X(:,:,3)=[V(1,:)+V(num+1,:);V(2,:)+V(num+2,:);V(3,:)+V(num+3,:);V(4,:)+\
X(:,:,2)=([zeros(1,2*num);-(1i*sqrt(3)/2)*(V(2,:)-V(num+2,:));(1i*sqrt(3
X(:,:,1)=(-[-1i*(V(1,:)-V(1+num,:));(1i/2)*(V(2,:)-V(2+num,:));(1i/2)*(\
%}
%% S(Q,w)
S=zeros(3,3,num);
for p=1:num
    for i=1:6
        for j=1:6
            for n=1:3
                for m=1:3
```

```
            S(n,m,p)=S(n,m,p)+exp(1i*dot(k,r(j,:)-r(i,:)))*X(i,p,n)*X
                end
            end
        end
    end
end
s=zeros(1,num);
for n=1:3
    for m=1:3
        for p=1:num
        s(1,p)=s(1,p)+(fix(min(n,m)/max(n,m))-k(n)*k(m)/(norm(k))^2)*
        end
    end
end
s=s/num;
```

To calculate the dynamical phonon structure factor, I mase a MATLAB code *RMO_mp_phonon_color.m*.

```
%% nuclear dynamical structure factor
num=90;rat=1;
m1=88.9;%YMO 88.9/ LMO 174.97
m2=54.9;m3=16;
z1=39;% x-ray form factor YMO 39/ LMO 71
z2=25;z3=8;
b1=7.75;b2=3.73;b3=7.75;
upk=vp;
upk(1:18,:,:)=z1*vp(1:18,:,:)/sqrt(m1);
upk(19:36,:,:)=z2*vp(19:36,:,:)/sqrt(m2);
upk(37:90,:,:)=z3*vp(37:90,:,:)/sqrt(m3);
% vpk=vp;
% vpk(1:18,:,:)=b1*vp(1:18,:,:)/sqrt(m1);
% vpk(19:36,:,:)=b2*vp(19:36,:,:)/sqrt(m2);
% vpk(37:90,:,:)=b3*vp(37:90,:,:)/sqrt(m3);
s=zeros(nqpoint,90);
a=[6.0760778956701698    0.0000000000000000    0.0000000000000000];
```

```
b=[-3.0380389478350849    5.2612218396265655   -0.0008125388379104];
c=[0.0000000000000000   -0.0017386792259000   11.4306544195067499];
at=2*pi*cross(b,c)/dot(a,cross(b,c));
bt=2*pi*cross(c,a)/dot(a,cross(b,c));
ct=2*pi*cross(a,b)/dot(a,cross(b,c));
kx0=0;ky0=0;kz0=0;
E=zeros(nqpoint,96);V=zeros(90,96,nqpoint);E1=zeros(nqpoint,6);

Qi=1;Qf=nqpoint;
parfor i=Qi:Qf
    kx=q1(i,1);ky=q1(i,2);kz=q1(i,3);%1.5 for YMnO3/ 1.8 for LuMnO3
    vpk=up(:,:,i);w1k=w1(i,:); %multiply 1.1 for YMnO3
    [e,v]=RMO_mp2(kx,ky,kz,vpk,w1k);
    [ee,~]=RMO_magnon(kx,ky,kz);
    V(:,:,i)=v(7:96,1:96);
    E(i,:)=diag(e)';
    E1(i,:)=diag(ee)';
end

for i=Qi:Qf
    k=(kx0+q1(i,1))*at+(ky0+q1(i,2))*bt+q1(i,3)*ct;
    kp=kron(ones(1,30),k);
    Up=upk(:,:,i);Vp=V(:,:,i);
    U=Up*Vp;
    for j=1:96
        sk=kp*U(:,j);
        s(i,j)=sk*sk'/E(i,j);
    end
end

for i=1:nqpoint
    for j=1:96
        s(i,j)=s(i,j)*heaviside(real(s(i,j)));
        if s(i,j)>1e4;
            s(i,j)=0;
```

```
        else
        end
    end
end


Q1=1:204;
e=0:0.5:50;
[x,y]=meshgrid(e,Q1);
sigma=[7/2.33,1.5/2.33];%[6/2.33 1.2/2.33]
s1=[s(1:51,:);s(103:153,:);s(205:255,:);s(307:357,:)];
I1=real(s1);
EE=[E(1:51,:);E(103:153,:);E(205:255,:);E(307:357,:)];
omega=rat*real(EE);
Z1=zeros(size(x));
Z1 = convolute(Q1,omega,I1,y,x,Z1,sigma);
myscale=[5,500];%[50 5000]
figure;
pcolor(y,x,log10(Z1+1e-6))
shading flat
caxis(myscale);
%set(gca,'XTick',[1 51 102 153 204],'XTickLabel',{'A03','A08 A19','A1
set(gca,'XTick',[1 51 102 153 204],'XTickLabel',{'A03','A08 A14','A19
xlabel('Detectors');
ylabel('Energy (meV)');
h=colorbar;
ticks_wanted=unique([myscale(1),get(h,'YTick'),myscale(2)]);
% or for example ticks_wanted=10.^(2:4);
caxis(log10(myscale))
set(h,'YTick',log10(ticks_wanted));
set(h,'YTickLabel',ticks_wanted,'fontsize',10);
hold on
plot(Q1,EE,'k','linewidth',1)
title('Near (4 0.5 0)');%xy
% title('Near (0.17 0 12)');%z
```

```
%{
detn=[9 17 25 60 68 76 101 109 117];
figure
for i=1:length(detn)
subplot(3,3,10-i)
plot(e,Z(detn(i),:),'k')
hold all
plot(e,Z1(detn(i),:),'r')
xlim([5 20])
end
%}
```

Appendix B. Codes for the calculation of decay rate

To calculate decay rate with magnon phonon coupling, I made MATLAB codes *vparam_sp2.m* and *vnlsw_sp1.m*

```
function [E0,E1,u1,u2,v1,v2,g,gp]=vparam_sp2(J,S,a,e1,ap,kx,ky)
gam=(cos(kx)+2*cos(kx/2).*cos(sqrt(3)*ky/2))/3;
A=3*J*S*((a-1/2)*gam+1);
B=3*J*S*(1+2*a)*gam/2;
e0=sqrt(A.^2-B.^2);
u=(((A+B)./(A-B)).^(1/4)+((A-B)./(A+B)).^(1/4))/2;
v=(((A+B)./(A-B)).^(1/4)-((A-B)./(A+B)).^(1/4))/2;
l1=-(sqrt(3)/2)*(exp(1i*(-kx/2-sqrt(3)*ky/2))-exp(-1i*kx))+(sqrt(3)/2)
l2=(exp(1i*(-kx/2+sqrt(3)*ky/2))-exp(-1i*(-kx/2-sqrt(3)*ky/2)))-(1/2)*
l=sqrt(conj(l1).*l1+conj(l2).*l2);
c=0.1683*ap*J*S*(u+v).*l/sqrt(e1);
E0=sqrt((e0.^2+e1.^2-sqrt((e0.^2+e1.^2).^2-4*(e0.^2.*e1.^2-4*c.^2.*e0
E1=sqrt((e0.^2+e1.^2+sqrt((e0.^2+e1.^2).^2-4*(e0.^2.*e1.^2-4*c.^2.*e0
a1=(1+(c./(E0-e1)).^2).^(-1/2);
a2=(1+(c./(E1-e0)).^2).^(-1/2);
x1=a1;
x2=(c.*a2./(E1-e0));
x3=0;
x4=(c.*a2./(-E1-e0));
u1=u.*x1+v.*x3;
u2=u.*x2+v.*x4;
v1=u.*x3+v.*x1;
v2=u.*x4+v.*x2;
% u1=(u-((E0-e0)./(E0+e0)).*v).*a1;
% u2=((c./(E1-e0)).*(1-(E1-e1)./(E1+e1)).*u-(c./(E1+e0)).*(1-(E1-e1)./
% v1=(-((-E0+e0)./(-E0-e0)).*u+v).*b1;
% v2=((c./(-E1-e0)).*(1-(-E1+e1)./(-E1-e1)).*u-(c./(-E1+e0)).*(1-(-E1-
g=gam;
gp=(sin(kx)-2*sin(kx/2).*cos(sqrt(3)*ky/2))/3;
```

```
function [en1,en2,r0,r1]=vnlsw_sp1(J,S,a,e1,ap,kx,ky)
[E0k,E1k,u1k,u2k,v1k,v2k,gk,gpk]=vparam_sp2(J,S,a,e1,ap,kx,ky);


N=1e6;t=1e4;


qh=rand(1,N);qk=rand(1,N);
qx=(4*pi/3)*1.5*qh;
qy=(4*pi/3)*sqrt(3)*(qh/2+qk);
[E0q,E1q,u1q,u2q,v1q,v2q,gq,gpq]=vparam_sp2(J,S,a,e1,ap,qx,qy);
[E0km,E1km,u1km,u2km,v1km,v2km,gkm,gpkm]=vparam_sp2(J,S,a,e1,ap,kx-qx,ky
% [E0kp,E1kp,u1kp,u2kp,v1kp,v2kp,gkp,gpkp]=vparam_sp1(J,S,a,e1,ap,-kx-qx
%% show number of NaN values
%{
c0=isnan(gpq);disp(sum(c0));
c1=isnan(u1q);disp(sum(c1));
c2=isnan(v1q);disp(sum(c2));
%}
%% calculate decay rate
g112=gpq.*(u1q+v1q).*(u1km.*u2k+v1km.*v2k)+gpkm.*(u1km+v1km).*(u1q.*u2k+
g122=gpq.*(u1q+v1q).*(u2km.*u2k+v2km.*v2k)+gpkm.*(u2km+v2km).*(u1q.*u2k+
g222=gpq.*(u2q+v2q).*(u2km.*u2k+v2km.*v2k)+gpkm.*(u2km+v2km).*(u2q.*u2k+
g111=gpq.*(u1q+v1q).*(u1km.*u1k+v1km.*v1k)+gpkm.*(u1km+v1km).*(u1q.*u1k+
g121=gpq.*(u1q+v1q).*(u2km.*u1k+v2km.*v1k)+gpkm.*(u2km+v2km).*(u1q.*u1k+
g221=gpq.*(u2q+v2q).*(u2km.*u1k+v2km.*v1k)+gpkm.*(u2km+v2km).*(u2q.*u1k+

R=(27*J^2*S/2);

r1=R*(pi/2)*sqrt(t/pi)*g112.^2.*exp(-t*(E0q+E0km-E1k).^2);
% r1=R*(pi/2)*sqrt(t/pi)*g112.^2.*exp(-t*(E0q+E0km-E1k).^2)+2*R*(pi/2)*s
r1=sum(r1)/N;
r0=R*(pi/2)*sqrt(t/pi)*g111.^2.*exp(-t*(E0q+E0km-E0k).^2)+2*R*(pi/2)*sqr
r0=sum(r0)/N;
```

en1=E0k;en2=E1k;

Publications

1. "Magnon Breakdown in a Two Dimensional Triangular Lattice Heisenberg Antiferromagnet of Multiferroic $LuMnO_3$"
   Joosung Oh, Manh Duc Le, Jaehong Jeong, Jung-hyun Lee, Hyungje Woo, Wan-Young Song, T. G. Perring, W. J. L. Buyers, S.-W. Cheong, and Je-Geun Park
   Physical Review Letters **111**, 257202 (2013) Editor's Suggestion

2. "Hexagonal $RMnO_3$: a model system for two dimensional triangular lattice antiferromagnets"
   Hasung Sim, Joosung Oh, Jaehong Jeong, Manh Duc Le and Je-Geun Park
   Acta Crystallographica Section B **72**, 3 (2016)

3. "Magnon-Phonon coupling and two-magnon continuum in the two-dimensional triangular antiferromagnet $CuCrO_2$"
   Kisoo Park, Joosung Oh, Jonathan C. Leiner, Jaehong Jeong, Kirrily C. Rule, Manh Duc Le and Je-Geun Park
   Physical Review B **94**, 104421 (2016)

4. "Spontaneous decays of magneto-elastic excitations in non-collinear antiferromagnet $(Y,Lu)MnO_3$"
   Joosung Oh, Manh Duc Le, Ho-Hyun Nahm, Hasung Sim, Jaehong Jeong, T.G. Perring, Hyungje Woo, Kenji Nakajima, Seiko Ohira-Kawamura, Zahra Yamani, Y. Yoshida, H. Eisaki, S.-W. Cheong, A. L. Chernyshev and Je-Geun Park
   Nature Communications **7**, 13146 (2016)

Conference Presentations

(Oral presentations)

1. Decay and anomalous spectrum of magnon observed in h-$LuMnO_3$.
   HANARO Symposium (May. 2013 in Korea)

2. Spin phonon induced magnetic soft mode in triangular antiferromagnet h-$RMnO_3$.
   American Physical Society March meeting (Mar. 2015 at San Antonio, US)

3. Spin phonon induced magnetic soft mode in triangular antiferromagnets h-(Y,Lu)MnO_3.
   2015 Korean Physical Society Spring Meeting (Apr. 2015 in Korea)

4. Spontaneous decays of magneto-elastic excitation in noncollinear magnets (Y/Lu)MnO_3.
   Correlated Electron Systems" Gordon Research Seminar (Jun. 2016 in South Hedley, US)

5. Magnon phonon hybridization and enhanced anharmonicity in noncollinear magnets (Y,Lu)MnO_3.
   American Physical Society March meeting (Mar. 2017 at New Orleans, US)

(Poster presentations)

1. To understand the specific heat of (Y/Lu)MnO_3 using inelastic neutron scattering data.
   2013 Korean Physical Society Spring meeting (Apr. 2013 in Korea)

2. To understand the specific heat anomaly of (Y/Lu)MnO_3 using inelastic neutron scattering data
   13^{th} Japan Korea Taiwan Symposium (Jan. 2013 in Japan)

3. Excitation spectrum of 2D triangular Heisenberg antiferromagnet hexagonal $LuMnO_3$
   Quantum materials symposium (Feb. 2014 in Korea)

4. Magnon breakdown in a two dimensional triangular Heisenberg antiferromagnet $LuMnO_3$
   American Physical Society March meeting (Mar. 2014 in US)

5. Observation of magnon decay and non-linear spinwaves in $LuMnO_3$
   2014 Korean Physical Society Spring meeting (Apr. 2014 in Korea)

6. Spin phonon induced magnetic soft mode in triangular antiferromagnets (Y/Lu)MnO_3
   15^{th} Taiwan Japan Korea Symposium (Mar. 2015 in Taiwan)

7. Inelastic neutron scattering studies on magnon phonon coupling in triangular antiferromagnets $Y_{1-x}Lu_xMnO_3$
   14^{th} PSI Summer School on Condensed Matter Research (Aug. 2015 in Switzerland)

References

[1] C. L. Henley, Phys. Rev. Lett. **62**, 2056 (1989).

[2] O. Tchernyshyov, R. Moessner, and S. L. Sondhi, Phys. Rev. Lett. **88**, 067203 (2002).

[3] A. L. Chernyshev and M. E. Zhitomirsky, Phys. Rev. Lett. **97**, 207202 (2006).

[4] J. H. Kim and J. H. Han, Phys. Rev. B **76**, 054431 (2007).

[5] E. Manousakis, Rev. Mod. Phys. **63**, 1 (1991).

[6] B. Dalla Piazza, M. Mourigal, N. B. Christensen, G. Nilsen, P. Tregenna-Piggott, T. Perring, M. Enderle, D. F. McMorrow, D. Ivanov, and H. M. Rønnow, Nature physics **11**, 62 (2015).

[7] M. Powalski, G. S. Uhrig, and K. P. Schmidt, Phys. Rev. Lett. **115**, 207202 (2015).

[8] .

[9] T.-H. Han, J. S. Helton, S. Chu, D. G. Nocera, J. A. Rodriguez-Rivera, C. Broholm, and Y. S. Lee, Nature **492**, 406 (2012).

[10] A. Banerjee, J. Yan, J. Knolle, C. A. Bridges, M. B. Stone, M. D. Lumsden, D. G. Mandrus, D. A. Tennant, R. Moessner, and S. E. Nagler, Science **356**, 1055 (2017).

[11] G. H. Wannier, Phys. Rev. **79**, 357 (1950).

[12] P. W. Anderson, Materials Research Bulletin **8**, 153 (1973).

[13] B. Bernu, P. Lecheminant, C. Lhuillier, and L. Pierre, Phys. Rev. B **50**, 10048 (1994).

[14] R. R. P. Singh and D. A. Huse, Phys. Rev. Lett. **68**, 1766 (1992).

[15] D. J. J. Farnell, R. F. Bishop, and K. A. Gernoth, Phys. Rev. B **63**, 220402 (2001).

[16] L. Capriotti, A. E. Trumper, and S. Sorella, Phys. Rev. Lett. **82**, 3899 (1999).

[17] S. R. White and A. L. Chernyshev, Phys. Rev. Lett. **99**, 127004 (2007).

[18] W. Zheng, J. O. Fjærestad, R. R. P. Singh, R. H. McKenzie, and R. Coldea, Phys. Rev. Lett. **96**, 057201 (2006).

[19] W. Zheng, J. O. Fjærestad, R. R. P. Singh, R. H. McKenzie, and R. Coldea, Phys. Rev. B **74**, 224420 (2006).

[20] O. A. Starykh, A. V. Chubukov, and A. G. Abanov, Phys. Rev. B **74**, 180403 (2006).

[21] A. L. Chernyshev and M. E. Zhitomirsky, Phys. Rev. B **79**, 144416 (2009).

[22] M. E. Zhitomirsky and A. L. Chernyshev, Rev. Mod. Phys. **85**, 219 (2013).

[23] R. Coldea, D. A. Tennant, A. M. Tsvelik, and Z. Tylczynski, Phys. Rev. Lett. **86**, 1335 (2001).

[24] M. Kohno, O. A. Starykh, and L. Balents, Nat. Phys. **3**, 790 (2007).

[25] S. Toth, B. Lake, K. Hradil, T. Guidi, K. C. Rule, M. B. Stone, and A. T. M. N. Islam, Phys. Rev. Lett. **109**, 127203 (2012).

[26] T. Chatterji, S. Ghosh, a. Singh, L. Regnault, and M. Rheinstädter, Phys. Rev. B **76**, 144406 (2007).

[27] O. P. Vajk, M. Kenzelmann, J. W. Lynn, S. B. Kim, and S. W. Cheong, Phys. Rev. Lett. **94**, 087601 (2005).

[28] H. Yakel, W. Koehler, E. Bertaut, and E. Forrat, Acta Crystallographica **16**, 957 (1963).

[29] B. B. Van Aken and T. T. M. Palstra, Phys. Rev. B **69**, 134113 (2004).

[30] D. Y. Cho, J. Y. Kim, B. G. Park, K. J. Rho, J. H. Park, H. J. Noh, B. J. Kim, S. J. Oh, H. M. Park, J. S. Ahn, H. Ishibashi, S. W. Cheong, J. H. Lee, P. Murugavel, T. W. Noh, a. Tanaka, and T. Jo, Phys. Rev. Lett. **98**, 217601 (2007).

[31] J. Oh, M. D. Le, J. Jeong, J.-h. Lee, H. Woo, W.-Y. Song, T. G. Perring, W. J. L. Buyers, S.-W. Cheong, and J.-G. Park, Phys. Rev. Lett. **111**, 257202 (2013).

[32] M. Fiebig, T. Lottermoser, and R. V. Pisarev, J. Appl. Phys. **93**, 8194 (2003).

[33] H. Sim, J. Oh, J. Jeong, M. D. Le, and J.-G. Park, Acta Crystallographica Section B: Structural Science, Crystal Engineering and Materials **72**, 3 (2016).

[34] P. J. Brown and T. Chatterji, J. Phys.: Condens. Matter **18**, 10085 (2006).

[35] M. Fiebig, D. Fröhlich, K. Kohn, S. Leute, T. Lottermoser, V. V. Pavlov, and R. V. Pisarev, Phys. Rev. Lett. **84**, 5620 (2000).

[36] M. Fiebig, J. Phys. D **38**, R123 (2005).

[37] M. Fiebig, T. Lottermoser, D. Fröhlich, A. V. Goltsev, and R. V. Pisarev, Nature **419**, 818 (2002).

[38] S. Lee, A. Pirogov, M. Kang, K.-H. Jang, M. Yonemura, T. Kamiyama, S.-W. Cheong, F. Gozzo, N. Shin, H. Kimura, Y. Noda, and J.-G. Park, Nature **451**, 805 (2008).

[39] A. V. Goltsev, R. V. Pisarev, T. Lottermoser, and M. Fiebig, Phys. Rev. Lett. **90**, 177204 (2003).

[40] S. C. Chae, N. Lee, Y. Horibe, M. Tanimura, S. Mori, B. Gao, S. Carr, and S.-W. Cheong, Phys. Rev. Lett. **108**, 167603 (2012).

[41] S. C. Chae, Y. Horibe, D. Y. Jeong, N. Lee, K. Iida, M. Tanimura, and S.-W. Cheong, Phys. Rev. Lett. **110**, 167601 (2013).

[42] S. Artyukhin, K. T. Delaney, N. A. Spaldin, and M. Mostovoy, Nat. Mater. **13**, 42 (2014), arXiv:1204.4126 .

[43] M. Poirier, F. Laliberte, L. Pinsard, and A. Revcolevschi, Phys. Rev. B **76**, 174426 (2007), arXiv:0708.0754 .

[44] T. Katsufuji, S. Mori, M. Masaki, Y. Moritomo, N. Yamamoto, and H. Takagi, Phys. Rev. B **64**, 104419 (2001).

[45] J. Park, S. Lee, M. Kang, K. H. Jang, C. Lee, S. V. Streltsov, V. V. Mazurenko, M. V. Valentyuk, J. E. Medvedeva, T. Kamiyama, and J. G. Park, Phys. Rev. B **82**, 054428 (2010).

[46] J. Vermette, S. Jandl, and M. M. Gospodinov, J. Phys.: Condens. Matter **20**, 425219 (2008).

[47] J. Vermette, S. Jandl, A. A. Mukhin, V. Y. Ivanov, A. Balbashov, M. M. Gospodinov, and L. Pinsard-Gaudart, J. Phys.: Condens. Matter **22**, 356002 (2010).

[48] H. Fukumura, S. Matsui, H. Harima, K. Kisoda, T. Takahashi, T. Yoshimura, and N. Fujimura, J. Phys.: Condens. Matter **19**, 365239 (2007).

[49] H. Fukumura, N. Hasuike, H. Harima, K. Kisoda, K. Fukae, T. Yoshimura, and N. Fujimura, J. Phys.: Condens. Matter **21**, 064218 (2009).

[50] A. P. Litvinchuk, M. N. Iliev, V. N. Popov, and M. M. Gospodinov, J. Phys.: Condens. Matter **16**, 809 (2004).

[51] R. Basistyy, T. N. Stanislavchuk, A. A. Sirenko, A. P. Litvinchuk, M. Kotelyanskii, G. L. Carr, N. Lee, X. Wang, and S.-W. Cheong, Phys. Rev. B **90**, 024307 (2014).

[52] F. Wang and A. Vishwanath, Phys. Rev. Lett. **100**, 077201 (2008).

[53] J. Jeong, S. Lee, and J.-G. Park, J. Korean Magn. Soc. **22**, 103 (2012).

[54] G. L. Squires, *Introduction to the theory of thermal neutron scattering* (Cambridge university press, 2012).

[55] A. Furrer, T. StrÃ, *et al.*, *Neutron scattering in condensed matter physics* (World Scientific Publishing Co Inc, 2009).

[56] G. Shirane, S. M. Shapiro, and J. M. Tranquada, *Neutron scattering with a triple-axis spectrometer: basic techniques* (Cambridge University Press, 2002).

[57] A. Q. Baron, arXiv preprint arXiv:0910.5764 (2009).

[58] A. Q. Baron, arXiv preprint arXiv:1504.01098 (2015).

[59] S. Petit, F. Moussa, M. Hennion, S. Pailhès, L. Pinsard-Gaudart, and a. Ivanov, Phys. Rev. Lett. **99**, 266604 (2007).

[60] S. Pailhès, X. Fabrèges, L. P. Régnault, L. Pinsard-Godart, I. Mirebeau, F. Moussa, M. Hennion, and S. Petit, Phys. Rev. B **79**, 134409 (2009).

[61] A. Togo and I. Tanaka, Scripta Materialia **108**, 1 (2015).

[62] K. Parlinski, Z. Q. Li, and Y. Kawazoe, Phys. Rev. Lett. **78**, 4063 (1997).

[63] S. Baroni, S. de Gironcoli, A. Dal Corso, and P. Giannozzi, Rev. Mod. Phys. **73**, 515 (2001).

[64] J. P. Perdew, K. Burke, and M. Ernzerhof, Phys. Rev. Lett. **77**, 3865 (1996).

[65] S. L. Dudarev, G. A. Botton, S. Y. Savrasov, C. J. Humphreys, and A. P. Sutton, Phys. Rev. B **57**, 1505 (1998).

[66] I. V. Solovyev, M. V. Valentyuk, and V. V. Mazurenko, Phys. Rev. B **86**, 054407 (2012).

[67] J. Varignon, S. Petit, and M.-B. Lepetit, arXiv preprint arXiv:1203.1752 (2012).

[68] T. J. Sato, S. H. Lee, T. Katsufuji, M. Masaki, S. Park, J. R. D. Copley, and H. Takagi, Phys. Rev. B **68**, 014432 (2003), arXiv:0304441 [cond-mat] .

[69] H. J. Lewtas, A. T. Boothroyd, M. Rotter, D. Prabhakaran, H. Müller, M. D. Le, B. Roessli, J. Gavilano, and P. Bourges, Phys. Rev. B **82**, 184420 (2010), arXiv:arXiv:1007.5490v2 .

[70] X. Fabrèges, S. Petit, I. Mirebeau, S. Pailhès, L. Pinsard, A. Forget, M. T. Fernandez-Diaz, and F. Porcher, Phys. Rev. Lett. **103**, 067204 (2009), arXiv:0905.4824 .

[71] W. Tian, G. Tan, L. Liu, J. Zhang, B. Winn, T. Hong, J. A. Fernandez-Baca, C. Zhang, and P. Dai, Phys. Rev. B **89**, 144417 (2014).

[72] L. Chaix, S. De Brion, S. Petit, R. Ballou, L. P. Regnault, J. Ollivier, J. B. Brubach, P. Roy, J. Debray, P. Lejay, A. Cano, E. Ressouche, and V. Simonet, Phys. Rev. Lett. **112**, 137201 (2014), arXiv:1402.7018 .

[73] R. M. White, M. Sparks, and I. Ortenburger, Phys. Rev. **139**, A450 (1965).

[74] S. Petit, Collection SFN **12**, 105 (2011).

[75] R. Valdés Aguilar, M. Mostovoy, A. B. Sushkov, C. L. Zhang, Y. J. Choi, S.-W. Cheong, and H. D. Drew, Phys. Rev. Lett. **102**, 047203 (2009).

[76] M. Mochizuki, N. Furukawa, and N. Nagaosa, Phys. Rev. B **84**, 144409 (2011).

[77] S. W. Lovesey, J. Phys. C: Solid State **5**, 2769 (1972).

[78] M. Mourigal, W. T. Fuhrman, A. L. Chernyshev, and M. E. Zhitomirsky, Phys. Rev. B **88**, 094407 (2013).

[79] A. B. Souchkov, J. R. Simpson, M. Quijada, H. Ishibashi, N. Hur, J. S. Ahn, S. W. Cheong, A. J. Millis, and H. D. Drew, Phys. Rev. Lett. **91**, 027203 (2003).

[80] K. Singh, M.-B. Lepetit, C. Simon, N. Bellido, S. Pailhès, J. Varignon, and A. De Muer, Journal of Physics: Condensed Matter **25**, 416002 (2013).

[81] J. Varignon, S. Petit, A. Gellé, and M. Lepetit, Journal of Physics: Condensed Matter **25**, 496004 (2013).

[82] S. Bramwell, Journal of Physics: Condensed Matter **2**, 7527 (1990).

[83] T. Lancaster, S. J. Blundell, D. Andreica, M. Janoschek, B. Roessli, S. N. Gvasaliya, K. Conder, E. Pomjakushina, M. L. Brooks, P. J. Baker, D. Prabhakaran, W. Hayes, and F. L. Pratt, Phys. Rev. Lett. **98**, 197203 (2007).

[84] D. Kozlenko, S. Kichanov, S. Lee, J.-G. Park, V. P. Glazkov, and B. Savenko, Journal of Experimental and Theoretical Physics Letters **82**, 193 (2005).

[85] P. Häfliger, S. Gerber, R. Pramod, V. Schnells, B. Dalla Piazza, R. Chati, V. Pomjakushin, K. Conder, E. Pomjakushina, L. Le Dréau, *et al.*, Physical Review B **89**, 085113 (2014).

[86] A. Chernyshev and W. Brenig, Physical Review B **92**, 054409 (2015).

[87] T. Aoyama, A. Miyake, T. Kagayama, K. Shimizu, and T. Kimura, Phys. Rev. B **87**, 094401 (2013).

[88] A. B. Garg, A. Mishra, K. Pandey, and S. M. Sharma, Journal of Applied Physics **116**, 133514 (2014).

[89] M. Aronson, S. Dierker, B. Dennis, S. Cheong, and Z. Fisk, Physical Review B **44**, 4657 (1991).

[90] T. Chatterji, B. Ouladdiaf, P. F. Henry, and D. Bhattacharya, Journal of Physics: Condensed Matter **24**, 336003 (2012).

[91] J. Agostinho Moreira, A. Almeida, W. S. Ferreira, J. P. Araújo, A. M. Pereira, M. R. Chaves, M. M. R. Costa, V. A. Khomchenko, J. Kreisel, D. Chernyshov, S. M. F. Vilela, and P. B. Tavares, Phys. Rev. B **82**, 094418 (2010).

[92] S. E. Dutton, E. Climent-Pascual, P. W. Stephens, J. P. Hodges, A. Huq, C. Broholm, and R. Cava, Journal of Physics: Condensed Matter **23**, 246005 (2011).

[93] T. Chatterji, G. N. Iles, B. Ouladdiaf, and T. C. Hansen, Journal of Physics: Condensed Matter **22**, 316001 (2010).

[94] V. S. Bhadram, B. Rajeswaran, A. Sundaresan, and C. Narayana, EPL (Europhysics Letters) **101**, 17008 (2013).

[95] J. Laverdière, S. Jandl, A. A. Mukhin, V. Y. Ivanov, V. G. Ivanov, and M. N. Iliev, Phys. Rev. B **73**, 214301 (2006).

[96] M. An, S. K. Yuan, Y. Wu, Q. M. Zhang, X. G. Luo, and X. H. Chen, Phys. Rev. B **76**, 024305 (2007).

[97] K. Park, J. Oh, J. C. Leiner, J. Jeong, K. C. Rule, M. D. Le, and J.-G. Park, Phys. Rev. B **94**, 104421 (2016).

[98] K. Takenaka, Science and technology of advanced materials **13**, 013001 (2012).

[99] S. Calder, J. G. Vale, N. Bogdanov, X. Liu, C. Donnerer, M. Upton, D. Casa, A. Said, M. Lumsden, Z. Zhao, *et al.*, Nature communications **7** (2016).

[100] S. Tóth, B. Wehinger, K. Rolfs, T. Birol, U. Stuhr, H. Takatsu, K. Kimura, T. Kimura, H. M. Rønnow, and C. Rüegg, Nature communications **7** (2016).

[101] M. C. Shapiro, S. C. Riggs, M. B. Stone, C. R. de la Cruz, S. Chi, A. A. Podlesnyak, and I. R. Fisher, Phys. Rev. B **85**, 214434 (2012).

[102] J. Yamaura, K. Ohgushi, H. Ohsumi, T. Hasegawa, I. Yamauchi, K. Sugimoto, S. Takeshita, A. Tokuda, M. Takata, M. Udagawa, M. Takigawa, H. Harima, T. Arima, and Z. Hiroi, Phys. Rev. Lett. **108**, 247205 (2012).

[103] C. H. Sohn, C. H. Kim, L. J. Sandilands, N. T. M. Hien, S. Y. Kim, H. J. Park, K. W. Kim, S. J. Moon, J. Yamaura, Z. Hiroi, and T. W. Noh, Phys. Rev. Lett. **118**, 117201 (2017).

[104] J. S. White, C. Niedermayer, G. Gasparovic, C. Broholm, J. M. S. Park, A. Y. Shapiro, L. A. Demianets, and M. Kenzelmann, Phys. Rev. B **88**, 060409 (2013).

Publications

1. "Magnon Breakdown in a Two Dimensional Triangular Lattice Heisenberg Antiferromagnet of Multiferroic $LuMnO_3$"
   Joosung Oh, Manh Duc Le, Jaehong Jeong, Jung-hyun Lee, Hyungje Woo, Wan-Young Song, T. G. Perring, W. J. L. Buyers, S.-W. Cheong, and Je-Geun Park
   Physical Review Letters **111**, 257202 (2013) Editor's Suggestion

2. "Hexagonal $RMnO_3$: a model system for two dimensional triangular lattice antiferromagnets"
   Hasung Sim, Joosung Oh, Jaehong Jeong, Manh Duc Le and Je-Geun Park
   Acta Crystallographica Section B **72**, 3 (2016)

3. "Magnon-Phonon coupling and two-magnon continuum in the two-dimensional triangular antiferromagnet $CuCrO_2$"
   Kisoo Park, Joosung Oh, Jonathan C. Leiner, Jaehong Jeong, Kirrily C. Rule, Manh Duc Le and Je-Geun Park
   Physical Review B **94**, 104421 (2016)

4. "Spontaneous decays of magneto-elastic excitations in non-collinear antiferromagnet $(Y,Lu)MnO_3$"
   Joosung Oh, Manh Duc Le, Ho-Hyun Nahm, Hasung Sim, Jaehong Jeong, T.G. Perring, Hyungje Woo, Kenji Nakajima, Seiko Ohira-Kawamura, Zahra Yamani, Y. Yoshida, H. Eisaki, S.-W. Cheong, A. L. Chernyshev and Je-Geun Park
   Nature Communications **7**, 13146 (2016)

Conference Presentations

(Oral presentations)

1. Decay and anomalous spectrum of magnon observed in h-$LuMnO_3$.
   HANARO Symposium (May. 2013 in Korea)

2. Spin phonon induced magnetic soft mode in triangular antiferromagnet h-$RMnO_3$.
   American Physical Society March meeting (Mar. 2015 at San Antonio, US)

3. Spin phonon induced magnetic soft mode in triangular antiferromagnets h-(Y,Lu)MnO_3.
   2015 Korean Physical Society Spring Meeting (Apr. 2015 in Korea)

4. Spontaneous decays of magneto-elastic excitation in noncollinear magnets (Y/Lu)MnO_3.
   Correlated Electron Systems" Gordon Research Seminar (Jun. 2016 in South Hedley, US)

5. Magnon phonon hybridization and enhanced anharmonicity in noncollinear magnets (Y,Lu)MnO_3.
   American Physical Society March meeting (Mar. 2017 at New Orleans, US)

(Poster presentations)

1. To understand the specific heat of (Y/Lu)MnO_3 using inelastic neutron scattering data.
   2013 Korean Physical Society Spring meeting (Apr. 2013 in Korea)

2. To understand the specific heat anomaly of (Y/Lu)MnO_3 using inelastic neutron scattering data
   13^{th} Japan Korea Taiwan Symposium (Jan. 2013 in Japan)

3. Excitation spectrum of 2D triangular Heisenberg antiferromagnet hexagonal $LuMnO_3$
   Quantum materials symposium (Feb. 2014 in Korea)

4. Magnon breakdown in a two dimensional triangular Heisenberg antiferromagnet $LuMnO_3$
   American Physical Society March meeting (Mar. 2014 in US)

5. Observation of magnon decay and non-linear spinwaves in $LuMnO_3$
   2014 Korean Physical Society Spring meeting (Apr. 2014 in Korea)

6. Spin phonon induced magnetic soft mode in triangular antiferromagnets $(Y/Lu)MnO_3$
   15^{th} Taiwan Japan Korea Symposium (Mar. 2015 in Taiwan)

7. Inelastic neutron scattering studies on magnon phonon coupling in triangular antiferromagnets $Y_{1-x}Lu_xMnO_3$
   14^{th} PSI Summer School on Condensed Matter Research (Aug. 2015 in Switzerland)

국문초록

삼각격자 반강자성체 육방정계 $RMnO_3$의 들뜸스펙트럼 연구: 자기-탄성 들뜸의 자발적 붕괴

오주성
물리천문학부 물리학전공
서울대학교 대학원

쩔쩔맴 자성체는 새로운 물질상태를 야기할 수 있는 플랫폼으로서 연구되어왔다. 동일 선상의 기저 상태를 갖는 보통 자석과는 달리, 쩔쩔맴 자성체에서의 상호 작용은 동시에 만족 될 수 없으며, 이는 고전적 기저 상태의 축퇴를 유발한다. 그러한 경쟁하는 기저 상태는 추가적인 섭동에 민감 해지며, 이는 기저 상태 및 여기에너지에 특별한 영향을 미칠 수 있다.

기하학적으로 쩔쩔맴 현상이 있는 가장 단순한 모델 자성체는 2차원 삼각격자 하이젠버그 반강자성체 이다. 이론적으로, 2차원 삼각격자 반강자성체 에서는 마그논의 에너지 변화와 선폭 증가가 있을 것으로 예측되었다. 그러나 실제 물질에 존재하는 격자 변형 또는 스핀 포논 결합과 같은 추가적인 복잡성으로 인해 이러한 이론적 예측과 실험의 직접적인 비교는 드물었다. 그러한 적당한 스핀 포논 결합을 갖는 변형된 삼각격자 반강자성체 후보 물질 중 하나는 육방정계 희토류 망간산화물 (h-$RMnO_3$)이다.

단결정 비탄성 중성자 산란에 의해 측정된 마그논 스펙트럼은 마그논 포논 결합을 고려한 비선형 스핀파 계산에 의해 재현되었다. 캐나다의 초크 리버 연구소 (Chalk River Laboratory)의 C5 스핀 편광 분광계와 영국 ISIS의 MAPS 빔라인에서 비탄성 중성자 산란 기술을 사용하여 $Y_{1-x}Lu_xMnO_3$의 자기 여기 스펙트럼을 측정하였다. 전반적인 스펙트럼은 단순한 스핀 해밀토니안에 의한 선형 스핀파 이론에 의해 재현되지만, 기존의 마그논 들뜸에 의해 설명 될 수없는 고에너지에서의 약한 추가 신호를 관찰했다. 들뜸 스펙트럼에서 나타나는 이러한 특이점을 설명하기 위해서는 이전에 $RMnO_3$의 탄성 특성에 중요한 역할을 하는 것으로 알려진 스핀 격자 결합과 같은 추가적인 효과를 고려할 필요가 있다. 실제로, h-$RMnO_3$의 비동일선상 스핀 구조는 자기 스펙트럼에서 추가 모드를 생성 할 수있는 직접적인

마그논 포논 결합을 허용한다. 이를 검증하기 위해 우리는 비탄성 엑스선 산란 기법을 사용하여 $YMnO_3$의 포논 스펙트럼을 T_N 위아래로 측정하였다. T_N 아래에서, 우리는 강한 마그논 포논 결합의 존재를 명확히 나타내는, 마그논과 동일한 운동량과 에너지를 갖는 추가적인 포논 모드를 관측했다. 비슷하게, 비탄성 중성자 산란 실험에서 관측된 추가적인 신호 또한 포논과 동일한 운동량 및 에너지를 갖는 것을 확인하였다. 이러한 넓은 운동량 공간에서의 강력한 결합은 운동량 공간에서 좁은 영역에 한정된 마그논 포논 결합을 보고했던 이전 연구와 구별된다. 따라서 우리는 새로운 혼합된 모드를 자기 탄성 들뜸이라고 명명하였다.

마그논 포논 결합과 더불어, 비동일선상 스핀 구조는 이차원 삼각격자 반강자성체 $RMnO_3$의 마그논 붕괴를 유도 할 것으로 기대되었다. 비탄성 중성자 산란 데이터를 분석함으로써, 우리는 그러한 붕괴의 증거인 자기탄성 들뜸의 선폭 증가를 관측했다. 관측 선폭을 재현하기 위해, 우리는 자기 탄성 모드의 감쇠율을 계산하는 이론적인 방법을 개발했다. 계산 결과는 선폭의 운동량 의존성을 정성적으로 설명하였다.

주요어: 삼각격자 반강자성체, $RMnO_3$, 마그논 포논 결합, 비선형 현상, 비탄성중성자산란, 비탄성엑스선산란
학 번: 2013-30920